

ABSTRACT

Title of dissertation: EXPERIMENTS WITH TRAPPED IONS
AND ULTRAFAST LASER PULSES

Kale Gifford Johnson
Doctor of Philosophy
2016

Dissertation directed by: Professor Christopher R. Monroe
Joint Quantum Institute
University of Maryland Department of Physics
and
National Institute of Standards and Technology

Since the dawn of quantum information science, laser-cooled trapped atomic ions have been one of the most compelling systems for the physical realization of a quantum computer. By applying qubit state dependent forces to the ions, their collective motional modes can be used as a bus to realize entangling quantum gates. Ultrafast state-dependent kicks [1] can provide a universal set of quantum logic operations, in conjunction with ultrafast single qubit rotations [2], which uses only ultrafast laser pulses. This may present a clearer route to scaling a trapped ion processor [3]. In addition to the role that spin-dependent kicks (SDKs) play in quantum computation, their utility in fundamental quantum mechanics research is also apparent. In this thesis, we present a set of experiments which demonstrate some of the principle properties of SDKs including ion motion independence (we demonstrate single ion thermometry from the ground state to near room tempera-

ture and the largest Schrödinger cat state ever created in an oscillator), high speed operations (compared with conventional atom-laser interactions), and multi-qubit entanglement operations with speed that is not fundamentally limited by the trap oscillation frequency. We also present a method to provide higher stability in the radial mode ion oscillation frequencies of a linear radiofrequency (rf) Paul trap—a crucial factor when performing operations on the rf-sensitive modes. Finally, we present the highest atomic position sensitivity measurement of an isolated atom to date of $\sim 0.5 \text{ nm Hz}^{-1/2}$ with a minimum uncertainty of 1.7 nm using a 0.6 numerical aperture (NA) lens system, along with a method to correct aberrations and a direct position measurement of ion micromotion (the inherent oscillations of an ion trapped in an oscillating rf field). This development could be used to directly image atom motion in the quantum regime, along with sensing forces at the yoctonewton (10^{-24} N) scale for gravity sensing, and 3D imaging of atoms from static to higher frequency motion. These ultrafast atomic qubit manipulation tools demonstrate inherent advantages over conventional techniques, offering a fundamentally distinct regime of control and speed not previously achievable.

EXPERIMENTS WITH TRAPPED IONS AND ULTRAFAST
LASER PULSES

by

Kale Gifford Johnson

Dissertation submitted to the Faculty of the Graduate School of the
University of Maryland, College Park in partial fulfillment
of the requirements for the degree of
Doctor of Philosophy
2016

Advisory Committee:

Professor Christopher R. Monroe, Chair/Advisor

Dr. William D. Phillips

Professor James R. Williams

Professor Alexey V. Gorshkov

Professor Christopher C. Davis

© Copyright by
Kale Gifford Johnson
2016

Dedication

This thesis is dedicated to Chris, my advisor, and to the scientists in our group. For all the help you have given me, I hope this may be helpful in return. It is also dedicated to my other friends, who keep me going, and to my family, who love and support me. And finally, to Brittany, who would fall in love with a graduate student like me and be happy about it!

Acknowledgments

There are a lot of people that contributed (almost completely of their own volition) to the results of the research presented here, and also to my enjoyment as a graduate student. It all started when I was born...actually I won't start that far back. Although I could with my family—thank you for giving me the freedom and support to find something I love to do. I love you, and I hope I give back as much as you give me. Thank you Chris, my academic father. It has been a pleasure learning the trade from you. Your busy schedule meant that I had to glean as much as I could from every one of our interactions. Thanks to your intensity to learn and compete, and your respect for skill and good comedy, music, sports, culture and family, I did enjoy our time together. You never wasted a moment of my time; even while I spent plenty of yours. With great delicacy, you smoothed out all the BS ideas I threw at you over these past years, and now I finally feel like a physicist. Thank you.

Thanks David Wong-Campos, who came into the "Ultrafast Lab" two years after me but had the audacity to direct some of our efforts towards optics research—his passion. You indeed taught me a great deal about optics, along with quite a few other things including reading science articles for pleasure, and that there is plenty out there which can still be greatly improved or invented. You have become a great friend, and I look forward to continuing the work we have started together. Thank you Jonathan Mizrahi for training me in the lab after I arrived, and for the technical and theoretical support you still provide. Your patience is something to aspire to.

Thank you Brian Neyenhuis; in addition to the fierce nature with which you attack problems (I'm sure you're laughing at that image), you know how to keep a team talking. While not all of the time spent is discussing physics, creative ideas spawned from many of our conversations while reloading the ion trap. Thank you Crystal Senko; our shared time on the ultrafast project was the shortest of the four, but I am very glad to have had it. Your methodical approach and long list of ion trap references taught me some important lessons early on. I also do not forget the help you gave when I moved, or all the advice you had for a new graduate student!

Thanks also to all the other members of the ion trapping group that I've known over my 5 years in the group. Just listing your names isn't thanks enough—but hopefully you remember what we've done, from useful ideas and discussions to doing smart and not-so-smart things at conferences and liquid lunches, long days in the lab, carrying furniture, wiring traps, discussing books, bicycling, trivia and friendly chalkboard arguments—David Hayes, Wes Campbell, Grahame Vittorini, Volkan Inlek, Clayton Crocker, Jake Smith, Ken Wright, Phil Richerme, Marty Lichtman, Nobert Linke, Kenny Lee, Emily Edwards, Rajibul Islam, Paul Hess, Ilka Geisel (visiting student), Simcha Korenblit, Susan Clark, Andrew Manning, Taeyoung Choi, Geofry Ji, Kate Collins, Caroline Figgatt, Aaron Lee, Kevin Landsman, Shatanu Debnath, Guido Pagano, and Jiehang Zhang. Being around all of you was enjoyable, educational and rewarding. The exceptional quality of research that happens in our group and at the JQI is thanks to you.

I also spent a few months in Australia working with Mike Biercuk. I would like also to thank him and his students MC Jarratt, Alex Soare, Harrison Ball and post

doc David Hayes (again) for the refreshing time and the good research. Thanks also to our collaborator Alex Retzker and his students Itsik Cohen, and Amit Rotem. Your efforts will allow us to improve upon the work presented here. Finally, thanks to everyone else who was not mentioned but who helped me and this work.

Table of Contents

| | |
|--------------------------------------------------------------------------|------|
| List of Tables | viii |
| List of Figures | ix |
| List of Abbreviations | xi |
| 1 Introduction | 1 |
| 2 The Apparatus | 9 |
| 2.1 Linear Rf Ion Traps | 9 |
| 2.2 The Blade Ion Trap and Vacuum Chamber | 12 |
| 2.3 Experimentation with One and Two Ions | 20 |
| 2.3.1 The $^{171}\text{Yb}^+$ Ion | 20 |
| 2.3.2 Loading, Cooling and Detection | 22 |
| 2.3.3 Rotating Ion Trap Axes | 27 |
| 2.3.4 Doppler Cooling along multiple Axes | 28 |
| 2.4 Second Ionization to Create $^{171}\text{Yb}^{2+}$ with Laser Pulses | 31 |
| 2.5 Imparting Ultrafast Laser Forces to Atoms | 34 |
| 2.5.1 Spin-Dependent Kick Generation | 34 |
| 2.5.2 Frequency Domain Interpretation | 42 |
| 2.5.3 The Mode-Locked Laser | 44 |
| 2.5.4 Picking and Rotating Pulses at 100 MHz | 47 |
| 3 Stabilizing Ion Secular Motion | 50 |
| 3.1 trap rf stabilization | 52 |
| 3.2 Ion Oscillation Frequency | 56 |
| 3.3 Limits and noise sources | 60 |
| 4 Sensing Atomic Motion | 65 |
| 4.1 Experimental Description | 66 |
| 4.2 Thermometry | 69 |
| 4.3 Fock State Tomography | 72 |
| 4.4 Limits of Measurement | 75 |

| | | |
|-------|--------------------------------------------|-----|
| 5 | Ultrafast Schrödinger Cat States | 77 |
| 5.1 | Experimental Setup | 88 |
| 5.2 | Three and Four-Component Cat Contrast | 89 |
| 5.3 | Six and Eight-Component Cat Contrast | 91 |
| 5.3.1 | Sources of Error | 91 |
| 6 | Highly Sensitive Atom Imaging | 93 |
| 6.1 | Experimental Apparatus | 94 |
| 6.2 | Aberration measurement and correction | 95 |
| 6.3 | Position sensitivity | 99 |
| 6.4 | Sensing of Rf Induced Micromotion Position | 103 |
| 6.5 | Outlook | 106 |
| 7 | Realizing an Ultrafast Two Ion Gate | 108 |
| 7.1 | Single Mode Phase Accumulation | 109 |
| 7.2 | Two Ion Relative Phase Accumulation | 109 |
| 7.3 | A Particular Solution | 112 |
| 7.4 | Measuring Entanglement | 118 |
| 8 | Outlook and Future Directions | 122 |
| 8.1 | Imaging a Large Cat State and Other Motion | 122 |
| 8.2 | Delta-Kicked Harmonic Oscillator | 123 |
| 8.3 | Hamiltonian Engineering | 123 |
| 8.4 | Superfast Cooling | 124 |
| 8.5 | Two-dimensional Cat States | 124 |
| 8.6 | Working in the Infrared | 124 |
| | Bibliography | 126 |

List of Tables

| | | |
|-----|---------------------------------------------------------------|----|
| 2.1 | Blade trap and chamber assembly in-vacuo parts | 14 |
| 2.2 | Blade trap and chamber assembly out-of-vacuum parts | 15 |
| 3.1 | Component Stability | 61 |

List of Figures

| | | |
|------|----------------------------------------------------------------------|-----|
| 2.1 | Linear Paul "blade" trap | 11 |
| 2.2 | Ion trap and vacuum chamber assembly | 13 |
| 2.3 | Blade trap photographs and sketches | 18 |
| 2.4 | Circuit diagram of in-vacuo rf filter | 19 |
| 2.5 | $^{171}\text{Yb}^+$ atomic energy level diagram | 21 |
| 2.6 | Ion detection and imaging | 26 |
| 2.7 | Adjusting the trap axes | 29 |
| 2.8 | 2D ion trajectory from scattering a single photon | 30 |
| 2.9 | Observation of double ionization | 33 |
| 2.10 | Conditions for a spin-dependent Kick | 43 |
| 2.11 | Experimental setup of Raman laser | 45 |
| 2.12 | Triggering a pulse sequence | 49 |
| | | |
| 3.1 | Ion trap rf drives with active stabilization | 53 |
| 3.2 | Helical resonator with a capacitive divider pickoff | 54 |
| 3.3 | Rectifier circuit diagram and photograph | 56 |
| 3.4 | Suppression of injected noise | 57 |
| 3.5 | Ramsey fringe contrast with and without feedback | 59 |
| 3.6 | Secular frequency noise with and without feedback | 59 |
| 3.7 | Allan deviation of the secular frequency | 61 |
| 3.8 | Simulation of rectifier response | 64 |
| | | |
| 4.1 | Ultrafast atom interferometry | 68 |
| 4.2 | Ultrafast sensing measurements of \bar{n} | 71 |
| 4.3 | Ultrafast phase space tomography | 74 |
| | | |
| 5.1 | Cat state experimental schedule and coherent state control | 81 |
| 5.2 | Cat state creation and verification | 83 |
| 5.3 | Three, four, six and eight-component cat states | 86 |
| | | |
| 6.1 | Schematic of the imaging system | 94 |
| 6.2 | Aberration measurement results | 96 |
| 6.3 | Position uncertainty of the trapped ion | 100 |

| | | |
|-----|---------------------------------------------------------|-----|
| 6.4 | Micromotion position measurement | 103 |
| 7.1 | A two ion SDK | 110 |
| 7.2 | Phase space and SDK timing for a gate | 114 |
| 7.3 | Phase space trajectories for $N_1 = 1$ | 115 |
| 7.4 | Phase space trajectory for $N_1 = 2$ | 116 |
| 7.5 | Phase space trajectory for $N_1 = 3, 4, 5, 6$ | 117 |
| 7.6 | Ultrafast Entanglement Partiy Oscillations | 121 |

List of Abbreviations

| | |
|-------|---------------------------------------------|
| AWG | Arbitrary Waveform Generator |
| BEC | Bose-Einstein Condensate |
| CCD | Charge-Coupled Device |
| CF | ConFlat |
| COM | Center of Mass |
| DC | Direct Current |
| EMCCD | Electron Multiplying Charge-Coupled Device |
| GVD | Group Velocity Dispersion |
| ICCD | Intensified Charge-Coupled Device |
| LO | Local Oscillator |
| MOT | Magneto-Optical Trap |
| NA | Numerical Aperture |
| PMT | Photomultiplier Tube |
| PSF | Point Spread Function |
| QIP | Quantum Information Processing |
| Rf | Radiofrequency |
| SDK | Spin-Dependent Kick |
| SQUID | Superconducting Quantum Interference Device |
| UHV | Ultra-High Vacuum |
| UV | Ultraviolet |

Chapter 1: Introduction

Since the proposal of an efficient quantum factoring algorithm [4], the past 22 years has seen a flurry of activity surrounding the development of quantum information processing (QIP). The number of experimental apparatuses that have been able to isolate individual quantum systems is now quite large—sufficiently describing each would require more than one thesis—and includes superconducting electronic circuits [5], microwave photon cavities [6], color centers in crystalline substrates [7], freely propagating photons [8], nanomechanical resonators [9–11], quantum ”dots” in Silicon [12], unbound room temperature molecules [13], cold, trapped, neutral [14] and charged atoms [15], atomic clouds [16] and molecules [17], plus more; this is not to mention the theoretical advances that have helped shape each of these fields. Each quantum technology has its advantages and disadvantages.

In ion trapping, the story of isolating and controlling quantum systems started before the boom of QIP research. David Wineland’s 2012 Nobel Lecture [18] gives a clear account of the history, which is very closely related to this thesis and parallels part of, and I will try to summarize the relevant parts of his account. The first laser cooling of atoms occurred in 1978, in two different ion traps [19, 20], following proposals that radiation pressure could be used to reduce the temperature of trapped

ions [21, 22]. Further progress in Doppler, then sub-Doppler cooling to near the ground state of the bound atom [23, 24], opened the door for quantum control of both the individual electronic states of an atom and of the harmonic motion of those trapped atoms. Through a relatively straightforward experimental process, by which a laser excites an optical transition in addition to changing the harmonic motion of the trapped atom by one quanta of energy—most commonly known as a Jaynes-Cummings interaction [25]—it became possible to prepare and control motion at the quantum level [18]. Following the theoretical groundwork [26], entangling gates between an internal and external degree of freedom of a single atom were carried out [27]. Spin-motion entanglement came shortly after, bringing about the creation of Schrödinger cat states [28] and eventually entanglement between two [29], and more [30] ions based on proposals using geometric phase as the entanglement generator [31]. Other methods for entangling quantum motion with internal states of an atom have emerged which hope to push the level of control further using near-field microwaves, or ultrafast laser pulses. These, and many other, advances of ion traps have built a foundation that is supporting a broad range of research in quantum science.

The recent push to change the state-of-the-art in spin-motion entanglement has arisen because of several limitations associated with current methods. Performing high fidelity operations typically requires that the atom be within the "Lamb-Dicke" regime where $(kz_0)^2(2\bar{n} + 1) \ll 1$ (k is the wavenumber of light driving the transition, z_0 is the ground state spread of the motion in 1-dimension, and \bar{n} is the average number of motional quanta, or phonons, stored in the oscillator). Remov-

ing this restriction allows the motion of trapped atoms to be controlled without the stringent requirement of near-ground-state cooling during experimental state preparation steps. Removing the restriction also allows larger quantum states of motion to be generated. Ultrafast laser pulses have proven to be one way of removing this restriction [1, 32], by manipulating states initially prepared to be far outside the Lamb-Dicke regime (\bar{n} up to 10^4) [33], and by generating entangled quantum states that extend outside of the Lamb-Dicke regime in just hundreds of nanoseconds—faster than a single period of harmonic oscillation.

Using ultrafast laser pulses to manipulate quantum states also has the advantage of speed. In an experiment led by Wesley Campbell, before I joined the group, arbitrary, single-qubit π -rotations were made on the $^{171}\text{Yb}^+$ hyperfine "clock" transition (12.6 GHz splitting) in less than 50 ps [2]. This demonstration, where the qubit rotations occurred more than 10^4 times faster than a single period of harmonic oscillation of the trapped ion, with better than 0.99 fidelity took a small fraction, less than 10^{-8} , of the qubit coherence time and demonstrated the first step towards a general quantum processor using only ultrafast pulses. As mentioned above, gains in computational speed are not limited to the internal degree of freedom, and a technique has also been proposed (and implemented, as of this thesis) to generate two-qubit entanglement in a time shorter than a single motional oscillation period [3, 32, 34]. Demonstrating such a gate is an important benchmark because previous gates relied on spectral resolution of the phonons—quantized excitations in the eigenmodes of motion—which limits the gate time to be greater than the trap oscillation period.

Faster operations have additional advantages beyond reducing the effects of decoherence and increasing processing speeds: a fast enough entangling gate between two ions in a group can act through local modes of motion without exciting the collective motional modes of the larger group. This property could be a way to scale-up the number of operations available to a single group of trapped ions, which would complement other proposed methods such as shuttling ions into and out of different zones on a single apparatus [35], and using switchable interconnects to route photons between multiple quantum registers [36].

There are other reasons to use ultrafast operations, such as the ability to engineer Hamiltonians through trotterization (the decomposition of a desired unitary evolution operator into a stroboscopic sequence of shorter evolutions [37]) faster than the decoherence time of the ion for quantum simulation or cooling [38–40], studying quantum chaos in a delta-kicked harmonic oscillator [41], and others. Simply having a nearly impulsive, qubit state-dependent force is generally useful, and demonstrations of some of the initial possibilities has been rewarding. This thesis follows closely behind the research laid out by Jonathan Mizrahi, Wes Campbell and others, who developed the first stages of this process and worked out how an ultrafast spin-dependent kick (SDK) can be made in the lab [1]. While creating and running the experiments in this thesis, focused on ultrafast control, several discoveries and pieces of technology were made that turned out to be particularly useful. The second ionization of ^{+}Yb using ultrafast pulses was realized accidentally, while an improved method of stabilizing the harmonic oscillation frequency [42], and a generally useful microscopy technique used to localize a trapped ion position better

than 2 nm [43] were both realized intentionally. These early ultrafast, and other, experimental advances are the focus of this thesis. An outline is given below.

- Chapter two is an overview of the experimental apparatus and techniques that were used while conducting this research. The chapter is focused mainly on the aspects to which I contributed directly, with supplemental details on theory and past work that is especially relevant. It covers the vacuum and trap assembly, the lasers, and a review of laser interactions detailed previously [44]. It also covers a short description of an effect we saw with one of our ultrafast lasers, where second ionization of $^{171}\text{Yb}^+ \rightarrow ^{171}\text{Yb}^{2+}$ was induced through a short exposure to high energy pulses. This was not pursued due to time constraints, but evidence of the process is clear.
- Chapter three describes a method that we developed to stabilize the ion secular frequency by using active feedback control on the trap radiofrequency drive amplitude. This was important for ion trapping in general, because the secular frequency stability of most ion traps is about 1 part per thousand over an hour. We were able to improve this to 10 parts per million, in addition to reducing higher frequency noise.
- Chapter four covers an experiment in which senses the initial motional state of a trapped ion. A single ion is prepared in a variety of different thermal and pure motional states. For any given state, the motion is divided into two copies, using SDKs, before being recombined some time later. The interference of the copies with each other is monitored. This process is referred to as atom

interferometry. By adjusting the time between SDKs, which open and close the atom interferometer, the motional state is mapped out. This was shown to work on thermal states ranging from ground-state-cooled to near room temperature, and also allows us to observe the quantum nature of a pure number state of the harmonic oscillator.

- Chapter five describes an experiment where we explore the limits of creating Schrödinger cat states with spin-dependent kicks. In a harmonic oscillator, a cat state is often referred to as the quantum superposition of multiple classical-like oscillations which are localized to much less than the separation between them [18, 45]. We create a cat state which grows in size by $4\hbar k$ of momentum ($k = 2\pi/355 \text{ nm}$) by applying every pulse from a mode locked laser (repetition rate $\approx 80 \text{ MHz}$) to impart an SDK. This is accomplished using a switching technique that is discussed further in chapter 5. We also create the largest cat state ever made using a high fidelity technique that is resonant with half the trap frequency by kicking the ion every half trap period. Finally, we generate cat states with more than two localized components—up to eight—by applying additional microwave pulses during the kick sequences.
- Chapter six gives a method by which we were able to correct the aberrations in a relatively high numerical aperture (NA) imaging system. The technique requires taking only a single shot intensity profile of light collected from a point-like emitter and fitting a truncated set of Zernike polynomials. Through this, we can determine the magnitude of standard aberrations the Zernike co-

efficients represent, such as defocus, coma, astigmatism and so on, and feed that information back to the lens position to create a diffraction limited spot. After using this technique with our high NA system, we integrated the image of a trapped $^{174}\text{Yb}^+$ ion on an electron multiplying charge-coupled device (EMCCD) to achieve the best position localization ever measured from an isolated atom. In addition, we replaced the EMCCD with a razor blade and photomultiplier tube (PMT) to observe the motion of the ion by looking directly at the position-dependent illumination of the mask and PMT. This is in contrast to all previous ion trap measurements at this small level of motion (10-20 nm), where the velocity-dependent fluorescence is correlated with the trap rf drive.

- Chapter seven describes an experiment where two ions in the same trap are entangled with each other using a series of SDKs. This demonstrates the first temperature insensitive entangling gate, and also the first entangling gate which is not restricted to be temporally longer than a trap period.
- Chapter eight is an outlook and covers current ideas on future directions for the experiments. These include pursuing higher fidelity entangling gate methods by more effective power stabilization and possibly modifying the system to use a lower frequency optical or infrared laser pulse while pulse-shaping before frequency multiplying to address the desired atom transition. This would allow us to use more sophisticated optical techniques and devices such as a spacial light modulator, which break down when used with even modest inten-

sities of ultraviolet laser light. Other experiments include looking at quantum chaos in a delta-kicked harmonic oscillator, faster ground state cooling using strong ultrafast pulses, directly imaging our large cat state and other motional states, Hamiltonian engineering through Trotterization, or generating cat states in two dimensions. We believe there are many more possibilities with this experiment which have not been discovered.

Chapter 2: The Apparatus

All of the experiments presented in this thesis were performed on $^{171}\text{Yb}^+$, $^{174}\text{Yb}^+$, and $^{171}\text{Yb}^{2+}$ trapped in a linear radiofrequency (rf) Paul trap. In my first summer with the group, I was fortunate to be given the responsibility of building our ion trap and vacuum chamber (with assistance from Jonathan Mizrahi and David Hucul among others). The account of that construction along with a brief introduction to linear rf ion traps is covered in this section. Additionally, the relevant atomic transitions and laser interactions required for trapping and controlling the motion and qubit state of the ions are presented. Finally, observation of a method to produce $^{171}\text{Yb}^{2+}$ ions from trapped $^{171}\text{Yb}^+$ is briefly discussed. There are many considerations which play into an experiment like this, but some are now standard and covered in previous theses and papers by our group and others. Other aspects of this experiment are less typical or even unique, and so more time is spent on them.

2.1 Linear Rf Ion Traps

We trap individual ions in a linear rf trap, which consists of a two-dimensional rf quadrupole electric field superposed with a static quadrupole electric field to

provide confinement along the longitudinal direction [46]. Longitudinal confinement is typically much weaker than the transverse confinement, so that a crystal of laser-cooled ions resides along the $x = y = 0$ rf field null with minimal rf-induced micromotion [15, 47, 48]. The transverse confinement, dictated by the rf fields, is used as an information bus in many applications because motion along these directions is at higher frequency, and the transverse normal mode spectrum for a chain of ions can be tuned [49]. When speed and independently tunable frequencies are not necessary, it is more common to use the stable, micromotion-free longitudinal modes. In the experiments presented here, we use a single transverse mode for all coherent operations. Linear ion traps exist in a variety of topologically equivalent electrode configurations, some even with electrodes all in a single plane for ease in lithographic fabrication [50].

The linear trap used in these experiments has four gold-plated ceramic “blade” electrodes with their edges running parallel to the longitudinal (z) axis of the trap, similar to the drawing in Fig. 2.1. Two opposite blades are driven with an rf potential with respect to the other two static blades, creating the transverse (x - y) quadrupole confinement potential. Appropriate static potentials applied to the longitudinally-segmented static blades serve to confine the ions along the z -axis. The rf electric quadrupole potential near the center of the trap

$$V(x, y) = \frac{\mu V_0}{2R^2}(x^2 - y^2) \cos \Omega t \quad (2.1)$$

is set by the rf amplitude on the trap electrode, V_0 , the distance from the trap center to the electrodes, R , the rf drive frequency Ω , and a dimensionless geometric

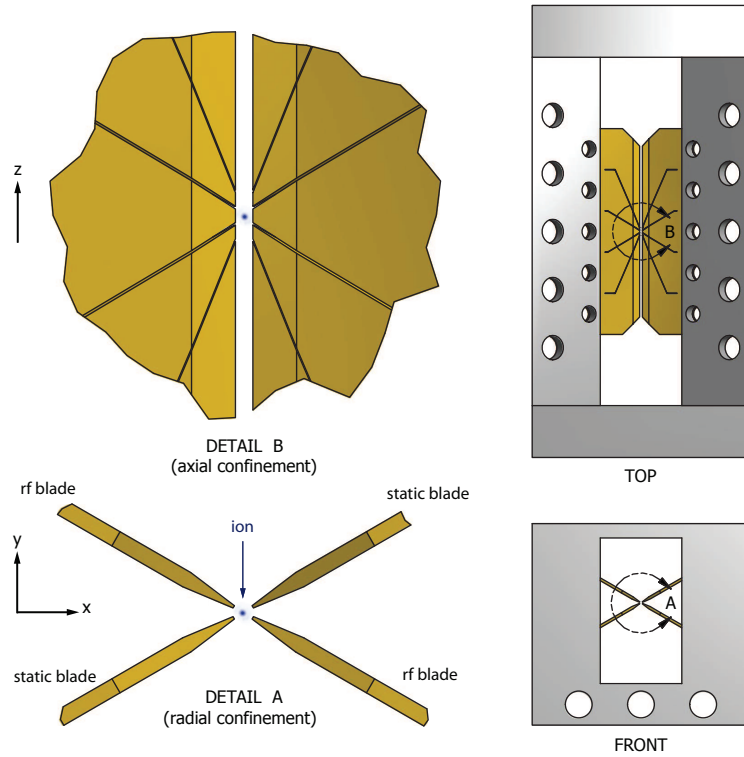


Figure 2.1: Linear Paul trap created with four gold-plated blade electrodes that are held in place by an insulating mount [42]. An ion is confined in between the electrodes through a combination of rf and static potentials applied to the electrodes. Each blade is split longitudinally into 5 segments that are electrically isolated on the static blades and electrically connected on the rf blades. The transverse distance from the ion axis to each electrode is $R = 200 \mu\text{m}$, and the length of the central longitudinal segments is $400 \mu\text{m}$.

efficiency factor $\mu \sim 0.3$ for the geometry of Fig. 2.1. A particle with charge e and mass m inside the trap feels a resulting ponderomotive “pseudopotential”

$$U_{\text{pon}} = \frac{e^2}{4m\Omega^2} |\nabla V|^2 = \frac{e^2 \mu^2 V_0^2}{4m\Omega^2 R^4} (x^2 + y^2), \quad (2.2)$$

with harmonic oscillation frequency [51],

$$\omega = \frac{e\mu V_0}{\sqrt{2}m\Omega R^2}. \quad (2.3)$$

This expression is valid under the pseudopotential approximation where $\omega \ll \Omega$ [47, 51], and we do not consider the residual transverse forces from the static potentials, because they are relatively small and stable.

2.2 The Blade Ion Trap and Vacuum Chamber

The ion trap and chamber were assembled in-house, with a majority of the individual components being purchased or custom ordered. In order to minimize background gas collisions, which disturb experiments in a number of ways (formation of YbH^+ , population of the $^2\text{F}_{7/2}$, and impulsive heating [44]), the ion trap is held at ultra-high vacuum, or UHV ($< 10^{-9}$ torr), inside of a stainless steel chamber. (The chamber modules are connected using ConFlat (CF) technology.) Using clean assembly procedures and parts, we achieve vacuum pressures near 10^{-11} Torr, which allows a single trapped ion to be held without collision for ~ 1 hour on average (collisions with H_2 , the dominant consideration for a clean system, are considered using the H_2 -ion Langevin cross-section [52]). The trap and chamber shown in Fig. 2.2, drawn using the computer-aided design software Autodesk Inventor, was built using the parts in Tables 2.1 and 2.2.

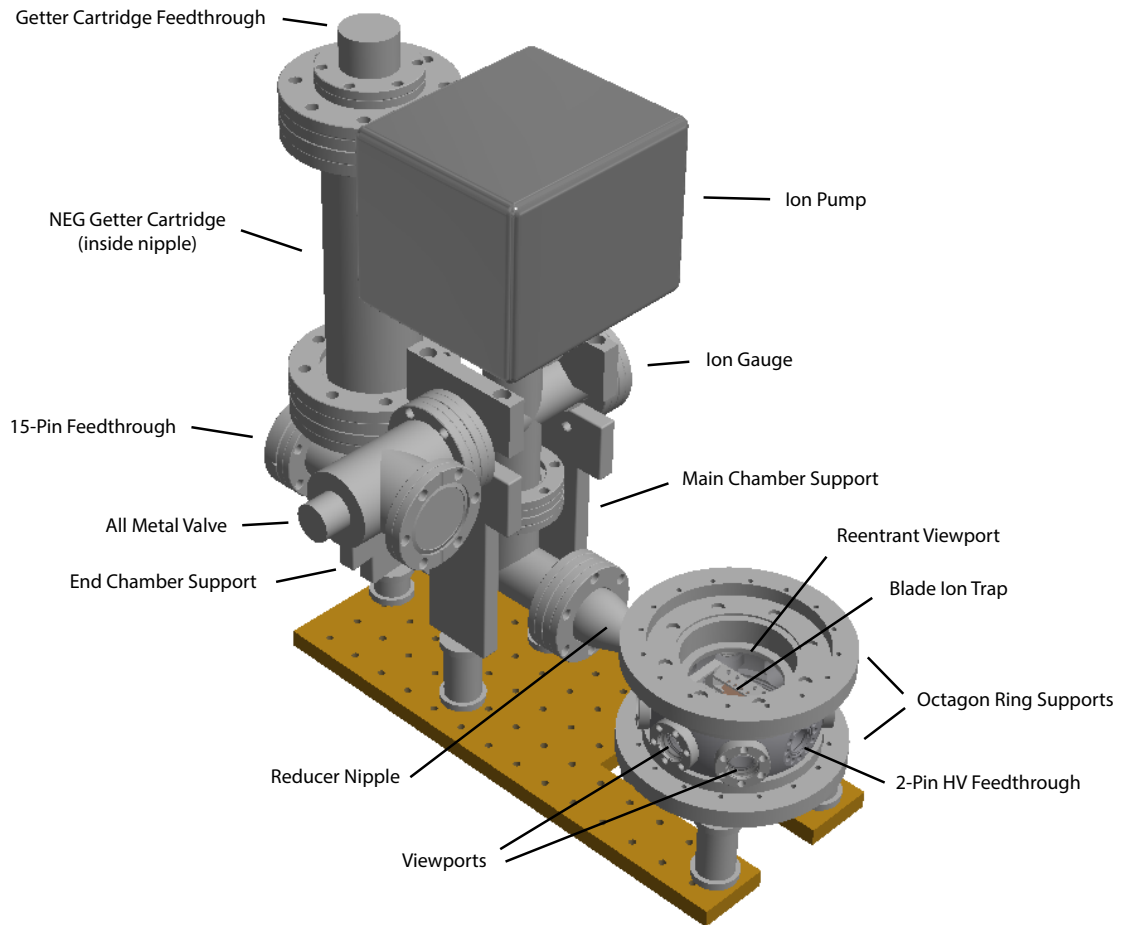


Figure 2.2: Blade ion trap and vacuum chamber assembly. The ion trap is housed inside of a spherical octagon chamber for high optical access through fused silica viewports on the top, bottom, and sides of the chamber. Each section of the chamber is connected with stainless steel "tubes" that are joined with ConFlat (CF) seals. Electrical connections to the ovens and blade segments are passed outside of the chamber with feedthroughs at either end of the chamber.

Table 2.1: Blade trap and chamber assembly in-vacuo parts. Viewports were anti-reflective coated by Spectra Thin Film for 355, 369 and/or 935 nm. Blades were gold coated by Sandia Nation Laboratories, two having static and two having AC style coating.

| Part | Vendor | Part Number |
|---------------------------------|---------------------------|---------------------------|
| Spherical Octagon Chamber | Kimball Physics | MCF450-SphOct-E2A8 |
| Groove Grabbers (5) | Kimball Physics | MCF450-GrvGrb-C01 |
| 4-Way Standard Cross | Kurt J. Lesker | C-0275 |
| Standard Tee (2) | Kurt J. Lesker | T-0275 |
| Conical Reducer Nipple | Kurt J. Lesker | CRN275X133 |
| Full Nipple | Kurt J. Lesker | FN-0337 |
| All Metal Valve | Kurt J. Lesker | VZCR40R |
| Zero-Length Reducer Flng. (2) | Kurt J. Lesker | RF337X275T |
| Copper Gaskets | Kurt J. Lesker | GA-0133,... |
| Macor Blade Holder | Maryland Machine | |
| Blade (4) | Laser Micromachining Ltd. | |
| Screws (to secure blades)(8) | Small Parts Inc. | 00-90, 0.125" SS 303 |
| Washers (") (8) | Small Parts Inc. | 0 outer diam-0.125" SS |
| Lock Washers (") (8) | Small Parts Inc. | 18-8 split lock washer SS |
| Nuts (") (8) | J. I. Morris | 00 SS 303 |
| Washers (") (16) | J. I. Morris | 00 SS 303 |
| In Vacuo Capacitors (10) | ATC | 116UL821M100TT |
| Gold Ribbon | Semicond. Pkg. Materials | 0.015" x 0.0005" |
| Constantan Foil | | |
| Left-Handed Oven Holder (2) | Mackenzie Machine | |
| Right-Handed Oven Holder | Mackenzie Machine | |
| Oven Holder Mount (3) | Mackenzie Machine | |
| ¹⁷¹ Yb Enriched Oven | Oak Ridge N.L. | |
| Yb Nat. Ab. Oven | Alvasource | AS-2-Yb-95-F |
| Ba Nat. Ab. Oven | Alvasource | AS-2-Ba-55-F |
| 15-Pin Vac. Side Cbl. Kit | MDC | 9921032 |
| 15-Pin Feedthrough | MDC | 9162002 |
| 2-Pin HV Feedthrough | MDC | 9422011 |
| 1.33" Viewport(6) | MDC | 9722013 |
| 4.5" Reentrant Viewport | UKAEA | |
| 4.5" Viewport (Bottom) | UKAEA | |
| Ion Gauge | Agilent Technologies | 9715007 |
| Ion Pump | Agilent Technologies | 9191145 |
| NEG Getter Cartridge | SAES | 4H04193 |
| Getter Cartridge Feedthrough | SAES | 4H04023 |
| Getter Ribbon | SAES | 4F0280D |
| Getter Pellets | SAES | S5K0467 |

Table 2.2: Blade trap and chamber assembly out-of-vacuum parts.

| Part | Vendor | Part Number |
|---------------------------|----------------------|----------------------|
| 15-Pin Air Side Cable Kit | MDC | 9921024 |
| Ion Gauge Cable | Duniway Stockroom | ND-IGH-25-MultiGauge |
| Ion Gauge Controller | Agilent Technologies | XGS600H1M0C0 |
| Ion Pump Controller | Agilent Technologies | 9297000 |
| Ion Pump Cable | Agilent Technologies | 9290705 |
| Main Chamber Support (2) | Mackenzie Machine | |
| End Chamber Support (1) | Mackenzie Machine | |
| Octagon Ring Support (2) | Mackenzie Machine | |
| Bolts (chamber assembly) | Kurt J. Lesker | SBK832050,... |

The chamber is designed to be compact, keeping the distances (spanned by "tubes") from the pumps to the trapping region as short as possible. The tubes are kept as wide as practicality allows. These designs are guided by standard vacuum principles, which can be formally described in an analogous manner to electrical circuits and Ohm's law [53]. Consider first a tube under vacuum, well below the viscous flow pressure, in the molecular flow regime ($\lesssim 0.1$ Torr). The conductance C of this tube is given by the equation

$$C_{tube} \propto \frac{d^3}{l}, \quad (2.4)$$

where d is the tube diameter and l is its length. Conductance C is in units of a volume flow rate (L s^{-1}), and sets the throughput

$$Q = C\Delta P \quad (2.5)$$

through a tube with pressure differential ΔP across the length l . Reducer nipples allow pipes of various dimensions to be connected, and in the limiting case of the zero-length reducer flange, the conductance is treated by considering an aperture

instead of a tube:

$$C_{\text{aperture}} \propto d^2. \quad (2.6)$$

The equivalent conductance of elements joined in parallel and in series is totaled in the same way as electrical conductors. It is clear, therefore, that short, wide tubes are best to increase pumping power at the ion trap. The higher pumping power reduces the amount of background gas which is produced by outgassing of all elements within the chamber. A getter cartridge in the form of St 172 (Zr-V-Fe) stacked disks pumps N_2 , CO , and H_2 at a rate between 100 and 300 L s^{-1} , while an ion pump at 20 L s^{-1} is able to pump virtually all gases and vapors. The speed at which these pump on the ion trap is governed by the conductance of the chamber, and the reducer nipple that lead between the elements. The total conductance, from air at room temperature

$$C_{\text{tube,air}} \approx \frac{d^3}{l} \times 12.1 \frac{\text{L}}{\text{s cm}^2} \quad (2.7)$$

$$C_{\text{aperture,air}} \approx d^2 \times 11.6 \frac{\text{L}}{\text{s cm}^2} \quad (2.8)$$

$$C_{\text{total}} = \left(\frac{1}{C_{\text{tube,air}}} + \frac{1}{C_{\text{aperture,air}}} \right)^{-1}, \quad (2.9)$$

is about 70 L s^{-1} . Between the conductance and pumping speed of both pumps, the total system speed is

$$S = \left(\frac{1}{S_{\text{pump}}} + \frac{1}{C_{\text{total}}} \right)^{-1} = \left(\frac{1}{100} + \frac{1}{70} \right)^{-1} \approx 40 \text{ L s}^{-1}. \quad (2.10)$$

This tells us that the chamber is not throttling the pumps, which would be the case if S_{pump} was much greater than C_{total} . Outgassing rates of 300 series stainless steel routinely reach 10^{-12} Torr L/s cm^2 after having been baked at 250°C (higher

than our usual 200°C, but similar) for more than 15 hours [54]; if we estimate our chamber surface area at 200 cm², the total outgassing throughput is $Q = 2e^{-10}$ Torr L/s. Using the throughput relationship

$$Q = PS, \tag{2.11}$$

the estimated final pressure would therefore be $P = 5 \times 10^{-12}$ Torr. This gives us some margin of error and indeed allows pressures deep into the UHV regime to be reached—we observe a pressure of $\sim 10^{-11}$ Torr in our system. As added assurance, NEG ribbon and getter pellets of the same material as the cartridge sit inside the spherical octagon. Although these are activated through the bakeout process alone, which takes them to a lower maximum temperature than achieved by the resistive heating of the cartridge, they will still provide additional pumping.

The ion trap itself was assembled by hand from a Macor holder and 4 gold-plated blade electrodes (Fig. 2.3). The blades were laser machined by Laser Micromachining Ltd. and subsequently coated by Sandia National labs. The blades are identical, except that the two rf blades are coated such that all 5 segments are shorted together, while the static blades have no connection between segments. The blades are wired using gold ribbon and wire bonding, with wire extensions consisting of Kapton coated wire. Each segment of the static blades is wired to the 15-pin feedthrough and filtered externally, before it is connected to a static voltage supply. The static blade segments are also capacitively coupled to a ground wire in order to filter rf pickup. Treating the ion trap as a simple capacitor, the system is

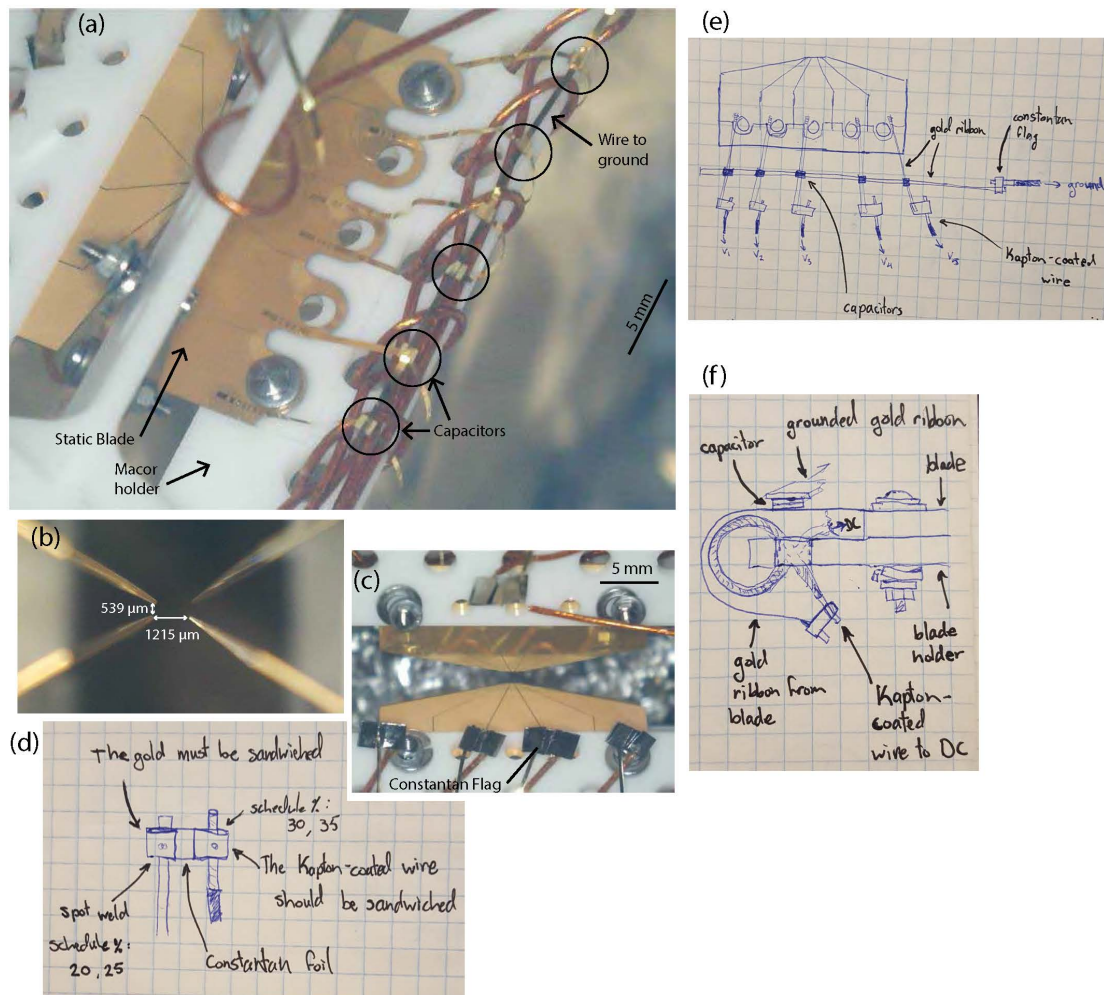


Figure 2.3: Blade ion trap photographs and sketches. The trap was assembled in house. Filters were assembled by a series of wire bonds and spot welds between Constantan foil (used for its high resistance, which is useful for spot welding), gold foil wire, capacitors and the blade segments.

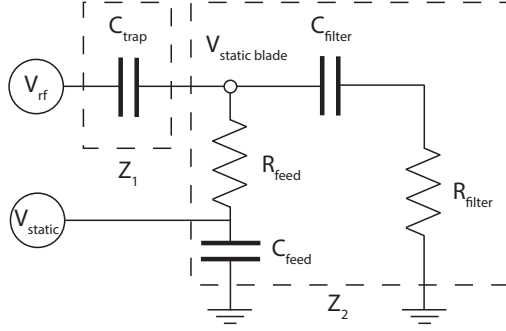


Figure 2.4: Circuit diagram of in-vacuo rf filter. This filter is constructed of the elements shown in Fig. 2.4, and is designed to reduce pickup on the static blades from the rf blades caused by a non-negligible resistance R_{feed} between the static blades and ground (primarily the feedthrough).

roughly equivalent to the voltage divider circuit diagram in Fig. 2.4, with

$$Z_2 \approx \left(\frac{1}{Z_{C,\text{filter}} + Z_{R,\text{filter}}} + \frac{1}{Z_{R,\text{feed}} + Z_{C,\text{feed}}} \right)^{-1}. \quad (2.12)$$

The impedance Z_2 is the complex load on the trap and rf drive, and $Z_{R,\text{feed}} = R_{\text{feed}} \approx 30 \Omega$ (due to the feedthrough and wire length), while $|Z_{C,\text{feed}}| = \frac{1}{\omega_{rf} C_{\text{feed}}} \approx 0.01 \Omega$ and can be ignored. The resistance to ground $Z_{R,\text{filter}} = R_{\text{filter}} \ll 1 \Omega$ and can also be ignored when $|Z_{C,\text{filter}}| = \frac{1}{\omega_{rf} C_{\text{filter}}} \gtrsim 1 \Omega$. It is clear that choosing the in-vacuo capacitor large enough allows us to ignore the resistance of the feedthrough. For this experiment, the in-vacuo capacitor has a value of 800 pF and so $|Z_{C,\text{filter}}| = \frac{1}{\omega_{rf} C_{\text{filter}}} \approx 10 \Omega$. Therefore, $|Z_2| \approx 10 \Omega$. The trap capacitance $C_{\text{trap}} \approx 10$ pF, and so $|Z_1| \approx 800 \Omega$. The rf pickup on the static blades is then $\frac{Z_2}{Z_2 + Z_1} V_{rf} \approx 10^{-2} V_{rf}$.

Further details of the bakeout procedure, drawings of custom parts, and exact trap and oven configurations inside of the spherical octagon are discussed elsewhere [44] and recored in the group laboratory files.

2.3 Experimentation with One and Two Ions

In order to perform quantum mechanical experiments with trapped ions, a number of common laser techniques are implemented to ionize, prepare and detect the trapped ion qubit. Ionization consists of a two-color excitation of an electron to continuum. Preparation includes Doppler cooling and sometimes resolved sideband cooling [55], along with optical pumping to set the qubit in a known state. Detection consists of collecting state dependent fluorescence [56], which collapses the qubit wavefunction and allows for discrimination between the two possible outcomes. Ion fluorescence is typically collected with a lens and focused onto a PMT, while sometimes a camera is used to observe spatial information.

2.3.1 The $^{171}\text{Yb}^+$ Ion

The singly charged $^{171}\text{Yb}^+$ ion is used in these experiments involving QIP for a number of reasons including its ground state hyperfine splitting, which provides a stable and accessible microwave qubit, and its fast cycling transition, which provides high efficiency qubit readout. An abridged energy level diagram in Fig. 2.5 shows the pertinent atomic structure. The $^2\text{S}_{1/2}$ electronic ground state has a hyperfine splitting (interaction between single outer electron and spin-1/2 nuclei) of $\omega_{hf}/2\pi = 12.64281$ GHz. The $F=0$ state is used as the logical $|0\rangle$ (denoted $|\downarrow\rangle$ to avoid later confusion with motional state labels), and the $F=1, m_f=0$ state is used as the logical $|1\rangle$ ($|\uparrow\rangle$).

The excited $^2\text{P}_{1/2}$ level at $2\pi/k \approx 369$ nm has a radiative lifetime of 8.12 ns

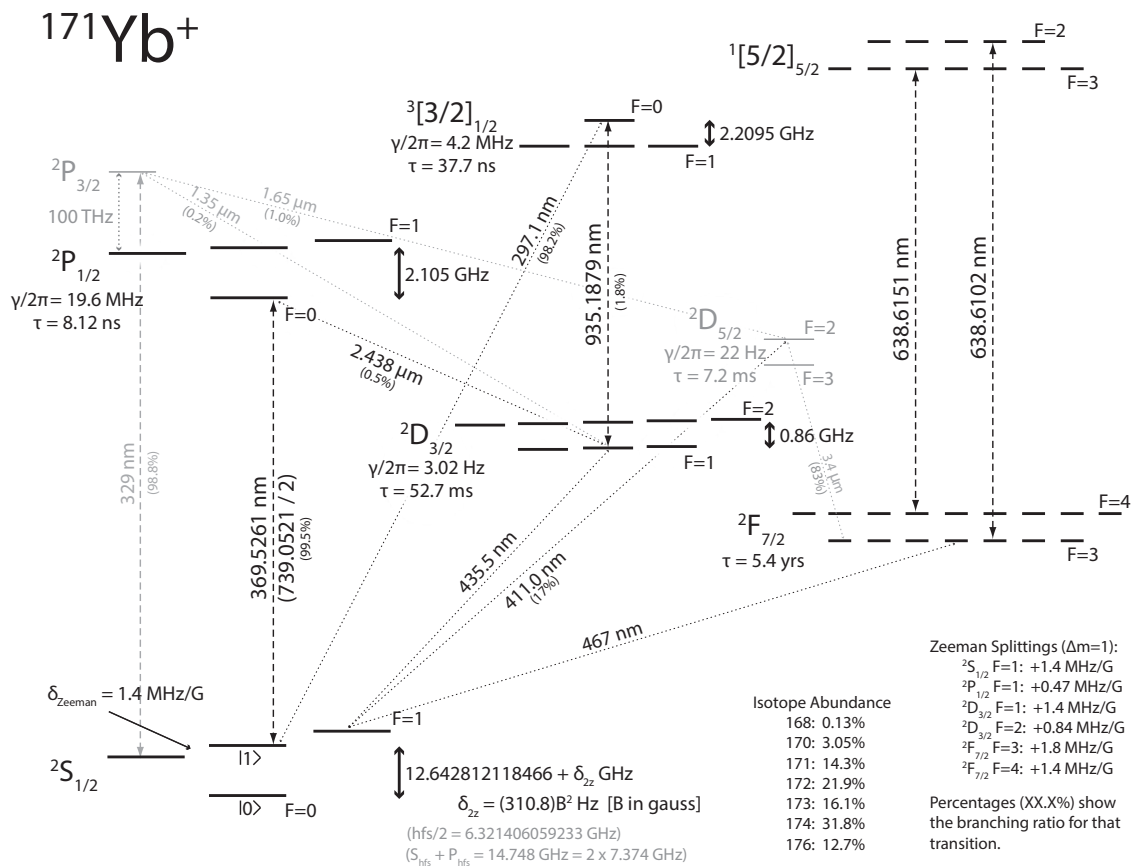


Figure 2.5: Atomic energy level diagram of $^{171}\text{Yb}^+$.

dominated by the dipole allowed decay to the ground state. The $F=0$ and $F=1$ hyperfine levels are split by 2.105 GHz, and the $F=1$ states have a Zeeman splitting of 1.4 MHz/G. A second decay mechanism from the ${}^2P_{1/2}$ manifold allows for population to fall to the ${}^2D_{3/2}$ manifold, which has a radiative lifetime of 52.7 ms before decaying to the electronic ground state. The ${}^2D_{3/2}$ state has a hyperfine splitting of 0.86 GHz. The ${}^2P_{3/2}$ level is 100 THz higher in energy than the ${}^2P_{1/2}$ level. This state is used for stimulated Raman transitions.

A lower lying ${}^2F_{7/2}$ manifold is not accessed through allowed transitions during our normal experimental operations, but sometimes becomes populated through collisions with background gas [57, 58]. This state has a radiative lifetime of over a year. The ${}^2F_{7/2}$ and ${}^2D_{3/2}$ can be excited to ${}^1[5/2]_{5/2}$ and ${}^3[3/2]_{1/2}$ bracket states, respectively. These bracket states involve excitations associated with lower lying electrons [59]. The ${}^3[3/2]_{1/2}$ level, separated from the ${}^2D_{3/2}$ manifold by $2\pi/k \approx 935$ nm, has a radiative lifetime of 37.7 ns which will predominantly decay to the ${}^2S_{1/2}$. It has a hyperfine splitting of 2.209 GHz.

2.3.2 Loading, Cooling and Detection

During loading, a beam of neutral atoms is sent through the trap (ejected from a tungsten tube, stuffed with enriched ${}^{171}\text{Yb}$ foil, that is resistively heated and aimed towards the trap), where ionization, cooling, and re-pump laser beams are focused to waists of $\sim 30 \mu\text{m}$ in the trapping region. As an atom passes through the trap, it is ionized by the beams and subsequently Doppler cooled. Ionization

of the neutral ^{171}Yb into $^{171}\text{Yb}^+$ is accomplished using 399 nm laser light resonant with the $6s_2\ ^1S_0 \leftrightarrow 6s6p\ ^1P_1$ transition in neutral Yb [60]. This isotope selective excitation allows a second photon from the cooling beam at 369 nm to drive the electron to the continuum, leaving an ion in the trapping region.

Doppler cooling the ion is achieved by applying light that is red-detuned of the $^2S_{1/2}, F=1 \leftrightarrow ^2P_{1/2}, F=0$ transition (Fig. 2.5), which scatters at a rate of [15]

$$\Gamma_c(\Delta) = \frac{s \frac{\gamma}{2}}{1 + s + \frac{4\Delta^2}{\gamma^2}}, \quad (2.13)$$

where Δ is the laser detuning from resonance, γ_c is the decay rate, and $s = \frac{I}{I_{sat}} = 2\Omega_c^2/\gamma_c^2$ is the fractional saturation intensity of the transition (Ω_c is the resonant Rabi frequency). When the Doppler width is much less than the natural linewidth of the transition, and the light is detuned by $\Delta_{min} = \frac{\gamma}{2}\sqrt{1+s}$, the minimum achievable energy (the Doppler limit) along a single dimension is given by [15]

$$E_{min} = \frac{\hbar\gamma}{4}\sqrt{1+s}. \quad (2.14)$$

These laser interactions obey the dipole transition selection rules [61]

$$\Delta F = 0, \pm 1 \quad (2.15)$$

$$F = 0 \leftrightarrow F' = 0 \quad (2.16)$$

$$\Delta M_F = 0 \text{ for } \pi \text{ light} \quad (2.17)$$

$$\Delta M_F = \pm 1 \text{ for } \sigma^\pm \text{ light.} \quad (2.18)$$

While the ion cycles through this transition, it can off-resonantly excite the $^2P_{1/2}, F=1$ levels (with a probability that can be calculated from Eq. 2.13), which may

then decay to the ${}^2S_{1/2}$, $F=0$ or ${}^2S_{1/2}$, $F=1$ states. If it falls into the ${}^2S_{1/2}$, $F=0$ state, sidebands at 14.74 GHz (the hyperfine splitting of the 12.6 GHz qubit and 2.1 GHz ${}^2P_{1/2}$ levels combined; generated as the second order sideband from a resonant EOM) will drive the ${}^2S_{1/2}$, $F=0 \leftrightarrow {}^2P_{1/2}$, $F=1$ transition, giving the atom more chances to decay back into the ${}^2P_{1/2}$, $F=1$ manifold and continue the cooling cycle.

In addition to these 369 nm transitions, the atom may also decay from the ${}^2P_{1/2}$, $F=0$ state to the metastable ${}^2D_{3/2}$, $F=1$ manifold (lifetime of 52.7 ms) with a probability of 0.005. The Doppler cooling transition is cycled thousands of times during initialization, and the atom will fall to the ${}^2D_{3/2}$, $F=1$ states with a high probability. To solve this problem, a 935 nm "re-pump" laser, with sidebands at 3.1 GHz to address all hyperfine levels, excites the ${}^2D_{3/2} \leftrightarrow {}^3[3/2]_{1/2}$ transition. The ${}^3[3/2]_{1/2}$ manifold has a 37.7 ns lifetime and decays with probability 0.982 back to the cooling transition, thus requiring only a few cycles to "re-pump".

Preparation of the $|\downarrow\rangle$ state is achieved through optical pumping [56]. Light resonant with the ${}^2S_{1/2}$, $F=1 \leftrightarrow {}^2P_{1/2}$, $F=1$ will eventually trap the population in the ${}^2S_{1/2}$, $F=0$ ($|\downarrow\rangle$) state with only a small probability of depopulation through 12.6 GHz-off-resonant excitation of the ${}^2P_{1/2}$, $F=1$ state. This process is performed while the cooling light is turned off.

State detection is an incoherent process by which the population in each qubit level is determined. Light resonant with the ${}^2S_{1/2}$, $F=1 \leftrightarrow {}^2P_{1/2}$, $F=0$ transition is scattered, or not scattered, from the ion and collapses the state vector to either $|\uparrow\rangle$ or $|\downarrow\rangle$, respectively. This is a manifestation of the quantum measurement phenomenon known as the wave function collapse and, as mentioned, is the basis of our

measurement scheme. Continued application of this light produces a state dependent fluorescence signal [56], by which the number of photons scattered during a given period signals which state the ion has collapsed to. This must be performed in multiple repeated experiments (each experiment consists of cooling, qubit state preparation, coherent control of qubit and ion motion, and measurement) to produce the probability distribution of the qubit state (i.e. a measurement in each experiment returns only a $|\uparrow\rangle$ or a $|\downarrow\rangle$).

Additionally, experiments are run with a magnetic field applied to the ion, providing a clear quantization axis and splitting the $F \neq 0$ hyperfine levels. This Zeeman splitting of 4 MHz (2.9 G x 1.4 MHz/G) prevents the ion from significant coherent population trapping during cooling and detection, but is modest enough to stay near resonance for efficient cooling from a single laser.

Fluorescence from trapped ions is collected using a lens and PMT or camera. The lens is positioned to collect light from the reentrant window on top of the vacuum chamber, as seen in Fig. 2.6(a). The histogram, Fig. 2.6(b), shows the number of occurrences of a number of photons collected during an extended detection cycle after zero, one, and two trapped ions are prepared in the $|\uparrow\rangle$ state. The "zero" histogram is taken with no ions in the trap, and applying detection light to simulate scattering from trap electrodes during measurement. We measure no photon counts the majority of times (14932 occurrences of no counts in Fig. 2.6(b)), while the probability of counting a single photon is about the same when a single bright ion is trapped. The probability of counting two photons when there is no ion is essentially zero (much lower than counting two photons with a single bright ion).

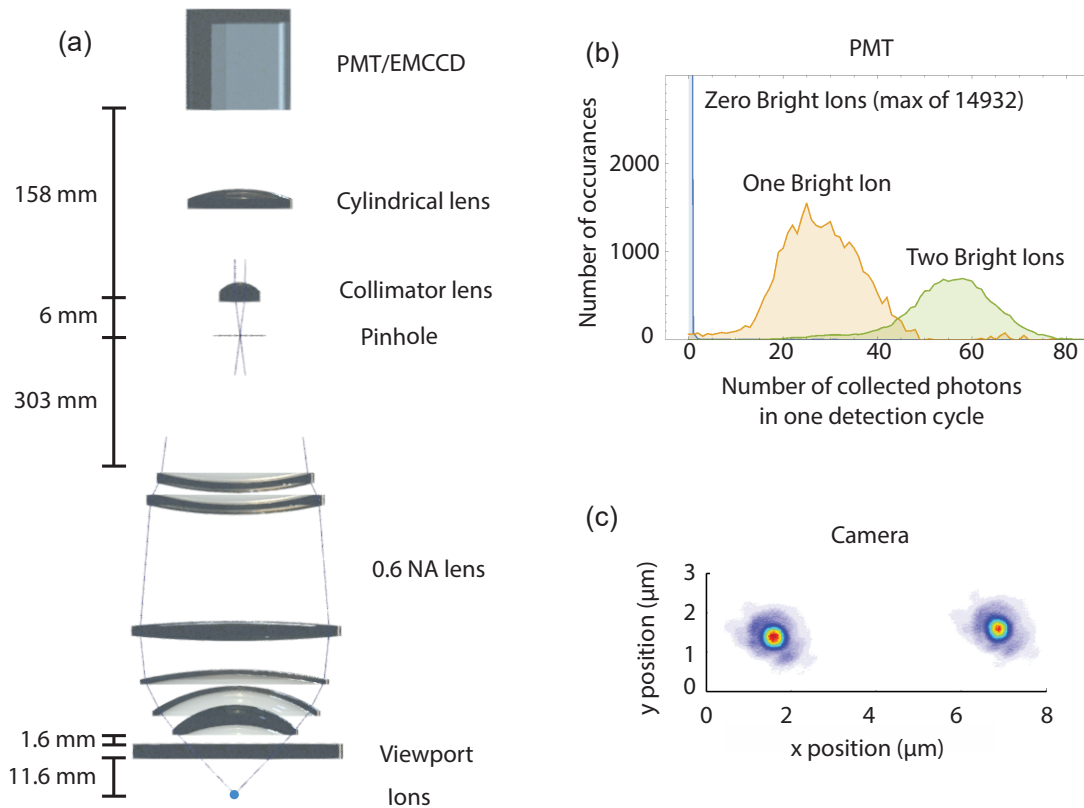


Figure 2.6: Ion detection and imaging. (a) Schematic diagram of the ion location, viewport, 0.6 NA lens stack, pinhole, collimator lens, cylindrical lens and the PMT or EMCCD. The lens stack is made by Photon Gear [43, 62], and is designed to focus onto the pinhole. The cylindrical lens is used to correct astigmatism from the 0.6 NA lens stack and viewport. The collimator lens is focusing light from a small solid angle, and so a plano-convex lens suffices. (b) Histograms are used to determine the qubit state of one or two ions. Light collected on the PMT during a single experimental detection cycle (scattering from the ion) produces a certain number of counts at the PMT. This number comes from one of three distributions localized around the average number of photons when there is zero, one or two fluorescing ions. By repeating the experiment many times, we build up a picture of this distribution and can determine the qubit state populations after an experiment (with this method, we cannot tell which ion is bright if there is only one fluorescing). (c) Light from two fluorescing ions collected on a camera gives spacial information about the ions.

So When working with a single ion, discrimination between the "bright" ($|\uparrow\rangle$) and "dark" ($|\downarrow\rangle$) state is achieved by calling any detection cycle in which 0 or 1 counts was detected as $|\downarrow\rangle$. Any other number of counts is considered as measuring a $|\uparrow\rangle$. By contrast, we see significant overlap between the one and two bright ion histograms in Fig. 2.6, and so a simple thresholding method does not work. Instead, we use these extended exposure (extended to reduce noise) detection histograms to fit a set of three Poisson distributions as a calibration. Then, after a set of a experiments, we fit the measurement histogram to a weighted sum of the three calibrated Poisson distributions and determine the probability of zero, one, and two bright ions from the weight of each coefficient. Figure 2.6(c) shows a high resolution image of two trapped ions taken by collecting the fluoresced photons on a camera. The details of this imaging are discussed further in Chapter 7.

2.3.3 Rotating Ion Trap Axes

In most of our experiments, we use a laser beam to coherently excite the external motion of the trapped ion through Raman transitions. Knowing the coupling strength of this laser to each axis of ion motion is critical for high fidelity operations, such as atom interferometry, multi-qubit logic gates and others. One way to handle this issue, and probably the simplest, is to couple the laser to just one axis of motion. Because the laser beam is constrained to come through the trap at angles corresponding to available windows in the chamber, fine adjustments of the mode coupling are made by rotating the axis of the trapping potential. Figure 2.7

shows how the axes of the trap can be rotated and the relative strengths tuned for different trap geometries. The trap used in this experiment is not square, and so we are not able to make the potential degenerate, but we are able to rotate it so that the beam only couples to one axis of motion.

2.3.4 Doppler Cooling along multiple Axes

So far, the discussion of Doppler cooling has been restricted to a single dimension. At low laser beam intensities (compared to saturation), which is the regime of typical operation, the concepts are easily expanded to consider cooling along all three directions. Figure 2.8 gives an intuitive (albeit classical) understanding of how absorption (or emission) of a single photon will affect the motion of a trapped ion in two dimensions (similar to three dimensions). First, consider the two radial modes of motion, where the secular frequency along the x-direction is different than in the y-direction. This is called non-degenerate for an obvious reason. If a photon moves the ion (starting from rest at the center of the trap) along only the x- or y-direction, the resulting motion of free evolution is restricted to a single dimension (Fig. 2.8(a)). If the photon pushes the ion at an oblique angle to the axes (Fig. 2.8(b)), then motion is not only excited along both axes, but the trajectory is two-dimensional. This implies that a single laser beam at an oblique angle to the trap axes of a non-degenerate trap can Doppler cool all three degrees of freedom (or, a Raman beam can push the ion into three-dimensional trajectories). Finally, if the secular frequency is equal in all directions (degenerate), then a single photon can

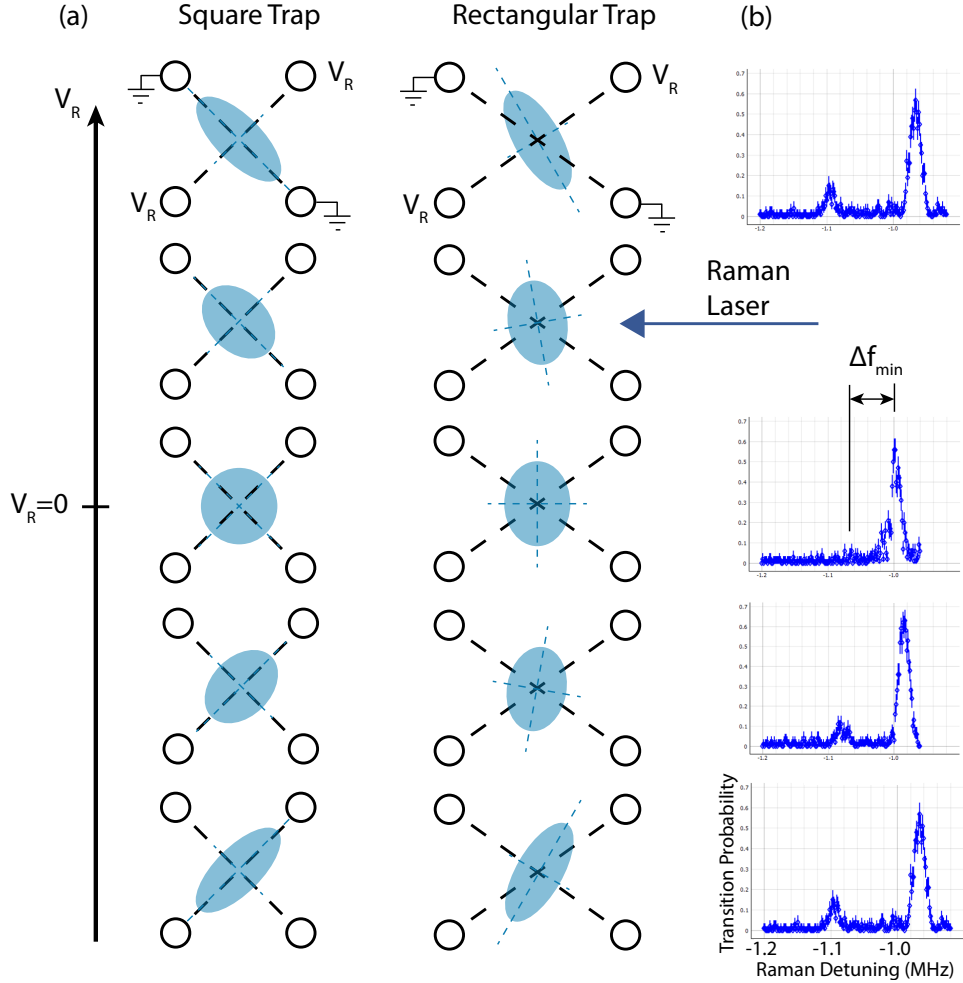


Figure 2.7: Adjusting the trap axes. (a) Trap electrode geometry determines how the trapping potential will look. For a square system of four electrodes, modifying the relative static voltage (V_R , a bias on the rf signal ranging from about -10 V to +10 V) while maintaining the ion at the trap center will change the ellipticity of the trapping potential, but will not rotate it. Doing the same thing on a trap that is not square will rotate the axis while modifying the ellipticity. The blue ellipse suggests the nature of the equipotential lines in the trap, and the light dashed lines along the major and minor axes of the ellipses indicate the direction of the trap modes. (b) The trap mode frequencies can be seen spectroscopically by observing the motional sidebands [55] of the ion with a Raman laser. Here we see the transition probability in a rectangular trap as a function of detuning from the carrier of a Raman transition. For $V_R \neq 0$, the (red) sidebands of both modes are visible (the relative coupling is not equal and gives rise to the unequal heights of the peaks). For $V_R \approx 0$, the modes are separated by the minimum allowable distance Δf_{min} , determined by the trap geometry (the left peak approaches zero because the Raman beam is along the direction drawn, and does not couple to the weaker mode when $V_R = 0$).

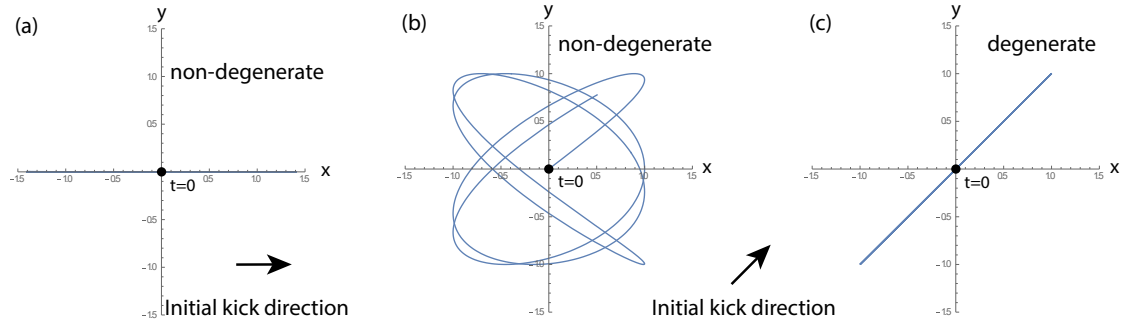


Figure 2.8: 2D ion trajectory from scattering a single photon. (a) In a non-degenerate trap, an ion kicked along one principle axis will stay on that axis. This is important both for cooling and for driving SDKs. (b) In a non-degenerate trap, an ion kicked off-axis will undergo a trajectory through two (or three) dimensions. This means a single laser beam can cool in two (or three) dimensions, and a single SDK can excite motion in two or three dimensions. (c) A single kick in any direction of a degenerate trap will only excite one dimension of motion.

only excite one-dimensional motion. Thus, a completely degenerate trap requires three beams to cool in all dimensions, or two beams if two of the modes are degenerate. The Doppler limit for all configurations is discussed in detail elsewhere [63].

When multiple ions are trapped, we have found that higher intensity laser light is often required to maintain the chain of ions over the course of minutes and hours. We add this light in as an additional cooling step, before lower intensity Doppler cooling takes the ion to the Doppler limit. The high intensity light is also detuned to account for power broadening. This process is altered quite often, so the exact power and detuning change from week to week, but the intensity is typically at least twice that of saturation. We believe this additional light is required because background gas collisions can displace the ion chain enough to cause the trap to heat the chain [52].

2.4 Second Ionization to Create $^{171}\text{Yb}^{2+}$ with Laser Pulses

Recent results have suggested the usefulness of highly charged trapped atoms for use in atomic clocks, quantum information and measuring the fine structure constant [64]. Although this was not an area of intended research during my PhD, we did encounter a method for reliable double ionization of ^{171}Yb using a pulsed 355 nm laser. The details of this interaction were not deeply investigated because the laser causing this transition stopped functioning just days after seeing the process. The ionization was an undesirable effect of the laser in this case, but its significance is not lost on us.

We investigate second ionization using a mode-locked 355 nm laser (High-Q Picotrain) with 6 W average power and transform limited pulse of duration $\tau \approx 10$ ps. We believe the ion undergoes a multi-step process by which it is excited and decays to the long-lived $^2F_{7/2}$ state (Fig. 2.5) before a second excitation drives the outer electron to the continuum. Evidence for this comes from an experiment where we trap three ions in a linear chain. To the middle ion, we apply a series of SDK operations during a simple experiment–Doppler cooling, SDKs, detection–which is repeated. (Single pulses with no motional coupling instead of SDKs should have the same effect, but we did not get a chance to try.)

In order to show that the ion enters the $^2F_{7/2}$ state before second ionization, we apply a series of SDKs that is sufficiently large enough such that the $^2F_{7/2}$ will be populated, but sufficiently small enough that we will detect the population change before ionization occurs. This is done as follows: when the middle ion goes dark

without pushing the outer ions farther away, we apply a pump beam at 638 nm to depopulate the ${}^2F_{7/2}$ state [56]. If the ion returns to its ground state where we can cool and detect it, we presume it was in the ${}^2F_{7/2}$ state. We indeed observe population of the ${}^2F_{7/2}$ state (rate not measured). We then apply a short series of pulses which takes the ion to the ${}^2F_{7/2}$ state, but instead of pumping out, we apply another series of SDKs and observe second ionization. It therefore appears that the atom only undergoes second ionization from the ${}^2F_{7/2}$ state.

To observe these processes we apply the short series of SDKs while looking at a continuous camera image feed to monitor the spatial configuration of the chain. When the center ion goes dark, but the chain spacing remains the same as when all three ions were bright (Fig. 2.9(a),(b)), the ion is in the ${}^2F_{7/2}$ state. When the outer ions move farther apart, the image indicates that the middle ion has been doubly ionized (Fig. 2.9(c),(d)). This should give a good estimate of the ionization rate and the path it takes, but we were unable to complete this study.

For added assurance that we are seeing double ionization, we fit the images along the axis to determine their positions (Fig. 2.9(b),(d)). Consider the forces acting on one of the two end ions at position x in equilibrium

$$F = \frac{q^2}{(2x)^2} + \frac{qq_c}{(x)^2} - Eqx = 0, \quad (2.19)$$

where q is the charge of the end ions, q_c is the charge of the center ion, and E is the electric trapping field gradient. If we let x_e be the ion position when the middle ion is singly charged ($q_c = e$), and x_{2e} be the position for $q_c = 2e$, we can write down

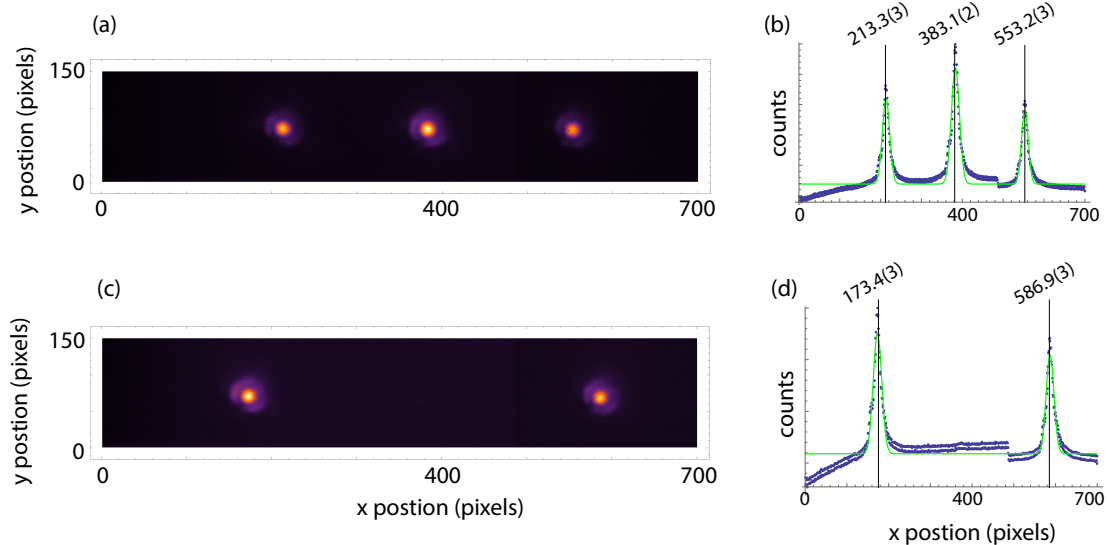


Figure 2.9: Observation of double ionization. (a) ICCD image of three trapped, singly charged ions using the lens system described in Fig. (6.1). When the middle ion is in the $^2F_{7/2}$ state, it appears dark in the image (not shown). (b) x-position dependent counts of the ion image in "(a)" (blue points) with fit to Gaussian peaks (green line). The fit is used to determine the position of each ion, labeled above peaks. The dip in counts near pixel 500 is from a defect in the CCD chip. (c) ICCD image of three trapped ions, the middle is doubly charged and the outer two are singly charged. The middle ion appears dark because it does not fluoresce from the illuminating light. (d) x-position dependent counts of the ion image in "(c)" (blue points) with fit to Gaussian peaks (green line). The fit is used to determine the position of each ion, labeled above peaks.

the simple relationship

$$\frac{x_{2e}}{x_e} = \left(\frac{9}{5}\right)^{1/3} \approx 1.216. \quad (2.20)$$

The ratio of the measured values of x_{2e} and x_e (from values shown in Fig. 2.9(b),(d)) yields 1.217(3), within error of Eq. 2.20, and strongly suggests that the center ion is double ionized.

2.5 Imparting Ultrafast Laser Forces to Atoms

This section describes the method by which a pulse of light couples internal and motional degrees-of-freedom of a trapped $^{171}\text{Yb}^+$ ion. These processes are the basic building blocks of much of the research described in this thesis. Much of our understanding was explicitly laid out by Wes Campbell and Jonathan Mizrahi [2, 32, 44]. Because the interactions are crucial to understanding how the results presented have come about, I will discuss the relevant details and consequences in the context of how I have worked on the whole project while leaving the first-principles derivation as it stands in other works.

2.5.1 Spin-Dependent Kick Generation

Consider a single atomic $^{171}\text{Yb}^+$ ion in a linear rf Paul trap, in a uniform magnetic field \mathbf{B} oriented along the x -axis of the ion trap and under the presence of a laser beam with time-dependent electric field envelope $X_\ell(t)$. Single photon transitions between the qubit levels 0: $F=0$ and 1: $F=1, m_f=0$, and the $^2P_{1/2}$ levels 2: $F=0$; 3: $F=1, m_f=-1$; 4: $F=1, m_f=0$; 5: $F=1, m_f=1$ (recall Fig. 2.5) have single

photon Rabi frequencies

$$g_{ij}^\ell(t) = -X_\ell(t)e^{-i\phi_\ell}\langle i|\boldsymbol{\mu}\cdot\hat{\boldsymbol{\epsilon}}_\ell|j\rangle, \quad (2.21)$$

where i and j are indices for the state (0-5), ℓ is the index of the laser beam (one beam for now, but two next), $\boldsymbol{\mu}$ is the electric dipole moment, and $\phi_\ell = k_\ell x + \phi_0^\ell$ is the position-dependent phase of the photon with wavenumber k_ℓ and offset ϕ_0^ℓ . The photon polarization vector $\hat{\boldsymbol{\epsilon}}_\ell = \cos(\beta_\ell)\hat{\sigma}^+ + \sin(\beta_\ell)\hat{\sigma}^-$ is defined by the parameter β_ℓ (for instance, $\beta_\ell = \pi/4$ is π -light).

Now consider a single 355 nm laser pulse is divided and applied to the ion simultaneously with pulses counter-propagating along \mathbf{B} . Choosing the quantization axis along the magnetic field direction, there is no π -light, and only the transitions $0 \leftrightarrow 3$, $1 \leftrightarrow 3$, $0 \leftrightarrow 5$, and $1 \leftrightarrow 5$ are possible. The total Rabi frequency for two-photon Raman transitions is therefore

$$\Omega = \frac{1}{2\Delta}(g_{03}^{1*} + g_{03}^{2*})(g_{13}^1 + g_{13}^2) + \frac{1}{2\Delta}(g_{05}^{1*} + g_{05}^{2*})(g_{15}^1 + g_{15}^2), \quad (2.22)$$

where $\Delta/2\pi = 33$ THz is the detuning of the laser light from the ${}^2P_{1/2}$ (which is much greater than the Zeeman and hyperfine splitting, and so is considered the same for each of the Raman Rabi frequencies). We see that transitions through level 3 are only made by $\hat{\sigma}^-$ light, while transitions through level 5 are only made by $\hat{\sigma}^+$ light. The total Rabi frequency becomes

$$\Omega(t) = \frac{\gamma^2}{12\Delta} \left[\frac{I_1(t)}{I_{sat}} \cos(2\beta_1) + \frac{I_2(t)}{I_{sat}} \cos(2\beta_2) + \sqrt{\frac{I_1(t)I_2(t)}{I_{sat}^2}} \cos(\beta_1 + \beta_2) (e^{i(2k\hat{x} + \phi_0)} + e^{-i(2k\hat{x} + \phi_0)}) \right], \quad (2.23)$$

where the single photon Rabi frequencies have been computed [61], $I_\ell(t) = (X_\ell(t)c\epsilon_0/2)^2$ are the beam intensities, $I_{sat} = \hbar\omega_0^3\gamma/(12\pi c^2)$ is the saturation intensity, $\phi_0 = \phi_1 - \phi_2$ is the relative phase offset of the two beams, γ is the excited state decay rate (~ 20 MHz), and $k_1 - k_2 = 2k$.

In these experiments, we apply the counter-propagating beams linearly polarized with mutually orthogonal configuration (lin-perp-lin) that arrive simultaneously at the ion ¹. Equivalently stated, $\beta_1 = \pi/4$ and $\beta_2 = -\pi/4$, and so only the last term in Eq. 2.23 survives. The magnitude of the Rabi frequency in Eq. 2.23 should also include contributions from the $^2P_{3/2}$ F=1 levels, which is not computed here but follows the same process [44]. This produces a Hamiltonian (including the qubit energy) of the form

$$\hat{H}(t) = \sqrt{\Omega_1(t)\Omega_2(t)} \cos[2k\hat{x} + \phi_0] \hat{\sigma}_x + \frac{\omega_{hf}}{2} \hat{\sigma}_z, \quad (2.24)$$

where $\Omega_1(t)$ and $\Omega_2(t)$ are the time-dependent effective Rabi frequencies of the counter-propagating pulses (not a physical process because a single beam does not drive transitions, but represents the beam strength), and $\hat{\sigma}_{x,z}$ are the Pauli spin operators of the qubit [44].

If we make the approximation that the effective Rabi frequencies are applied as pulses which are infinitely short in time compared to qubit and trap evolution (this has been proven to be a fine approximation [44]), and consider a string of these

¹overlapping the pulses is not difficult—each pulse is about 3 mm long, which is manageable for any micrometer.

pulses arriving at times t_l , the Hamiltonian becomes

$$\hat{H}(t) = \theta\delta(t - t_l) \cos[2k\hat{x} + \phi(t_l)]\hat{\sigma}_x \quad (2.25)$$

$$= \theta\delta(t - t_l) \cos[\eta(\hat{a} + \hat{a}^\dagger) + \phi(t_l)]\hat{\sigma}_x, \quad (2.26)$$

where the Rabi frequencies have become Dirac delta functions with pulse area θ , the position operator \hat{x} has been substituted for the raising (\hat{a}^\dagger) and lowering (\hat{a}) operators and of the ion harmonic motion, and the phase of the light is $\phi(t_l) = \phi(0) + \omega_A t_l$. The Lamb-Dicke parameter

$$\eta = 2kx_0, \quad (2.27)$$

(≈ 0.2 in all our experiments) is something that comes up a lot in these atom-laser interactions, where $x_0 = \sqrt{\frac{\hbar}{2m\omega}}$ is the ground state spread of the harmonic oscillator.

The time evolution of this interaction [44]

$$\hat{U}_{t_l} = \exp\left(i \int \hat{H}(t) dt\right) \quad (2.28)$$

$$= \exp(i\theta \cos[\eta(\hat{a} + \hat{a}^\dagger) + \Delta\phi(t_l)]\hat{\sigma}_x) \quad (2.29)$$

$$= \sum_{n=-\infty}^{\infty} i^n J_n(\theta\hat{\sigma}_x) e^{in[\eta(\hat{a} + \hat{a}^\dagger) + \Delta\phi(t_l)]} \quad (2.30)$$

$$= \sum_{n=-\infty}^{\infty} i^n J_n(\theta) e^{in\Delta\phi(t_l)} \hat{\mathcal{D}}[inn\eta] \hat{\sigma}_x^n, \quad (2.31)$$

produces a phenomenon known as Kapitza-Dirac scattering where the ion is diffracted into an infinite number of momentum states by the polarization gradient of the light. The polarization gradient arises from the lin-perp-lin configuration of the laser beams [61]. $J_n(\theta)$ is the n^{th} order Bessel function of the first kind, and the displacement operator $\hat{\mathcal{D}}[\alpha] = \exp(\alpha\hat{a}^\dagger - \alpha^*\hat{a})$, where the imaginary axis is momentum \hat{p} and the real axis is position \hat{x} . Notice also that the diffracted orders

are associated with alternating spins. Although this appears to be a complicated result, there is a way to simplify it. We do so by stringing together multiple pulses arriving at different times t_i and offsetting the frequency of the opposing light paths by an amount ω_A provided by a set of acousto-optic modulators. This focuses the Kapitza-Dirac diffractions into a nearly single, spin-dependent order, producing a spin-dependent kick (SDK). As far as we know, the only way to solve the problem of determining proper pulse timings is by numerical simulation, and this is an active area of research for our theory collaborators. For the experiments shown here, we have made two simplifying assumptions and found surprising good solutions. The assumptions are:

- 1) Every pulse has the same pulse area $\theta = \frac{\Theta}{N}$. This simplifies the experimental apparatus.
- 2) The SDK occurs much faster than a trap period.

The reason for these will become apparent as I run through a simple, but fairly effective, simulation as an example of what we do to solve for delay settings. There are several parameters to play with: pulse area θ , AOM frequency shift ω_A , and pulse timings. First lets say we are going to have eight pulses. (Eight because it is manageable but effective using our beam splitter and delay setup.) The schematic for this is described in the next section (Fig. 2.11). If eight pulses are used, lets try the intuitive pulse area $\theta = \pi/8$ so that the total effect is a full spin flip for each diffracted order ². Finally, lets say that population totaling $\lesssim 0.001$ is not worth

²Remember, this should all be played with for complete results. This is an area of research in its own right, and we did not explore all possible options but are working on expanding the search.

accounting for. This means we can probably drop orders $J_{\pm 3}(\pi/8)$ and above from Eq. 2.31 for a reasonable estimation:

$$J_0(\pi/8) = 0.96; J_{\pm 1}(\pi/8) = \pm 0.19; J_{\pm 2}(\pi/8) = 0.019; J_{\pm 3}(\pi/8) = \pm 0.0012.$$

Now we can try a simulation, in which free evolution between each kick is governed by the evolution operator

$$\hat{U}_{fe}(t) = \exp(-i\omega_{hf}t\hat{\sigma}_z/2). \quad (2.32)$$

From equation 2.31, the truncated pulse operator is

$$\begin{aligned} \hat{U}_{t_l} \approx & J_0(\pi/8) \\ & + iJ_1(\pi/8) \left(e^{i\omega_{At_l}\hat{\mathcal{D}}[i\eta]} + e^{-i\omega_{At_l}\hat{\mathcal{D}}[-i\eta]} \right) \hat{\sigma}_x \\ & - J_2(\pi/8) \left(e^{2i\omega_{At_l}\hat{\mathcal{D}}[2i\eta]} + e^{-2i\omega_{At_l}\hat{\mathcal{D}}[-2i\eta]} \right), \end{aligned} \quad (2.33)$$

in which the initial optical phase has been absorbed into a non-zero time-of-arrival for the first pulse, and subsequent optical phase evolution follows ω_{At_l} (recall t_l is the arrival time of the l th pulse). The final state after a pulse train is formulated as

$$|\Psi_f\rangle = \hat{O} |\Psi_i\rangle = \hat{U}_{t_8} \hat{U}_{fe}(t_8 - t_7) \hat{U}_{t_7} \hat{U}_{fe}(t_7 - t_6) \dots \hat{U}_{t_1} |\Psi_i\rangle. \quad (2.34)$$

I think the easiest way go from here is to use matrix multiplication on a computer. We write the operators in explicit matrix form in terms of the spin and a truncated momentum basis pertaining to absorbing+emitting pairs of photons. The eigenstates of the qubit manifold are:

$$|\uparrow\rangle = \begin{bmatrix} 1 \\ 0 \end{bmatrix} \quad \text{and} \quad |\downarrow\rangle = \begin{bmatrix} 0 \\ 1 \end{bmatrix}. \quad (2.35)$$

Relevant qubit state matrices are:

$$\hat{\sigma}_x = \begin{bmatrix} 0 & 1 \\ 1 & 0 \end{bmatrix} \quad \text{and} \quad e^{-i\omega_{hf}t\hat{\sigma}_z/2} = \begin{bmatrix} e^{-i\omega_{hf}t/2} & 0 \\ 0 & e^{i\omega_{hf}t/2} \end{bmatrix}. \quad (2.36)$$

A vacuum state that has been displaced by $4\hbar k$, $2\hbar k$, 0 , $-2\hbar k$, and $-4\hbar k$ in momentum can be written as:

$$|2i\eta\rangle = \begin{bmatrix} 1 \\ 0 \\ 0 \\ 0 \\ 0 \end{bmatrix}; |i\eta\rangle = \begin{bmatrix} 0 \\ 1 \\ 0 \\ 0 \\ 0 \end{bmatrix}; |0\rangle = \begin{bmatrix} 0 \\ 0 \\ 1 \\ 0 \\ 0 \end{bmatrix}; |-i\eta\rangle = \begin{bmatrix} 0 \\ 0 \\ 0 \\ 1 \\ 0 \end{bmatrix}; |-2i\eta\rangle = \begin{bmatrix} 0 \\ 0 \\ 0 \\ 0 \\ 1 \end{bmatrix}, \quad (2.37)$$

where higher order momentum states are ignored because only a tiny amount of population spreads into them. The displacement operators written in this basis are:

$$\hat{\mathcal{D}}[2i\eta] = \begin{bmatrix} 0 & 0 & 1 & 0 & 0 \\ 0 & 0 & 0 & 1 & 0 \\ 0 & 0 & 0 & 0 & 1 \\ 0 & 0 & 0 & 0 & 0 \\ 0 & 0 & 0 & 0 & 0 \end{bmatrix}; \dots; \hat{\mathcal{D}}[-2i\eta] = \begin{bmatrix} 0 & 0 & 0 & 0 & 0 \\ 0 & 0 & 0 & 0 & 0 \\ 1 & 0 & 0 & 0 & 0 \\ 0 & 1 & 0 & 0 & 0 \\ 0 & 0 & 1 & 0 & 0 \end{bmatrix}. \quad (2.38)$$

Now all that is left is choosing ω_A , and the timings. Let us imagine we are generating 8 pulses using delay lines in the shape of Mach-Zehnder interferometers as shown in Fig. 2.11. Additionally, let us try a solution where the pulses arrive at integer multiples of the hyperfine evolution plus the AOM shift. Intuitively, this is a good starting point considering it works for a standard Raman transition using an evenly spread train of low energy pulses [65] (although there are an infinite number of

possibilities). If we set the AOM shift to $\omega_A/2\pi = 466$ MHz (arbitrary, besides being experimentally achievable, but most settings will give some good answers), and limit the maximum Mach-Zehnder arm to be less than 17 hyperfine evolutions of delay, we get a manageable set of solutions.

The best solution in this example has delay arms (in units of hyperfine evolution plus AOM evolution) of length $t_{\text{delay}}(\omega_{hf} + \omega_A)/2\pi = 7, 8,$ and 16 . For an ion initially in the state $|\Psi_i\rangle = |0\rangle \otimes (|\uparrow\rangle + |\downarrow\rangle)$ ($1/\sqrt{2}$ normalization factor ignored), the series of pulses gives

$$\hat{O} \cdot |\Psi_i\rangle = |\Psi_f\rangle \approx \begin{bmatrix} 0.001 + 0.000i \\ -0.315 + 0.948i \\ 0.019 + 0.009i \\ -0.009 - 0.024i \\ 0.013 + 0.011i \end{bmatrix} \otimes \begin{bmatrix} 1 \\ 0 \end{bmatrix} + \begin{bmatrix} 0.013 - 0.011i \\ 0.009 - 0.024i \\ 0.019 - 0.009i \\ 0.315 + 0.948i \\ -0.001 + 0.000i \end{bmatrix} \otimes \begin{bmatrix} 0 \\ 1 \end{bmatrix}. \quad (2.39)$$

This means that an ion starting in state $|\Psi_i\rangle$ will have its spin and motion entangled with high fidelity. The fidelity of the transfer to the two desired diffracted momentum orders are $|(\langle i\eta | \otimes \langle \uparrow |) |\Psi_f\rangle|^2 = 0.997$, and $|(\langle -i\eta | \otimes \langle \downarrow |) |\Psi_f\rangle|^2 = 0.997$. That is 0.3% worse than the ideal SDK operator

$$\hat{O}_{SDK} = ie^{i\phi_0} \mathcal{D}[i\eta] \hat{\sigma}_+ + ie^{-i\phi_0} \mathcal{D}[-i\eta] \hat{\sigma}_-, \quad (2.40)$$

where the phase ϕ_0 is the initial optical phase.

2.5.2 Frequency Domain Interpretation

Intuition for why certain pulse timings succeed in producing SDKs may be gained by looking at the frequency spectrum of the pulse train. In the well-understood case of a beatnote between two frequency combs coupling spin and motion [32], the condition for driving transitions is

$$f_{hf} = n f_{rep} \pm f_A \quad (2.41)$$

where both solutions \pm should not be satisfied at the same time lest the fidelity decreases. The repetition rate of the pulse train f_{rep} must be less than the bandwidth of the pulse, which must be greater than the hyperfine splitting (to drive qubit transitions) but much less than the splitting between the excited ${}^2P_{3/2}$ and ${}^2P_{1/2}$ states (lest Raman transitions will not work) [65]. A plot of these conditions is shown in Fig. 2.10(a).

An uneven pulse train will produce an uneven frequency spectrum. However, it is still true that there should be preferential absorption depending on the spin state, which comes from a beatnote existing between spectral components at the hyperfine frequency and which always has the lower frequency component in one of the beams and the higher component in the other when shifted by an AOM (Fig. 2.10(b)).

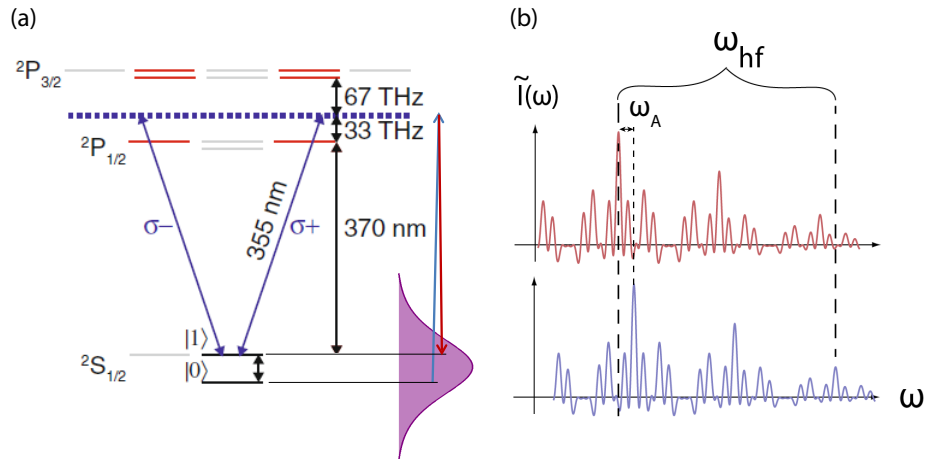


Figure 2.10: Conditions For a Spin-Dependent Kick. (a) The 355 nm mode locked laser pulse bandwidth must be greater than the hyperfine splitting. Drawn here, a single pulse bandwidth spans the hyperfine splitting of 12.6 GHz. This is not to scale with the excited states, which have a fine structure splitting of 100 THz. The pulse drives Raman transitions via off-resonantly coupling to the excited 2P states. (b) The frequency spectrum of a short train of unevenly spaced pulses and a beatnote resonant with the ground state hyperfine transition of the atom. The width of the spectrum envelop is greatly under-exaggerated to show how it drops off (proportional to the bandwidth of the laser $\sim 1/\tau$)

2.5.3 The Mode-Locked Laser

Each SDK is generated from a single 10 ps pulse of a frequency tripled, mode-locked Nd:YVO₄ at wavelength $\lambda = 355$ nm [1, 32, 33]. I have used three different lasers during my PhD, the first being a High-Q Picotrain laser with 8 W average power and an 80.16 MHz repetition rate. This laser was poorly made, and rarely functioned long enough to produce reliable data. We used this laser the first three years of my time in the group before replacing it with a 4 W average power Paladin Compact from Coherent Inc. This laser worked well for the year that we used it, but we have since moved to using a laser capable of driving single-pulse Rabi flops on multiple ions—a 24 W Paladin Advanced also made by Coherent Inc with a repetition rate of about 81 MHz. In the experiments described here, a pulse is divided into eight pulses using a series of beam splitters and delays in a Mach-Zehnder interferometer configuration (Fig. 2.11) and then applied to the ion in a linear-perpendicular-linear fashion to produce the spin-dependent displacement [32]

$$\hat{O}_{SDK} = e^{i\phi_\lambda} \hat{\sigma}_+ \hat{\mathcal{D}}[i\eta] + e^{-i\phi_\lambda} \hat{\sigma}_- \hat{\mathcal{D}}[-i\eta]. \quad (2.42)$$

The phase ϕ_λ is an optical phase that is assumed to be stable during the course of one experiment, but random over multiple experiments due to slow mechanical and other noise on the optics. The optical phase ϕ_λ cancels when an even number of applications of the operator \hat{O}_{SDK} are used during an experiment.

Each of the Paladin lasers produce transform limited pulses with a temporal profile $\text{sech}^2(t/\tau_p)$. At an average power of 24 W, a repetition rate of 80 MHz, and

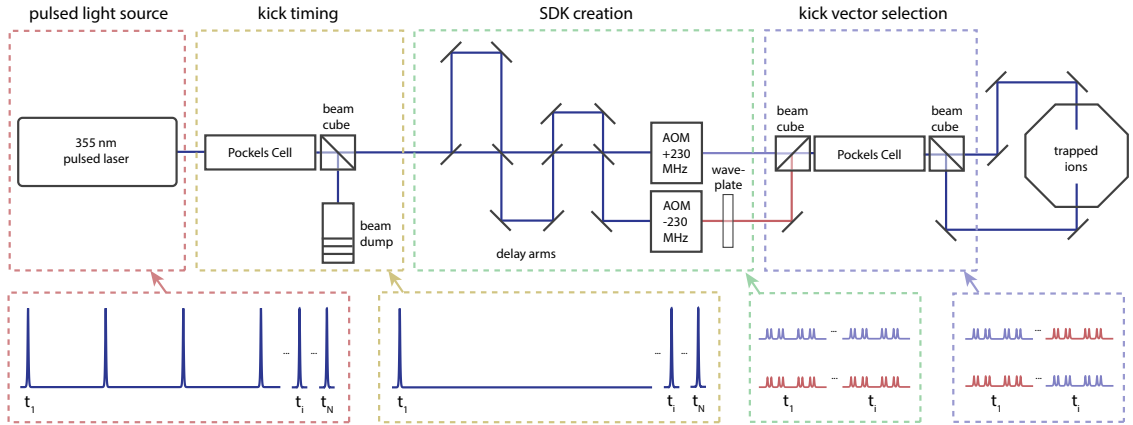


Figure 2.11: Experimental setup of Raman laser. The mode-locked Raman laser beam path is broken into four sections. The first section (outlined in red) is the laser itself, which produces ~ 10 ps laser pulses at a repetition rate of ~ 80 MHz. The second section (boxed in yellow) allows arbitrary pulses to be selected from the laser to be applied at the ion. The third section (green) takes each pulse and shapes it into two trains of 8 pulses each (2 ns duration) which are shifted in frequency by ~ 500 MHz relative to each other. The last section (blue) recombines these trains in space and time while maintaining their orthogonal polarization. A Pockels cell then selects which direction these beams are applied to the ion and determines the SDK direction.

a pulse duration of $\tau_p = 10$ ps, the energy and peak power of a single pulse is

$$E_p \approx \frac{24 \text{ W}}{80 \text{ MHz}} = 300 \text{ nJ} \quad (2.43)$$

$$P_p \approx 0.88 \frac{E_p}{\tau_p} = 26.4 \text{ kW}. \quad (2.44)$$

If all this power is focused to a $5 \mu\text{m}$ radius waist at the ion, it theoretically produces a total pulse area of [44]

$$\Theta \approx 60 \times 2\pi. \quad (2.45)$$

This is an upper limit, and only a fraction of the light is delivered to the ion after passing through the necessary optics.

Although a common concern when working with short laser pulses, dispersion is not a significant issue with 10 ps pulses. This can be understood by expanding the propagation constant $\beta(\omega)$ of the laser light to second order around the center frequency ω_0 [66]:

$$\beta(\omega) = \beta(\omega_0) + \beta'(\omega - \omega_0) + \frac{1}{2}\beta''(\omega - \omega_0)^2. \quad (2.46)$$

The second order term $\beta''(\omega) = \frac{d}{d\omega} \left(\frac{1}{v_g(\omega)} \right)$, in which $v_g(\omega)$ is the group velocity, is typically referred to as the group-velocity dispersion (GVD) and is about 100 fs^2/mm in fused silica at a laser wavelength of 400nm [67]. An initial pulse width of τ_{p0} will broaden to

$$\tau_p^2(z) = \left[1 + \left(\frac{z(4 \ln 2)\beta''}{\tau_{p0}^2} \right)^2 \right] \tau_{p0}^2, \quad (2.47)$$

and so even if the entire $z \sim 1$ m beam path was fused silica (in actuality it is mostly air, which has lower GVD [68]), a 10 ps pulse would broaden by a factor of only about $\sqrt{1 + 10^{-5}}$.

The laser was selected such that the repetition rate fell within specific ranges of frequencies to ensure high fidelity spin-dependent forces. As seen in Eq. 2.41, an integer multiple of the repetition rate plus the AOM shift must match the hyperfine splitting of the qubit. This is necessary if the laser is being used in the weak pulse regime for standard laser operations [32]. Additionally, the AOM shift must be larger than the width of a comb tooth for a given operation lest Raman transitions are driven with absorption and emission happening in both beams and reducing fidelity of the SDK. Finally, the AOM shift cannot be less than the width of a comb tooth away from half of the repetition rate (Eq. 2.41 again) or the force will not be spin dependent. In other words, there must be an asymmetry, and without this last condition, the ion will not preferentially absorb from one beam and emit into the other.

2.5.4 Picking and Rotating Pulses at 100 MHz

The timing and direction of an SDK is determined by the repetition rate of the laser pulses along with two Pockels cells and beam cubes, which rotate and analyze the polarization of arbitrary pulses in the train (Fig. 2.11). Each of these pulses will become eight smaller pulses to form an SDK, and a train of these eight pulses, or an SDK, is always rotated together). The upstream Pockels cell is used to pick which pulses make it to the ion. If the voltage that drives the Pockels cell is at zero volts, the vertical input polarization remains unchanged, and the cube directs the light into a beam dump. If the drive voltage is high, the input light is rotated

to have horizontal output orientation, and passes through the cube and down the table. The extinction ratio of this process (the ratio of average power of intentional light to unintentional light sent to the ion) is about 300:1.

The second Pockels cell is used to set the SDK direction. This method works by combining the linear-perpendicular-linear configured beams on a beam cube instead of at the ion-recall from Fig. 2.10 that two counter-propagating beams in a linear-perpendicular-linear fashion with a frequency difference ω_A have a preferential direction of emission and absorption at the ion which determines the kick direction. After combination, the beams are sent through the Pockels cell and beam splitter (Fig. 2.11). If the cell drive voltage is at zero, then nothing happens and the experiment occurs as it would without the cell. If the drive voltage is high, then the two beams are rotated, maintaining their relative orientation, and applied from opposite directions of the ion. This reversal of kick direction allows us to concatenate every pulse that is emitted from the laser as an SDK³.

In order to achieve proper timing between the pulse picker temporal window and arrival time of the pulses, we trigger the Pockels cell drive voltage sequence using a pulse from the laser. A pre-determined timing sequence is programmed into an arbitrary waveform-generator (AWG) which consists nominally of 0 V or 1 V (those voltages can be adjusted slightly to fine tune the driver) segments. This sequence is triggered when the experimental control program opens an rf switch and allows a pulse from the laser (converted to an electrical pulse on a photodiode)

³Without this switching, the ion would just be kicked back and forth without ever increase to a large momentum state because of the spin flip that occurs with each SDK.

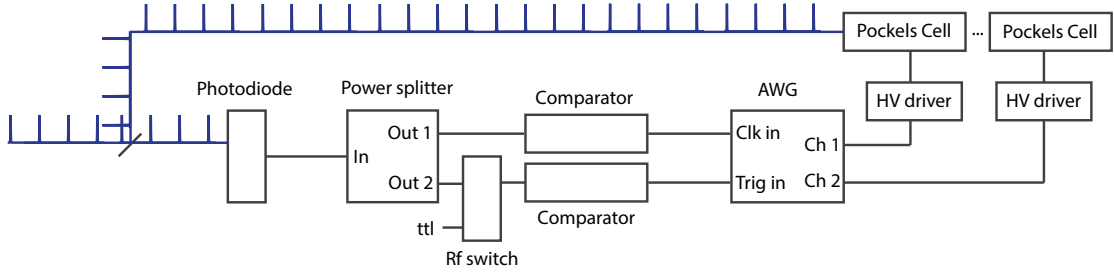


Figure 2.12: Triggering a pulse sequence. In order to ensure that the experimental control program is able to temporally match the pulses from the laser, we clock and trigger the Pockels cell drive voltage using laser pulses converted to electrical pulses.

to trigger the AWG sequence. The AWG, clocked by the same photodiode signal routed around the switch, runs the desired pulse sequence. This process is outlined in Fig. 2.12. It is important that the comparator (compares the input signal to an internal 50 mV and outputs 0 or 1 V depending on if the input is below or above the internal threshold) be after the rf switch, because the comparator fall time is much greater than the photodiode fall time; if the comparator were first, the rf switch would sometimes turn on during a comparator pulse making the timing random within that range and leading to varying optical pulse power when the pulse picker window does not align with the pulse.

Chapter 3: Stabilizing Ion Secular Motion

Charged particles are often controlled with radiofrequency (rf) electrical potentials, whose field gradients provide time-averaged (ponderomotive) forces that form the basis for applications such as quadrupole mass filters, ion mass spectrometers, and rf (Paul) ion traps [47, 51]. These rf potentials, typically hundreds or thousands of volts at frequencies ranging from 1kHz to 100 MHz, drive high impedance loads in vacuum and are usually generated with rf amplifiers and resonant step-up transformers such as quarter-wave or helical resonators [69]. Such circuitry is susceptible to fluctuations in amplifier gain, mechanical vibrations of the transformer, and temperature drifts in the system. Ion traps are particularly sensitive to these fluctuations, because the rf potential determines the harmonic oscillation frequency of the trapped ions. Stable trap frequencies are crucial in applications ranging from quantum information processing [36, 48] and quantum simulation [70, 71] to the preparation of quantum states of atomic motion [15], atom interferometry [33], and quantum-limited metrology [72].

Actively stabilizing rf ion trap potentials requires the faithful sampling of the rf potential. Probing the signal directly at the electrodes is difficult in a vacuum environment and can load the circuit or spoil the resonator quality factor. On the

other hand, sampling the potential too far upstream is not necessarily accurate, owing to changes in downstream inductance and capacitance. Here we actively stabilize the oscillation frequency of a trapped ion by noninvasively sampling and rectifying the high voltage rf potential between the step-up transformer and the vacuum feedthrough leading to the ion trap electrodes. We use this signal in a feedback loop to regulate the rf input amplitude to the circuit. We stabilize a 1 MHz trapped ion oscillation frequency to < 10 Hz for periods less than 200 s (slow drifts affect it on longer time scales), representing a maximum 34 dB reduction in the level of trap voltage (and therefore secular frequency) noise and drift at 200 s, with an adjustable locking bandwidth between 100 Hz and 30 kHz.

One approach to stabilize the ion oscillation frequency is to control the ratio V_0/Ω_{rf} , which is important in cases where the rf drive frequency is itself dithered to maintain resonance with the step-up transformer. This is necessary when the transformer resonance drifts, maybe due to mechanical or temperature fluctuations, by a significant amount of its linewidth. A feedback system of this style is shown in Fig. 3.1(a). One feedback loop (upper right section, blue) locks the rf drive frequency (tuned using frequency modulation–FM) to the step-up transformer resonance by deriving a zero crossing in the error signal from a phase shift across resonance of the reflected signal. This is done using a directional coupler to sample the drive and reflected signals and comparing the difference in phase using a frequency mixer. A second feedback loop (lower section, red) stabilizes the ratio V_0/Ω_{rf} using a digital divider. The main difficulty with this approach is the required performance of the digital divider circuit, which must have a precision as good as the desired stability,

and be fast enough to stabilize the system at the desired bandwidth. Moreover, higher order corrections to the trap frequency beyond the pseudopotential expression of Eq. 2.3 depend on terms that do not scale simply as the ratio V_0/Ω_{rf} . Therefore, we instead stabilize the rf potential amplitude V_0 alone, and use a fixed frequency rf oscillator and passively stable transformer circuit, as depicted in Fig. 3.1(b).

3.1 trap rf stabilization

We stabilize the rf confinement potential by sampling the high voltage rf signal supplying the ion trap electrodes and feeding it back to a frequency mixer that controls the upstream rf oscillator amplitude. As shown in the schematic of Fig. 3.1(b), an rf signal at $\Omega_{rf}/2\pi = 17$ MHz and -8 dBm is produced by an rf oscillator (SRS DS345) and sent through the local oscillator (LO) port of a level 3 frequency mixer (Mini-Circuits ZX05-1L-S), with a conversion loss of 5.6 dB. The RF port of the mixer is connected to a rf amplifier (Mini-Circuits TVA-R5-13) with a self-contained cooling system, providing a gain of 38 dB. The amplifier signal is fed into an antenna that inductively couples to a 17 MHz quarter-wave helical resonator and provides impedance matching between the rf source and the circuit formed by the resonator and ion trap electrode capacitance [69]. The antenna, resonator, and equivalent ion trap capacitance C_{trap} are shown in Fig. 3.2, and exhibit an unloaded quality factor $Q_U \sim 600$.

A capacitive divider samples roughly 1% of the helical resonator output, using

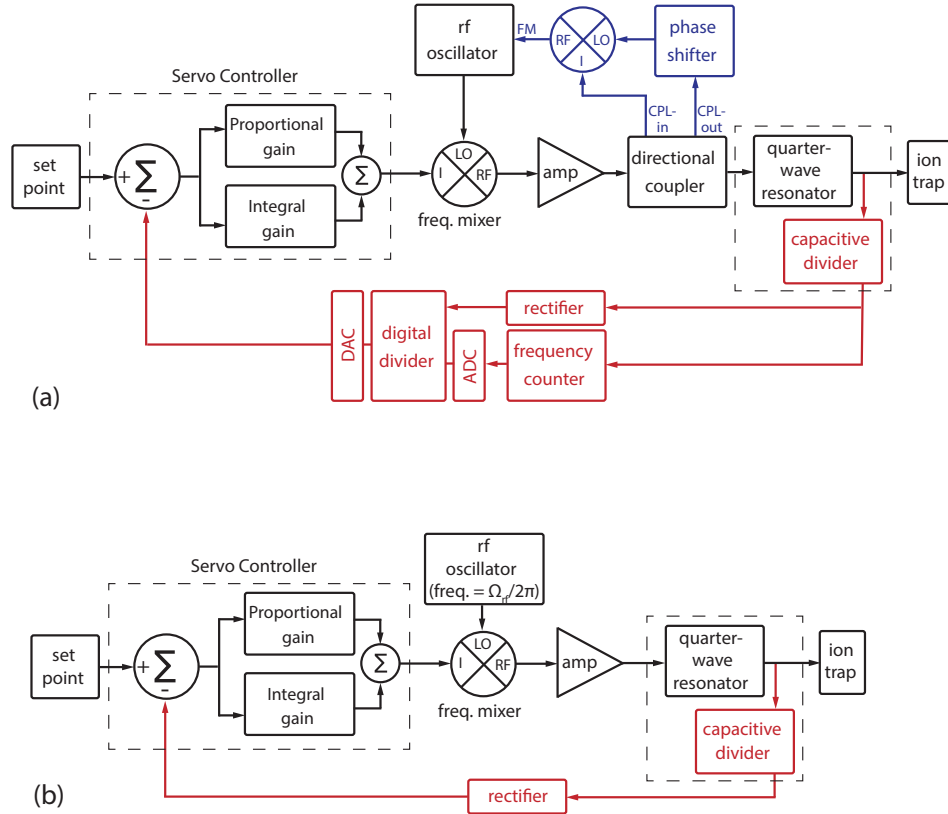


Figure 3.1: Ion trap rf drive with active stabilization [42]. (a) Stabilization of the ratio of rf potential amplitude to frequency V_0/Ω_{rf} (lower section, red) using a digital divider (ADC: analog-to-digital converter and DAC: digital-to-analog converter), with a separate feedback loop (upper right section, blue) that locks the rf drive frequency Ω_{rf} to the resonant frequency of the quarter-wave resonator (a step-up transformer). (b) Stabilization of the rf potential amplitude V_0 only, with fixed rf drive frequency (used in the experiment reported here).

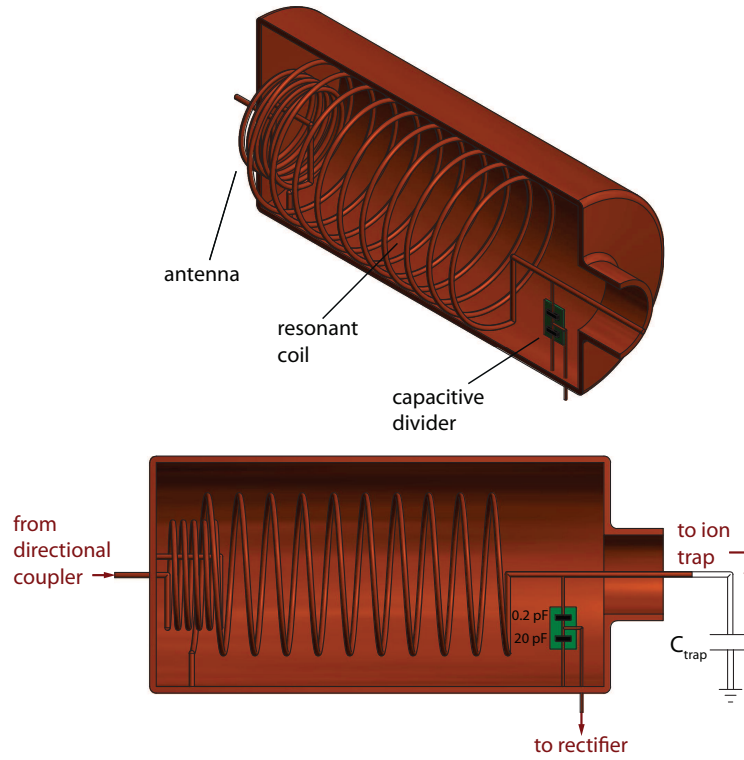


Figure 3.2: Helical quarter-wave resonator (transformer) with a 1:100 capacitive divider (0.2 pF and 20 pF) mounted inside of the resonator near the high voltage side [42]. The divider samples V_0 for feedback. A rigid wire is soldered from the output portion of the copper resonator coil to the copper-clad epoxy circuit board containing the dividing capacitors. The resonator drives the capacitance C_{trap} of the vacuum feedthrough and ion trap electrodes.

$C_1 = 0.2$ pF and $C_2 = 20$ pF ceramic capacitors (Vishay’s QUAD HIFREQ Series) with temperature coefficients of 0 ± 30 ppm/ $^{\circ}$ C. With $C_1 \ll C_{trap}$ and residual inductance between the divider and the trap electrodes much smaller than the resonator inductance itself, the divider faithfully samples the rf potential within a few centimeters of the trap electrodes and does not significantly load the trap/transformer circuit. The capacitors are surface-mounted to a milled copper-clad epoxy circuit board and installed inside the shielded resonator cavity, as diagrammed in Fig. 3.2.

The sampled signal passes through a rectifier circuit (Fig. 3.3(a)) consisting of two Schottky diodes (Avago HMPS-2822 MiniPak) configured for passive temperature compensation [73] and a low-pass filter giving a ripple amplitude 10 dB below the diode input signal amplitude. High quality foil resistors and ceramic capacitors are used to reduce the effect of temperature drifts. The entire rectifying circuit is mounted inside a brass housing (Crystek Corporation SMA-KIT-1.5MF) as shown in Fig. 3.3(b). The sampling circuit has a bandwidth of ~ 500 kHz, limited by the 5 k Ω /68 pF RC filter. The ratio of dc output voltage to rf input voltage peak amplitude, including the capacitive divider, is 1 : 250 at a drive frequency of 17 MHz, 1 : 330 at 100 MHz, and 1 : 870 at a drive frequency of 1 MHz (see section IV for additional details about drive frequency response).

The dc rectified signal is compared to a stable set-point voltage (Linear Technology LTC6655 5V reference mounted on a DC2095A-C evaluation board) with variable control (Analog Devices EVAL-AD5791 and ADSP-BF527 interface board), giving 20-bit set-point precision and ± 0.25 ppm stability. The difference between these inputs – the error signal – is then amplified with proportional and integral

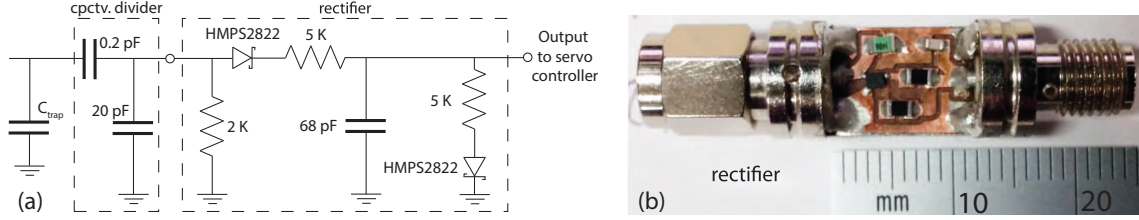


Figure 3.3: Rectifier circuit diagram and photograph [42]. (a) Schematic circuit diagram depicting the components of the pick-off voltage divider and temperature-compensating rectifier. (b) Photograph of the connected housing and mounted rectifier circuit.

gain (New Focus LB1005 servo controller) and fed back to regulate the upstream rf oscillator amplitude via the frequency mixer described above. Figure 3.4 shows the response of the system for various servo controller bandwidth settings when signals over a range of frequencies with constant amplitude are injected into the system at the amplifier input. The overall frequency response of the feedback loop is limited to a bandwidth of 30 kHz, consistent with the linewidth $\Omega_{rf}/(2\pi Q_U)$ of the helical resonator transformer.

3.2 Ion Oscillation Frequency

We next characterize the rf amplitude stabilization system by directly measuring the transverse motional oscillation frequency of a single atomic $^{171}\text{Yb}^+$ ion confined in the rf trap. We perform optical Raman sideband spectroscopy [15] between the same $|F = 0, m_f = 0\rangle \equiv |\downarrow\rangle$ and $|F = 1, m_f = 0\rangle \equiv |\uparrow\rangle$ “clock” hyperfine levels of the $^2S_{1/2}$ electronic ground state discussed in the last chapter. Recall, this atomic transition has a frequency splitting of $\omega_{hf}/2\pi = 12.642815$ GHz and acquires

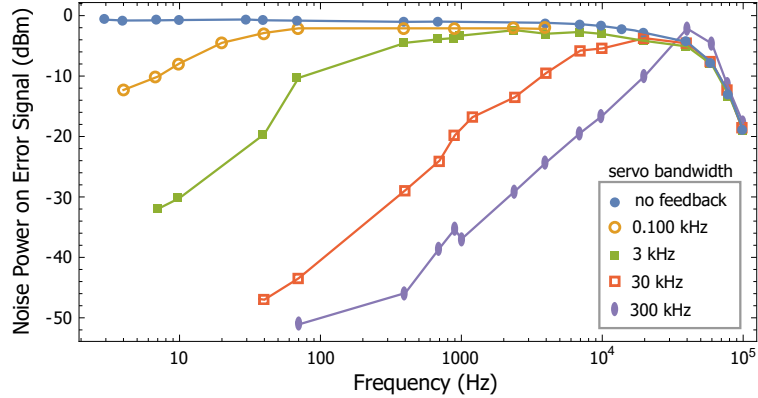


Figure 3.4: Suppression of injected noise in the stabilization circuit for various levels of feedback [42]. The rf drive is weakly amplitude-modulated at frequencies swept from 4 Hz to 100 kHz via a variable attenuator inserted before the rf amplifier (labeled "amp" in Fig. 3.1). The amplitude of the resulting ripple on the error signal (set point minus feedback at servo controller input) is measured for several servo controller bandwidth settings. The observed overall loop bandwidth of ~ 30 kHz is consistent with the linewidth of the helical resonator transformer.

frequency-modulated sidebands at $\omega_{hf} \pm \omega$ due to the harmonic motion of the ion in the trap, with $\omega/2\pi \sim 1$ MHz. Before each measurement, the ion is Doppler cooled. The ion is next prepared in the $|\downarrow\rangle$ state through optical pumping, and following the sideband spectroscopy described below, the state ($|\downarrow\rangle$ or $|\uparrow\rangle$) is measured with state-dependent fluorescence techniques [56].

The oscillation frequency is determined by performing Ramsey spectroscopy [74] on the upper (blue) vibrational sideband of the clock transition at frequency $\omega_{hf} + \omega$. Because the atomic clock frequency ω_{hf} is stable and accurate down to a level better than 1 Hz, drifts and noise on the sideband frequency are dominated by the oscillation frequency ω . The sideband is driven by a stimulated Raman process from two counter-propagating laser light fields with a beatnote ω_L tuned

near the upper vibrational sideband frequency [32, 65]. Following the usual Ramsey interferometric procedure [74], two $\pi/2$ pulses separated by time $\tau = 0.4$ ms drive the Raman transition. After the pulses are applied, the probability of finding the ion in the $|\uparrow\rangle$ state $P(\delta) = (1 + C \cos \tau\delta)/2$ is sampled, where $\delta = \omega_L - (\omega_{hf} + \omega)$ is the detuning of the beatnote from the sideband and C is the contrast of the Ramsey fringes. The Ramsey experiment is repeated 150 times for each value of δ in order to observe the Ramsey fringe pattern $P(\delta)$ and track the value of ω . Because this Raman transition involves a change in the motional quantum state of the ion, the Ramsey fringe contrast depends on the purity and coherence of atomic motion. For short Ramsey times, the measured contrast of ~ 0.8 is limited by the initial thermal distribution of motional quantum states, and for Ramsey times $\tau > 0.5$ ms, the fringe contrast degrades further (Fig. 3.5), which is consistent with a decoherence timescale $(2\bar{n}_0\dot{\bar{n}})^{-1}$ for initial thermal state $\bar{n}_0 = 15$ quanta and motional heating rate $\dot{\bar{n}} = 100$ quanta/s [75].

Through Ramsey spectroscopy, we sample the ion trap oscillation frequency ω at a rate of 2.1 Hz for 80 minutes with no feedback on the rf potential, and then for another 80 minutes while actively stabilizing the rf potential. A typical time record of the the measurements over these 160 minutes is shown in Fig. 3.6. Feedback control clearly improves the stability of the ion oscillation frequency.

From these measurements, we plot the Allan deviation [76] of the oscillation frequency in Fig. 3.7 as a function of integration time T . When the system is stabilized, the Allan deviation in ω is nearly shot-noise limited (decreasing as $1/\sqrt{T}$) up to ~ 200 s of integration time, with a minimum uncertainty of better than 10

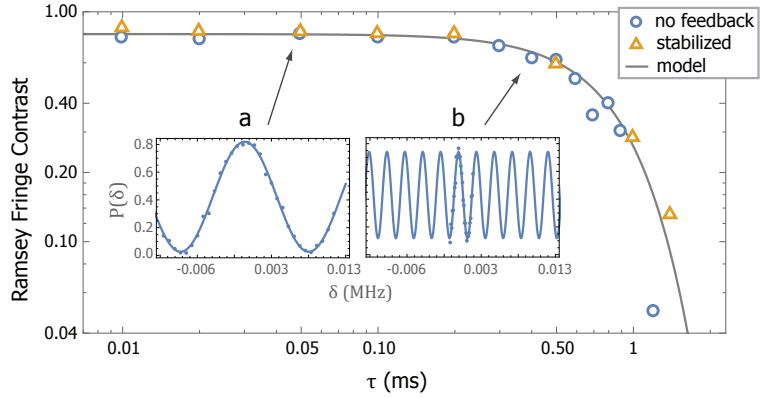


Figure 3.5: Ramsey fringe contrast as a function of the Ramsey time τ between $\pi/2$ pulses, with and without feedback [42]. The gray line is a model in which motional heating causes Ramsey fringe decoherence in ~ 0.5 ms. Inlays a and b show full Ramsey fringe measurements and fits for two different values of τ .

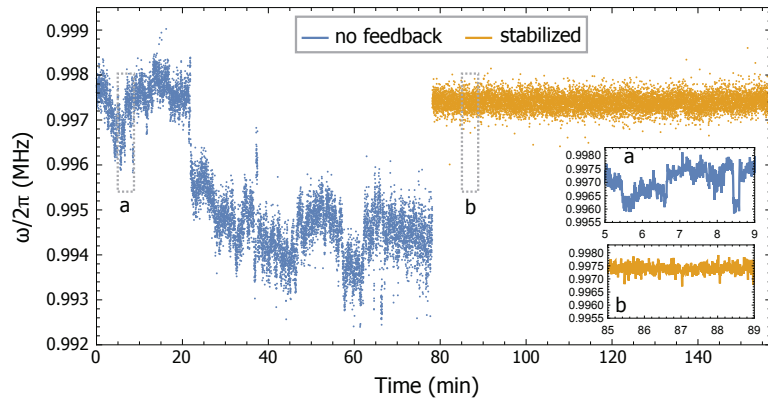


Figure 3.6: Time dependence of the ion harmonic oscillation frequency ω plotted over the course of 160 minutes with and without active stabilization [42]. With feedback there is a clear reduction in noise and drifts (apart from measurement shot noise, reflected by the fast fluctuations in the data). Inlays a and b show magnified sections of the plot covering 4 minutes of integration.

Hz, or 10 ppm, representing a 34 dB suppression of ambient noise and drifts in the drive voltage or secular frequency. Without feedback, the trap frequency deviation drifts upward with integration time. For integration times shorter than 7 s, there is not sufficient signal/noise in the measurements to see the effects of feedback stabilization. However, as shown in Fig. 3.4, the lock is able to respond to error signals up to a bandwidth of ~ 30 kHz, and we expect significant suppression of noise at these higher frequencies as well. Although the Allan deviation of the oscillation frequency in the stabilized system improves with longer averaging time as expected, it drifts upward for a period just after $T = 50$ s (likely caused by a temperature drift affecting the capacitive divider pick-off). We confirm this drift appears in the ion oscillation frequency ω and not the driving field ω_L or the ion hyperfine splitting ω_{hf} by performing the same experiment on the clock “carrier” transition near beatnote frequency $\omega_L = \omega_{hf}$ instead of the upper sideband $\omega_L = \omega_{hf} + \omega$. As shown in Fig. 3.7, the measured Allan deviation of the carrier continues downward beyond $T = 50$ s, meaning that the ion oscillation frequency is indeed the limiting factor at long times.

3.3 Limits and noise sources

It should be possible to stabilize the rf trap frequency much better than the observed 10 ppm by improving passive drifts outside of feedback control. These include the capacitive divider that samples the rf, the rectifier, the stable voltage reference, rf source frequency, and certain cables in the rf circuitry. Most of these

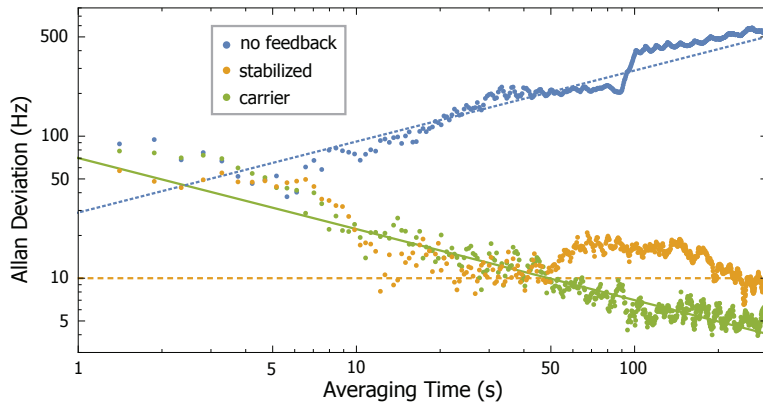


Figure 3.7: Allan deviation data of the secular frequency ω while the system is with and without feedback, as well as the Allan deviation of the qubit carrier transition [42]. The Allan deviation curves are calculated from the time record shown in Fig. 3.6, along with a similar measurement performed on the carrier transition.

components will have residual drifts with temperature, mechanical strains, or other uncontrolled noise. Below is a table of all crucial components outside of feedback control and their estimated contribution to the instability.

Table 3.1: Estimated stability of components outside of feedback control.

| Component | Stability |
|--------------------|----------------|
| Capacitive Divider | $0 \leq 6$ ppm |
| Rectifier | 0.01 ppm |
| Voltage Reference | 0.25 ppm |
| rf source freq. | 0.1 ppb |
| Cables | Unknown |

The capacitive divider pick-off is comprised of two capacitors each with a temperature coefficient of ± 30 ppm/ $^{\circ}\text{C}$. Given the voltage divider configuration, the net temperature coefficient can range from $\sim 0 - 60$ ppm/ $^{\circ}\text{C}$ depending on how well the capacitors are matched. Because temperature drifts on the order of $\sim 0.1^{\circ}\text{C}$

are expected without active temperature stabilization, the capacitive divider is likely limiting the ultimate stability of the system. Instabilities in the rectifier can arise from variability in the junction resistance of the diodes. In series with a 5 k Ω resistor, the $\sim 0.01\Omega/^\circ\text{C}$ junction resistance gives a net temperature coefficient of about 0.2 ppm/ $^\circ\text{C}$ in the rectifier response. This is roughly equal to the temperature coefficient of the resistors used in the rectifier circuit. By using the circuit configured for passive temperature compensation [73] shown in Fig. 3.3, we estimate the net temperature coefficient of the rectifier response is reduced to ~ 0.1 ppm/ $^\circ\text{C}$.

Performance of the circuit is also helped by passively stabilizing components within the feedback loop as much as possible, such as temperature regulating the rf amplifier which feeds the resonator and using a passive mixer instead of a powered voltage variable attenuator. The helical transformer is particularly sensitive to temperature fluctuations and mechanical vibrations, which alters the resonance frequency and quality factor. (Ensuring the helical coil is sealed against air currents can be more important than correcting small drifts in ambient temperature.) If the resonant frequency of the transformer drifts too far, then a feedback circuit with a fixed frequency source (as used here and shown in Fig. 3.1(b)) will call for more input power, and the servo system could possibly run away and become unstable. However, the resulting impedance mismatch from the off-resonant coupling will cause the servo to maintain the same amount of dissipated power in the resonator [69] and not necessarily affect further drifts. In any case, we do not observe such servo runaway. This is true even when the set point is ramped down and back up to cycle the trap rf voltage during instances in which ions are too hot for effec-

tive laser cooling in the tighter trapping potential. The resulting transient thermal response has no apparent effect on the secular frequency stability.

Based on simulations, this system is capable of stabilizing the rf amplitude in ion trapping apparatuses using a range of rf drive frequencies. Figure 3.8 shows the transient turn-on and steady state responses of the rectifier output for drive frequencies ranging from 1 MHz to 150 MHz. We see that while 17 MHz gives near maximum direct current (DC) voltage (a higher DC voltage is like a higher gain), increasing or decreasing the drive frequency by up to an order of magnitude still provides an appreciable DC voltage (the optimum frequency can also be shifted by modifying the rectifier circuit). So long as the rectifier output offset voltage (ripple is filtered by the servo controller) is appreciable, the feedback loop will maintain performance near the demonstrated fractional secular frequency stability of better than 10 ppm, independent of ion mass (see Eq. 2.3).

If the temperature coefficients of the capacitors in the capacitive divider are properly matched and the divider is actively temperature-stabilized, we believe the technique presented in this article would provide a stability in radial secular frequency of ~ 0.3 ppm. This stability could likely be made even better by further stabilization of the voltage reference in addition to improved design of the whole apparatus including mechanical and thermal stabilization, improved electrical shielding, and shortened distances between components.

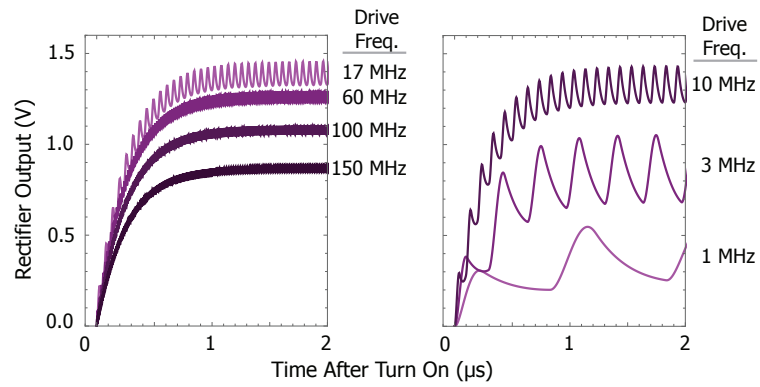


Figure 3.8: Simulations of the transient voltage output (into a $1\text{M}\Omega$ load) of the rectifier circuit with a 700 Vpp rf trap drive turned on at $t = 0\text{ s}$ [42]. The plots shows a response time, ripple, and dc offset at steady state for a range of drive frequencies.

Chapter 4: Sensing Atomic Motion

Ultrafast sensing of atomic motion works over a wide range of energies, from the zero-point (phonon occupation number $n = 0$) to potentially above room-temperature ($\bar{n} \sim 10^6$ for typical ion traps). Ultrafast partial state tomography (defined later in this chapter) on thermal states improves upon the dynamic range achieved with thermometry using dark resonances [77]. It also complements conventional methods of thermometry, including measurements of the motionally-induced upper and lower sideband asymmetries [78] and the thermal effects on induced transitions (Debye-Waller factors) [79]. However, both of these other methods break down when the atomic motion is outside of the Lamb-Dicke regime, typically around $\bar{n} > 10$. Measuring the entire Doppler-broadened envelope of sidebands [80] provides a more general measurement of thermal states, but can be difficult due to the bandwidth required to excite multiple sidebands. In this chapter, we use ultrafast techniques for accurate thermometry of ion motion ranging from $\bar{n} \sim 0.1$ to $\bar{n} \sim 10^4$ and show how this method extends to higher energies. We also measure particular quantum states through more complete motional tomography.

4.1 Experimental Description

In this experiment, we again trap a $^{171}\text{Yb}^+$ ion in a linear radio frequency Paul trap and probe the motion along a single radial mode of motion with secular trap frequency $\omega/2\pi \approx 1$ MHz. The $|F = 0, m_f = 0\rangle \equiv |\downarrow\rangle$ and $|F = 1, m_f = 0\rangle \equiv |\uparrow\rangle$ hyperfine levels of the $^2S_{1/2}$ electronic ground state are again used as the qubit, or effective spin. The ion is laser-cooled to near the Doppler limit ($\bar{n} \approx 10$) and optically pumped during initial state preparation. Qubit state detection is performed by collecting state-dependent fluorescence [56]. The qubit state in these experiments is detected with a fidelity above 0.997 using an imaging objective with 0.6 numerical aperture and a photomultiplier tube [62].

We create a spin-dependent kick (SDK) using the method discussed in the previous section—by modifying individual pulses extracted from a mode-locked laser with center wavelength $2\pi/k \approx 355$ nm, pulse duration $\tau \sim 10$ ps, and repetition rate of $f_{rep} = 118$ MHz (note that this is a higher repetition rate laser than discussed in Chapter 2). Each SDK has a spin population transfer from $|\downarrow\rangle$ to $|\uparrow\rangle$ with measured fidelity of 0.993(2) [32]. Because each SDK operation provides a momentum kick and flips the spin, immediately applying a second SDK would simply undo the first. However, by waiting one half of the trap period between SDKs, we can concatenate N individual kicks to create a larger effective SDK with $\Delta p = \pm 2N\hbar k = \pm N\eta p_0$. ($p_0 = \sqrt{\hbar m \omega/2}$ is the momentum spread of the ground state, and m is the ion mass.)

Techniques using Ramsey spectroscopy on states coherently displaced by spin

dependent forces have been demonstrated in creating Schrödinger cat states [28] and measuring spin dephasing in 2D ion crystals [81]. In this experiment, we create an interferometer to sense motion by applying two sets of N SDK operations within a Ramsey experiment on the qubit levels with time duration T (time separation of microwave $\pi/2$ pulses). First the ion is prepared in a coherent superposition of $|\downarrow\rangle$ and $|\uparrow\rangle$ by applying a near-resonant microwave $\pi/2$ pulse of duration τ_μ . A set of N SDKs is applied, and following this first set, the ion evolves for a time θ/ω_t before a second set of N SDKs is applied. After a time T from the first microwave $\pi/2$ pulse, another microwave $\pi/2$ pulse with the same duration and tuning drives the qubit to close the Ramsey interferometer. This sequence is diagrammed in Fig. 4.1(a). By scanning the microwave detuning $\delta \ll 1/\tau_\mu$ from resonance, we observe sets of Ramsey fringes with phase $\phi = \delta T$ that chronicle the ion motion (shown in Fig. 4.1(b) and 4.1(c)).

For a pure initial state $|\Psi^\alpha\rangle_i = |\downarrow\rangle |\alpha\rangle$, where α is a coherent state of the ion motion, the state following the Ramsey experiment is [44]

$$\begin{aligned}
|\Psi^\alpha\rangle = \frac{1}{2} & \left[e^{i\gamma} (|\downarrow\rangle + ie^{-i\phi} |\uparrow\rangle) |(\alpha + iN\eta)e^{-i\theta} - iN\eta\rangle \right. \\
& \left. + ie^{-i\gamma} (|\uparrow\rangle + ie^{i\phi} |\downarrow\rangle) |(\alpha - iN\eta)e^{-i\theta} + iN\eta\rangle \right], \tag{4.1}
\end{aligned}$$

where $\gamma = N\eta[\text{Re}(\alpha)(1 - \cos \theta) - \text{Im}(\alpha) \sin \theta]$.

Given an arbitrary initial state of motion in phase space described by the Glauber P-distribution [82,83], the final density matrix is $\hat{\rho} = \int P(\alpha) |\Psi^\alpha\rangle \langle\Psi^\alpha| d^2\alpha$. The probability of measuring the state spin-up after the Ramsey experiment is

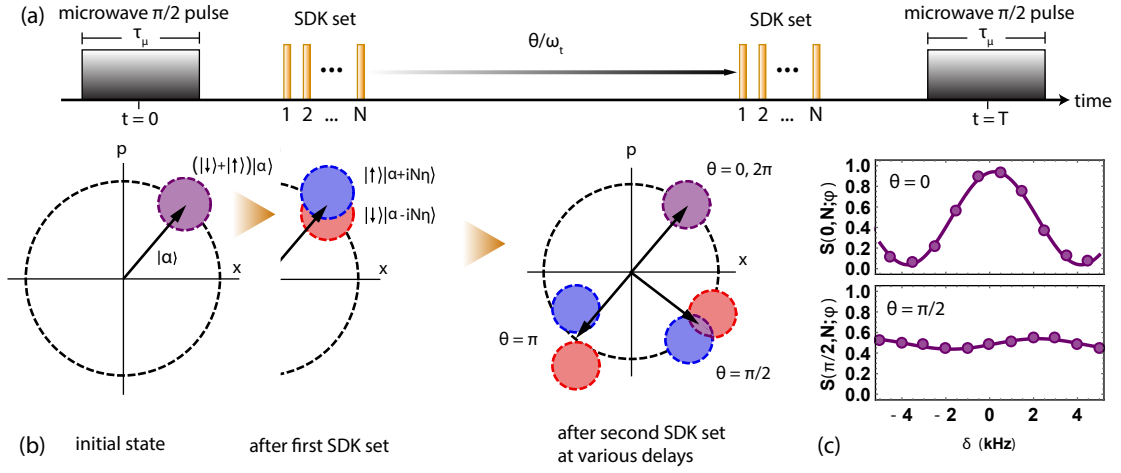


Figure 4.1: Ultrafast atom interferometry [33]. (a) Timeline of a single experiment, where a full SDK set is made of N single SDKs. (b) Phase space diagram of an initial state $(|\downarrow\rangle + |\uparrow\rangle)|\alpha\rangle$ evolving under two sets of SDKs separated by time delay θ/ω_t , where $|\alpha\rangle$ is a coherent state of motion. (c) Typical Ramsey fringes as a function of microwave frequency detuning δ . These two plots correspond to the points $\theta = 0$ and $\theta = \pi/2$ of an initial thermal state ($N = 1$ for the data shown). The function $S(\theta, N; \phi)$ is described by Eq. 4.2.

therefore

$$S(\theta, N; \phi) = \langle \uparrow | \hat{\rho} | \uparrow \rangle = \frac{1}{2} + \frac{1}{2} \int P(\alpha) e^{-4(N\eta)^2(1-\cos\theta)} \cos(4\gamma - \phi) d^2\alpha. \quad (4.2)$$

Two types of motional state that are readily accessible in the laboratory are thermal states and small Fock states. First we discuss ultrafast partial state tomography to determine the average phonon number in a thermal state. Then we extend this method to create a nearly complete map of the motion of an $n = 1$ Fock state in phase space, showing clear nonclassical signatures.

4.2 Thermometry

For an ion prepared in a thermal state with mean phonon number \bar{n} and P-function $P_{therm}(\alpha) = \frac{1}{\pi\bar{n}} e^{-|\alpha|^2/\bar{n}}$, Eq. 4.2 yields an expected Ramsey fringe pattern

$$S_{therm}(\theta, N; \phi) = \frac{1}{2} + \frac{1}{2} e^{-4(N\eta)^2(2\bar{n}+1)(1-\cos\theta)} \cos\phi. \quad (4.3)$$

The fringe contrast has periodic revival peaks at $\theta = 2\pi m$, where m is a positive integer. For a hot ion where $\bar{n} \gg 1/(N\eta)^2$, these revivals in contrast become narrow and approximately Gaussian with full width at half maximum FWHM = $0.83/(N\eta\sqrt{\bar{n}})$. With $N = 1$, we measure the Ramsey fringe contrast as a function of θ for a variety of initial thermal states of motion, and fit the contrast revival peaks to Eq. 3 to determine the average phonon number \bar{n} of the thermal state [75, 84, 85]. In the fit, we allow the peak Ramsey contrast at $\theta = 2\pi m$ to be less than unity in order to parametrize imperfect fidelity of the SDK operations. This reduction in fidelity is mainly attributed to variations in the Raman beam intensity over the

spatial extent of the ion wave packet (beam waist is $\approx 2 \mu\text{m}$), and becomes apparent at high \bar{n} ($\bar{n} = 10000$ has a spread of $\approx 1 \mu\text{m}$). This does not affect the width (it does affect the height) of the contrast revival peak, and thus the accuracy of the thermometer, and can be mended by widening the beam waist.

Ramsey contrast revival lineshapes are measured in experiments spanning over five orders of magnitude in \bar{n} , as shown in Figs. 4.2(a)-(c). Figure 4.2(d) shows these measurements plotted versus the expected value of \bar{n} from theory and other measurements. The figure is broken into three regions according to the manner in which the motional state is prepared and calibrated before measurement of the contrast revival lineshapes. Low energy thermal states ($\bar{n} < 10$) are generated by first sideband-cooling the ion to its zero point motion and then allowing the ion to weakly heat (the trap has a natural heating rate of 310(10) quanta/s due to trap electrode noise and anomalous heating [86]) in the trap by known amounts. In this regime, we compare ultrafast interferometric measurements of \bar{n} (shown in Fig. 4.2(b)) to values extracted from measured sideband asymmetries [55]. The deviation of the two measurements are shown in the red section of Fig. 4.2(a).

For thermal states $10 < \bar{n} < 150$, the ion is prepared by Doppler cooling with various frequency detunings from resonance. Ultrafast measurements in this regime are shown in Fig. 4.2(d). Each of these measurements and the predicted value of \bar{n} from Doppler cooling theory [87] (Fig. 4.2(e)) are plotted against each other in the green section of Fig. 4.2(a). As a check on the expected values of \bar{n} in this range, we also measure the Debye-Waller suppression of Rabi flopping amplitude transitions between the ion qubit states [55] for several cases, resulting in expected

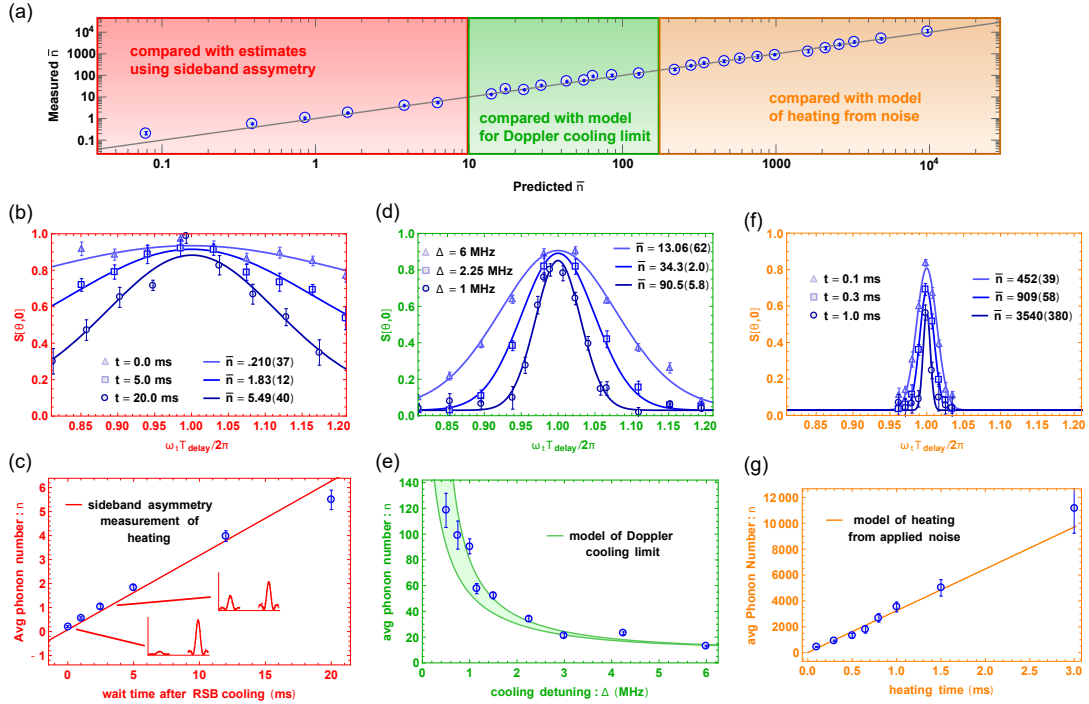


Figure 4.2: Ultrafast sensing measurements of \bar{n} (with $N = 1$) [33]: (a) Measurements of \bar{n} versus predicted values. There are three regimes of thermal state preparation—red being sideband-cooling then heating (see (b)), green being Doppler cooling with different detunings (see (d)) and orange being heating with applied noise (see (f)). (b) Sampling of Ramsey revival contrast lineshapes with initial states prepared by resolved sideband cooling to the ground state and subsequent heating. Data is fit to $S_{therm}(\theta, 1; \phi)$. The amplitude of each fit is a free parameter to account for SDK infidelity (also done in (d) and (f)). This does not significantly affect the width of the peak, which is used to determine \bar{n} . (c) Using identical state preparation to (b) but then a conventional sideband asymmetry measurement to determine ion temperature, a heating rate is determined and used to model the phonon number for wait times (solid line). The thermometry measurements from (b) are plotted to compare. (d) Sampling of Ramsey revival contrast lineshapes with initial states prepared by Doppler cooling only, with \bar{n} varied by changing the cooling beam detuning. (e) A model for average phonon occupation when preparing each state with various Doppler cooling beam detunings—the Doppler limit is a function of detuning (solid lines). Data from (d) is compared to the model. (f) Sampling of Ramsey revival contrast lineshapes with initial states prepared by inducing a high heating rate with white noise applied to a trap electrode. (g) A model for the phonon occupation after applying electrode noise is shown (solid line). Data from fits like that of (f) are plotted for comparison.

values consistent with Doppler theory.

Hot thermal states are prepared by inducing a high heating rate with a noisy electrical potential to a trap electrode for varied amounts of time after Doppler cooling. The ultrafast measurements of these states are shown in Fig. 4.2(f). Measurements in this regime are compared to a predicted \bar{n} given by the equation $\dot{\bar{n}} = \frac{e^2 S_V(\omega_t)}{4M\hbar\omega_t d^2}$ [78], where e is the ion charge, and $S_V(\omega_t)$ (V^2/Hz) is the applied power noise spectral density of the electric-potential, which is white over the measurement bandwidth (Fig. 4.2(g)). The effective distance d of the electrode to the ion is calibrated by applying a static potential offset to the same electrode and observing the resulting displacement of the ion in space [88]. The predicted and measured values for this regime are plotted against each other in the orange region of Fig. 4.2(a).

4.3 Fock State Tomography

We next perform more complete tomography of a nearly pure quantum state of motion by extracting the characteristic function

$$\chi_W(\alpha) = e^{-|\alpha|^2/2} \int P(\beta) e^{2i\text{Im}(\alpha\beta^*)} d^2\beta, \quad (4.4)$$

where $P(\beta)$ is again the Glauber P-distribution (integrated over the complex plane). This quasiprobability distribution contains all the information about the quantum state and is the Fourier transform of the better-known Wigner distribution [89, 90].

In terms of the observable $S(\theta, N; \phi)$, $\chi_W(\alpha)$ is given by

$$\text{Re}[\chi_W(\alpha)] = 2S(\theta, N; 0) - 1 \quad (4.5)$$

$$\text{Im}[\chi_W(\alpha)] = 2S(\theta, N; \frac{\pi}{2}) - 1, \quad (4.6)$$

where $\alpha = 2N\eta[\sin\theta + i(1 - \cos\theta)]$. Scanning θ and N while measuring $S(\theta, N; \phi)$ maps the characteristic function over rings in phase space, shown in Fig. 4.3(a). In order to scan the negative imaginary part of α , we can change the direction of the initial momentum kick associated with the spin flip operators by shifting the relative optical phase of the counter-propagating beams by π [1]. These reversed kicks can be thought of as effectively flipping the sign of η , and for simplicity, we represent them here by negative values of N .

We measure the characteristic function $\chi_W(\alpha)$ of the ion in the $n=1$ Fock state, prepared by sideband cooling to the ground state and transferring population to the $n=1$ state through application of a blue sideband operation [15]. To have a grid that spans the domain of the state, we scan around 16 rings in phase space set by $\pm N$, where $N = 1, 2, 3, 4, 5, 6, 8, 10$. Two of the 16 rings along which we measure are highlighted in Fig. 4.3(a), and plots of $S(\theta, N; 0)$ versus θ along those two rings are shown in Fig. 4.3(b). Notice in Fig. 4.3(b) that the larger SDK set ($N = 5$) separates the interferometer enough to see the oscillation of the motional distribution, while the smaller SDK set does not. Mapping along all 16 curves gives a nearly complete motional state map. The real part of the characteristic function is shown in Fig. 4.3(c) alongside the corresponding model of $\text{Re}[\chi_W(\alpha)]$ for an $n = 1$ Fock state in Fig. 4.3(d). The negative values of the characteristic quasiprobability

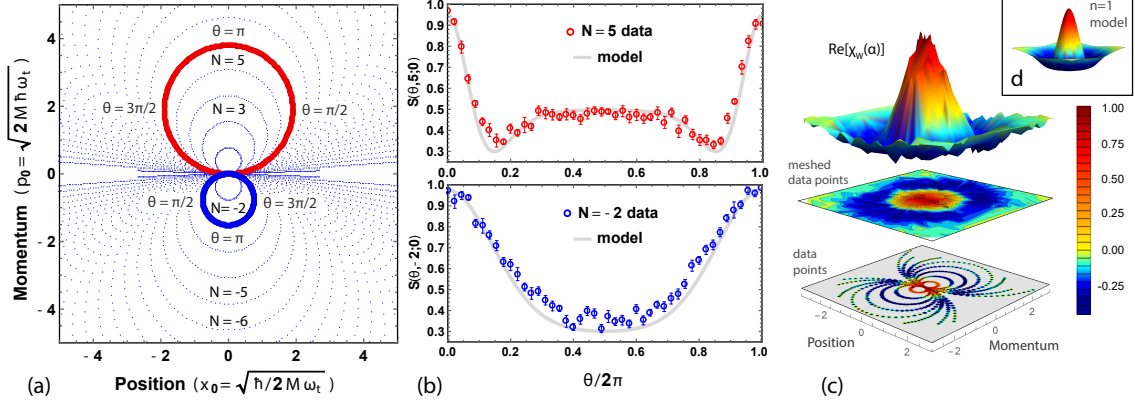


Figure 4.3: Ultrafast phase space tomography [33] (a) Points in phase space accessible in our tomographic measurements. The radius of each circle ($2N\eta$) is set by the number of kicks N , and the angular position on each circle is set by the SDK delay θ . The sign of N represents the direction of the initial momentum kicks associated with the spin flip operators. (b) Sample of measurements of the Ramsey fringe at $\phi = 0$ for a nominal $n = 1$ Fock state, using two sets of kicks with $N = 5$ (red) and $N = -2$ (blue) and scanning the delay θ . [The coordinates of these particular scans in phase space are highlighted in (a)]. (c) Motional state tomography of an ion prepared in the $n = 1$ Fock state. In ascending order: the value-colored data points of $\text{Re}[\chi_W(\alpha)]$ taken on 16 rings in phase space set by $\pm N$ where $N = 1, 2, 3, 4, 5, 6, 8, 10$, the interpolated data mapped in contour, and a 3D interpolation of the data. (d) Theory prediction for a Fock state with $n = 1$.

function highlight the nonclassical nature of the motional state of the ion.

4.4 Limits of Measurement

These ultrafast tomographic techniques are capable of measuring motional energies far beyond the data presented here, which was limited to $\bar{n} \sim 10^4$ because of re-cooling issues during state preparation (it becomes difficult to cool the ion in a reasonable amount of time to start a new experiment after it has been heated to a very high temperature). In the experiment, we scan the motional interferometric angular delay θ in steps set by the repetition rate of the laser, giving a resolution of $\omega_t/f_{rep} \sim 50$ mrad. For revival lineshapes narrower than this laser repetition rate limit, we scan θ by changing the trap frequency ω_t through accurate control of the trap rf drive voltage. With fine drive-voltage control, we can achieve a resolution in θ of 0.1 mrad, which would correspond to a contrast revival linewidth from a thermal state with $\bar{n} \sim 10^9$ (that is also about where trap anharmonicity may start to play a role). Other factors also come into play when measuring such high-energy states: First, the spatial extent of motion swells beyond the laser beam waist. At $\bar{n} = 10^6$ for instance, or equivalent temperature $T = \hbar\omega_t\bar{n}/k_B = 80\text{K}$, the ion would experience a significant gradient in the Rabi frequency across a beam with a $3\mu\text{m}$ waist. A second factor is the decreased detection fluorescence due to larger Doppler shifts at these energies. The detection fluorescence at $\bar{n} = 10^6$ would be reduced by a factor of $\sim 10^3$ from a cold ion [87]. Finally, when measuring these very narrow lineshapes, instabilities in the trap frequency ω_t and laser repetition rate f_{rep} would

have to be sufficiently stable over the measurement time. At $\bar{n} = 10^6$, this would require a fractional stability from both the trap frequency and laser repetition rate of better than 0.1%. These factors put ultrafast interferometric measurements of $\bar{n} \geq 10^6$ neither fundamentally nor technically beyond reach.

Chapter 5: Ultrafast Schrödinger Cat States

Mesoscopic quantum superpositions, or “Schrödinger cat states,” are widely studied for fundamental investigations of quantum measurement and decoherence [91] as well as potential applications in sensing [92] and quantum information science [93]. The generation and maintenance of such states relies upon a balance between efficient external coherent control of the system and sufficient isolation from the environment. Here we create a variety of cat states of a single trapped atom’s motion in a harmonic oscillator using ultrafast laser pulses. These pulses produce high fidelity impulsive forces that separate the atom into widely-separated positions, without restrictions that typically limit the speed of the interaction or the size and complexity of the resulting motional superposition. This allows us to quickly generate and measure cat states larger than previously achieved in a harmonic oscillator, and create complex multi-component cat state superpositions in atoms.

Quantum superposition is the primary conceptual departure of quantum mechanics from classical physics, giving rise to fundamentally probabilistic measurements, nonlocal correlations in spacetime [94], and the ability to process information in ways that are impossible using classical means [93]. Quantum superposi-

tions of widely separated but localized states, sometimes called “Schrödinger cat states” [95], exacerbate the quantum/classical divide. These states can be created in systems such as cold atoms and ions [28, 96, 97], microwave cavity QED with Rydberg atoms [98] and superconducting circuits [99–101], nanomechanical oscillators [9], and van der Waals clusters and biomolecules [102, 103]. All these systems gain sensitivity to outside influences with larger separations.

The natural localized quantum state of a harmonic oscillator is the coherent state $|\alpha\rangle$ [82], which is a Poissonian distribution of oscillator quanta with mean $|\alpha|^2$. For a mechanical oscillator with mass m and frequency ω , the complex number α characterizes the position \hat{x} and momentum \hat{p} operators of the oscillator, with $Re[\alpha] = \langle\hat{x}\rangle/(2x_0)$ and $Im[\alpha] = \langle\hat{p}\rangle x_0/\hbar$, where $x_0 = \sqrt{\hbar/(2m\omega)}$ is the zero-point width. Schrödinger Cat superpositions of coherent states $|\alpha_1\rangle + |\alpha_2\rangle$ of size $\Delta\alpha = |\alpha_1 - \alpha_2| \gg 1$ have been created in the harmonic motion of massive particles (phonons) [18] and in single mode electromagnetic fields (photons) [45]. In trapped ion systems, coherent states of motional oscillations are split using a qubit derived from internal electronic energy states [28, 104]. For photonic cat states, coherent states in a single mode microwave cavity are split using atoms or superconducting Josephson junctions. Recent experiments have created cat states with more than two components [105] for qubit storage and error protection [101]. In superconducting cavities, the size of the cat state is restricted to a maximum photon number of $\Delta\alpha^2 \sim 100$, due to nonlinearity of the self-Kerr and dispersive shift [101]. For trapped ions, cat states have been restricted to a regime where the motion is smaller than the wavelength of the light providing the dispersive force, or the “Lamb-Dicke”

regime, which usually restricts phonon numbers also to $\Delta\alpha^2 \sim 100$ in the previous largest case (to our knowledge) [104] and $\Delta\alpha^2 \ll 100$ for the heavier Yb atom. Multicomponent cat states have not previously been created in the motion of atoms.

Here we use ultrafast laser pulses to create cat states in the motion of a single $^{171}\text{Yb}^+$ ion confined in a harmonic trap with frequency $\omega/2\pi = 1$ MHz [1]. We characterize the coherence of the cat state by interfering the components of the superposition and observing fringes in the atomic populations mapped to the qubit. We achieve the largest phase space separation in any quantum oscillator to date—a superposition with $\Delta\alpha \approx 20$ (209 nm maximum separation compared to a $x_0 = 5.4$ nm spread of each component) and involving up to 400 phonons, with 20% interference contrast. The ultrafast nature of the cat generation is less restrictive on nonlinearities in the forces on the atom, and allows for very fast state creation with $\Delta\alpha = 0.4$ per laser pulse period (12 ns). Finally, we demonstrate a method to create 3-, 4-, 6- and 8-component cat states by timing the laser pulses at particular phases of the harmonic motion in the trap. These tools allow us to create and measure fragile mesoscopic states before they lose coherence.

In these experiments, the ion is subjected to 3-dimensional harmonic confinement (resonant frequencies $\omega_x \neq \omega_y \neq \omega_z$) within the radiofrequency Paul trap detailed in past work by our group [42]. We prepare cat states in the x -direction oscillator mode ($\omega = \omega_x$). The two hyperfine ground states of $^{171}\text{Yb}^+$ ($|\downarrow\rangle \equiv |F = 0, m_f = 0\rangle$ and $|\uparrow\rangle \equiv |F = 1, m_f = 0\rangle$, with qubit splitting $\omega_{hf}/2\pi = 12.642815$ GHz) are used to split coherent states of the atom motion through a strong state-dependent kick (SDK) [33]. The qubit can also be coherently manipu-

lated without motional coupling using resonant microwave pulses.

Each experiment follows the same general procedure. We initialize the atom's motion by Doppler laser cooling followed by resolved sideband cooling [33]. (Ground state population is 87%, and a thermal average is used when comparing data to theory [33], but the state will be represented from here as $|n=0\rangle$ for simplicity.) Optical pumping initializes the qubit state to $|\downarrow\rangle$ [56], and then a pair of microwave $\pi/2$ pulses with variable relative phase are applied to the ion with a delay between them. During the time between microwave pulses, the ion motion is excited using two sets of SDKs (separated by time T) to create a cat state and then reverse the process. The state is measured at the end of each experiment using qubit state-dependent fluorescence [56]. This sequence is detailed in the upper part of Fig. 5.1a.

A single SDK is created with a series of eight laser pulses of duration $\tau \approx 10$ ps and center optical wavelength $2\pi/k = 355$ nm. Each of the pulses is divided and applied to the ion simultaneously in counter-propagating directions and orthogonal linear polarizations (Fig. 5.1a, lowest box). The counter-propagating pulses, each with effective intensity envelope [32] $\text{sech}(\pi t/\tau)$ and bandwidth spanning the hyperfine structure but much less than the fine structure, produce a polarization gradient at the ion [61] and couple the qubit and ion motion with a strength modulated along the x -direction. A pair of pulses arriving at time $t = 0$ drives such a modulated Raman process (Fig. 5.1b) with the approximate Hamiltonian [32]

$$\hat{H}(t) = \Omega(t) \sin[2kx_0(\hat{a}^\dagger + \hat{a}) + \phi] \hat{\sigma}_x + \frac{\omega_{hf}}{2} \hat{\sigma}_z, \quad (5.1)$$

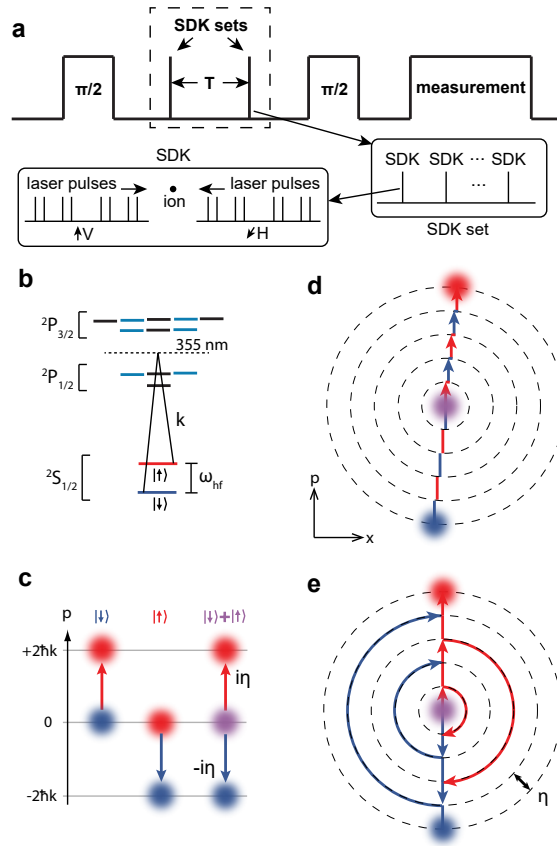


Figure 5.1: Experimental schedule and coherent state control. (a) Spin-dependent kicks (SDKs) are concatenated in various ways to generate large cat states. This process is performed between two microwave $\pi/2$ pulses with variable relative phase before the final state is measured. For simplicity, only kicks that affect the initial population in $|\downarrow\rangle$ are drawn with arrowheads. (b) Stimulated Raman transitions through virtual excited states near 355 nm couples the qubit to the ion motion. The $\omega_{hf} = 12.642815$ GHz hyperfine splitting of the $^2S_{1/2}$ serves as a qubit. (c) The Wigner phase space representation of a state-dependent kick (SDK). A single SDK displaces a coherent state by $2\hbar k$ ($i\eta$ in momentum space) in a direction that depends on the initial qubit state (red: $|\uparrow\rangle$ or blue: $|\downarrow\rangle$), and splits a coherent state associated with a qubit superposition (purple: $\propto |\uparrow\rangle + |\downarrow\rangle$). (d) By changing the direction of the laser beams between each SDK, every pulse from a mode-locked laser is used to create a large cat state. (e) Applying SDKs at intervals synchronous with half of the trap period oscillation cycle, the cat state grows without the need to change the laser direction. Free evolution appears in these plots as circular orbits.

where $\hat{\sigma}_{x,z}$ are Pauli spin operators, ϕ is the relative phase between the counter-propagating light fields and is considered constant during a pulse, \hat{a}^\dagger and \hat{a} are the raising and lowering operators of the ion motion, and $\Omega(t) = (1/2)(\Xi/\tau)\text{sech}(\pi t/\tau)$ is the Rabi frequency with pulse area Ξ .

The interaction described in Eq. 5.1 yields the well known Kapitza-Dirac scattering process [1] by which the atomic motional wave diffracts from a light field grating into all momenta classes $n2\hbar k$ with population dictated by the Bessel function $J_n(\Xi)$, and $n \in \mathbb{Z}$ [32]. By applying a series of eight pulses ($\Xi \approx \pi/8$ for each) in which the phase ϕ is appropriately shifted between each pulse using an acousto-optic modulator, we achieve a qubit state-dependent coherent momentum transfer of $\pm 2\hbar k$ (+ for $|\downarrow\rangle$ and $-$ for $|\uparrow\rangle$) along a single oscillator mode while the atom's motion is effectively frozen in time [1, 32, 33]. This SDK process approximately evolves the quantum state as

$$\hat{U}_{SDK} = \hat{\sigma}_+ \hat{\mathcal{D}}[i\eta] + \hat{\sigma}_- \hat{\mathcal{D}}[-i\eta], \quad (5.2)$$

without making the Lamb-Dicke approximation $\eta\sqrt{2n+1} \ll 1$, where $\hat{\sigma}_\pm$ are the qubit raising and lowering operators, and $\eta = 2kx_0 = 0.2$ is the Lamb-Dicke parameter, and $\hat{\mathcal{D}}$ is the displacement operator. Figure 5.1c depicts the SDK process in which the coherent state is shown in its Wigner representation [106] as a disk in phase space and the color represents the associated qubit state (the superposition states in this letter are drawn for intuitive purposes and are not scale). Note that each momentum displacement is associated with a qubit flip. Each SDK has a fidelity of 0.991, and this operation may be concatenated multiple times (Fig. 5.1,

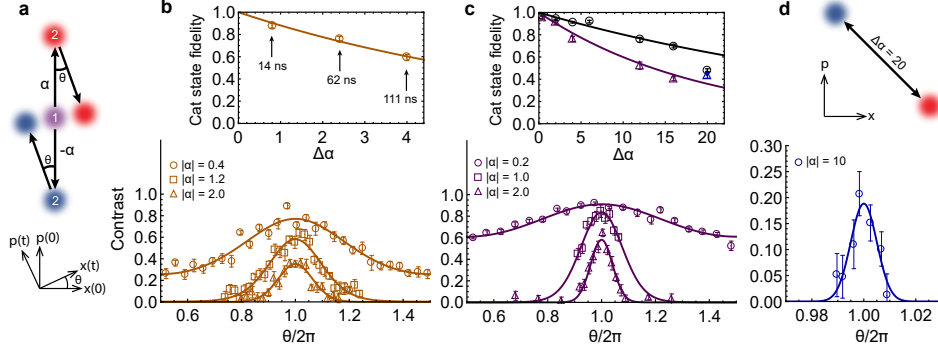


Figure 5.2: Cat state creation and verification. (a) The state $|\psi_1\rangle$ (labeled “1”) is split using a set of SDKs to create the cat state $|\psi_2\rangle$ (“2”). After evolution $\theta = \omega T$, a second set of SDKs drives the state to $|\Psi_{cat}\rangle$. (b) The cat state $|\psi_2\rangle$ with $\alpha = 0.4$ is generated in about 14 ns, $\alpha = 1.2$ in 62 ns, and $\alpha = 2.0$ in 111 ns. The states are verified by observing contrast in the state $|\Psi_{cat}\rangle$ (lower plot). We find the fidelity of each cat state $|\psi_2\rangle$ to be 0.88(2), 0.76(2), and 0.59(3), respectively (upper plot). (c) Using a higher fidelity technique which grows in α at an average rate $\eta\omega/\pi$, cat states are generated and verified by observing contrast revival (lower plot). Shown in the upper plot, cat state fidelity decays with the number of SDKs applied, and the effective single SDK fidelities are 0.9912(6) and 0.978(2) for Doppler (black, circles) and ground state cooled atoms (purple, triangles). (d) A cat state of $\Delta\alpha = 20$ is measured with a contrast revival peak of $C_0 = 0.19(3)$. Error bars are calculated with confidence interval of one sigma.

middle box) to generate arbitrary cat states, so long as the atom’s motion stays confined within the harmonic trapping region $|\alpha| \lesssim 10^4$.

In the first of three experiment types, we demonstrate our fastest method for generating cat states by using every pulse that is emitted from a mode locked laser (repetition rate $f_{rep}=81.4$ MHz) to generate a set of N SDKs. This is achieved by separating each pulse from the laser into the eight pulses required for an SDK, in addition to adding optical elements capable of physically swapping the direction of the counter-propagating pulses (see later section on Experimental Setup). Swapping

the direction compensates for the spin flip that occurs after each SDK and allows for fast concatenation of constructive momentum transfers (Fig. 5.1d). Starting each experiment, the ion is initialized in the state $|\psi_1\rangle = \frac{1}{\sqrt{2}}(|\downarrow\rangle + |\uparrow\rangle)|0\rangle$ using resonant microwaves. We apply a series of N SDKs which cause the superposition to grow in size at a rate $\frac{d|\alpha|}{dt} \approx \eta f_{rep}$ (this rate holds for small enough N , see Experimental Setup section), approximately generating the cat state $|\psi_2\rangle = \frac{1}{\sqrt{2(1+e^{-|\alpha|^2})}}(|\uparrow\rangle|\alpha\rangle + |\downarrow\rangle|-\alpha\rangle)$. After allowing the state to evolve for varying amounts of time T , then applying a second identical set of displacement operators, the state

$$|\Psi_{cat}\rangle \propto |\uparrow\rangle|-\alpha e^{-i\theta} + \alpha\rangle + |\downarrow\rangle|\alpha e^{-i\theta} - \alpha\rangle \quad (5.3)$$

is ideally created, where $\theta = \omega T$ (Fig. 5.2a). The phase of the second microwave $\pi/2$ pulse is scanned to probe the qubit contrast [32]

$$C(\theta) = C_0 e^{-4|\alpha|^2(1-\cos\theta)} \quad (5.4)$$

where $C_0 < 1$ accounts for imperfect operations. At integer multiples of the trap period $\theta = 2\pi m; m \in \mathbb{Z}$, we observe revivals in contrasts, and when $|\alpha| \gg \frac{1}{\sqrt{2}}$, the revival lineshape is approximately Gaussian with a FWHM of $1.18/|\alpha|$. In Fig. 5.2b, revival lineshapes at $\theta = 2\pi$ are shown in which the state $|\psi_2\rangle$ is generated for (up to) $\Delta\alpha = 4.0$ in 111 ns with fidelity of $F = 0.59(3)$ estimated using the relation $F = C_0^{1/2}$. This gives an effective single SDK fidelity of 0.951(4), which is lower than that of a true single SDK because of power fluctuations associated with swapping laser directions. Such a demonstration is an important benchmark for ultrafast quantum information processing.

In a second set of experiments, we create large cat states using a technique that does not require switching laser beam paths and instead works by delivering an SDK at every half trap period to excite large superpositions (Fig. 5.1e). This maintains high SDK fidelity by leaving the beam paths stationary, and the cat state grows at an average rate of $\frac{d|\alpha|}{dt} = \eta\omega/\pi$. Using this method we produce and verify states $|\Psi_{cat}\rangle$ up to $\Delta\alpha = 20$ (Fig. 5.2c,d). This largest state, with $100\hbar k$ of momentum in each coherent state, has a 209 nm maximum separation and contrast $C_0 = 0.19(2)$. Generating the large superposition state requires a high level of trap stability, which is achieved using a rf stabilization procedure [42]. Additionally, the trap frequency ω is scanned for fine control in θ [33]. The total measured fidelity of each SDK is found to be 0.978(2) for displacing coherent states, and 0.9912(6) for Doppler cooled states. This discrepancy is most likely due to the slower rate of coherent cat state creation due to ground state cooling allowing slower drifts to have effects.

The speed, fidelity, and high level of control in ultrafast operations allows us to make more complicated, multicomponent cat states. First, we create three and four component cat states with one additional microwave pulse and SDK set. Starting from the state $|\psi_2\rangle$, a microwave $\pi/2$ pulse rotates the state to $|\psi_3\rangle \propto (|\uparrow\rangle - |\downarrow\rangle)|\alpha\rangle + (|\uparrow\rangle + |\downarrow\rangle)|-\alpha\rangle$. A set of SDKs then produces three and four component cat states of the form

$$\begin{aligned}
|\Psi_{cat}^{3,4}\rangle \propto & |\uparrow\rangle (e^{i\phi_1} |\alpha e^{-i\theta} + \alpha\rangle + e^{i\phi_2} |\alpha e^{-i\theta} - \alpha\rangle) \\
& + |\downarrow\rangle (e^{i\phi_3} |-\alpha e^{-i\theta} + \alpha\rangle + e^{i\phi_4} |-\alpha e^{-i\theta} - \alpha\rangle),
\end{aligned} \tag{5.5}$$

with configuration depending on θ (Fig. 5.3a). (phases ϕ_1 , ϕ_2 , ϕ_3 , and ϕ_4 discussed

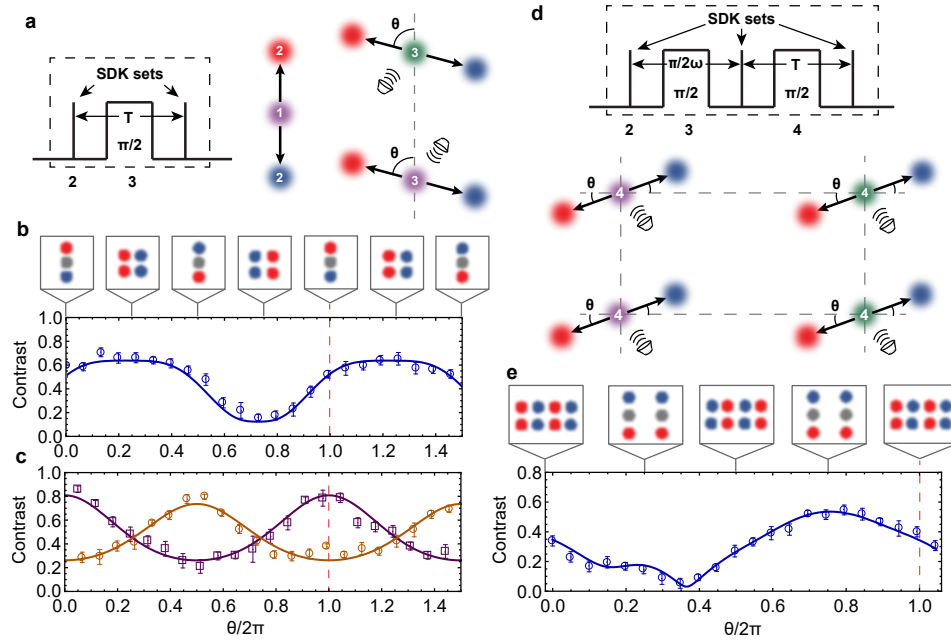


Figure 5.3: Three, four, six and eight-component cat states. (a) Creation of a multicomponent cat state begins by applying a set of SDKs to take the state $|\psi_1\rangle$ (1) to the state $|\psi_2\rangle$ (2). A microwave $\pi/2$ pulse rotates the qubit to produce the state $|\psi\rangle \propto (|\uparrow\rangle + |\downarrow\rangle)|\alpha\rangle + (|\uparrow\rangle - |\downarrow\rangle)|-\alpha\rangle$ (3). Another set of SDKs generates the three or four-component cat state. The diagram within the dashed line replaces the one in Fig. 5.1a for these experiments. (b) If $\theta = 0$, two of the components rejoin and the state has the form $|\alpha\rangle + |0\rangle + |-\alpha\rangle$. If $\theta = \pi/4$, for instance, then a four-component cat state of the form $|\alpha\rangle + |-\alpha\rangle + |i\alpha\rangle + |-i\alpha\rangle$ is generated. The final microwave pulse analyzes the state contrast, and is plotted as a function of θ , which is compared with the predicted contrast curve with only the amplitude as a fitting parameter. Error bars are calculated with confidence interval of one sigma. (c) If the microwave $\pi/2$ pulse in (a) is replaced by a $m\pi$ pulse, then the second SDK set behaves as it would in the 2-component experiment, with the exception that odd values of m are shifted by half of a trap period. We see this behavior fits the predicted model well. (d) The six and eight-component state is created by extending the technique for the three and four-component state with an additional microwave pulse and SDK set. (d) Contrast as a function of θ is used to verify the creation of the cat state when compared to the model (solid line).

in Three and Four-Component Cat Contrast section). It is evident from Eq. 5.5 that a three-component cat state is created when $\theta = m\pi$, and a four-component cat state is generated for other values of θ . Scanning θ and the phase of a final analysis microwave $\pi/2$ pulse, we observe a contrast lineshape indicative of the desired state (Fig. 5.3b). To further verify that these multicomponent states are being created, we run the same sequence but apply either no microwave pulse, or a π pulse, to the state $|\psi_2\rangle$. An SDK set then generates the cat states $|\Psi_{cat,0}\rangle \propto |\uparrow\rangle |-\alpha e^{-i\theta} + \alpha\rangle + |\downarrow\rangle |\alpha e^{-i\theta} - \alpha\rangle$ and $|\Psi_{cat,\pi}\rangle \propto |\downarrow\rangle |\alpha e^{-i\theta} + \alpha\rangle + |\uparrow\rangle |-\alpha e^{-i\theta} - \alpha\rangle$. These states revive at the same frequency, but out of phase by π , which is verified in Fig. 5.3c.

Continuing to unfold the state in phase space, another microwave $\pi/2$ rotation and SDK set generates a six and eight-component cat state (Fig. 5.3d). In this case, the four component cat state is generated with a separation along one quadrature double that of the other to allow for a square lattice once the eight component state is created. Again, scanning θ and the phase of a final microwave pulse, Ramsey fringes are observed which compare well with the expected behavior (Fig. 5.3e). (See Six and Eight-Component Cat Contrast for more details.)

Ultrafast laser pulses are capable of generating Schrödinger cat states larger than presented here, theoretically limited by the anharmonicity of the trap at large displacements. This technique can also be used to make even more complicated multicomponent states, as well as generate them in two and three dimensions by modifying the trapping potential and orientation. If a larger separation is desired for a measurement such as rotation sensing [107], lowering the trap frequency by 10

times would increase the separation by 10 times.

5.1 Experimental Setup

Laser pulses are generated from a frequency tripled, mode-locked Nd:YVO₄ laser. A pulse is divided into eight using a series of beam splitters and delays in a Mach-Zehnder interferometer configuration. The spin-dependent displacement in Eq. 5.2 has the more precise form

$$\hat{O}_{SDK} = e^{i\phi_\lambda} \hat{\sigma}_+ \hat{\mathcal{D}}[i\eta] + e^{-i\phi_\lambda} \hat{\sigma}_- \hat{\mathcal{D}}[-i\eta]. \quad (5.6)$$

The phase ϕ_λ is an optical phase that is assumed to be stable during the course of one experiment, but random over multiple experiments due to slow mechanical and other noise on the optics. Effects of the phase ϕ_λ cancel when an even number of applications of the operator \hat{O}_{SDK} are used during an experiment and so is dropped in Eq. 5.2.

The first method discussed for generating cat states uses every pulse from the mode-locked laser to produce SDKs (Fig. 5.1d). This works by swapping the directions of the counter-propagating beams, countering the spin flip that occurs with each SDK. To make this swap, we combine the perpendicular linearly polarized beams on a polarizing beam splitter and pass them through a Pockels cell. The cell can rotate the polarizations by 0 or $\pi/2$ radians arbitrarily for pulses arriving every 12 ns, here we alternate every pulse. A polarizing beam cube downstream of the Pockels cell separates the two beams after which they are directed, counter-propagating, onto the ion with simultaneous arrivals. As mentioned, the rate at

which the state grows is $\frac{d|\alpha|}{dt} \approx \eta f_{rep}$ for small enough N . This holds for $N \ll 2\pi f_{rep}/\omega$, but for large enough N , the rate decrease as trap evolution counteracts the kicks. This rate cycles every half trap period because the photon momentum adds most constructively when applied during the high momentum periods of the oscillation. This is evident in Fig. 5.1d by the deviation of the coherent state from the p -axis.

5.2 Three and Four-Component Cat Contrast

The contrast function which overlays the data in Fig. 5.3b is derived here. We write the time evolution operator for a coherent state as $\hat{U}_T[\theta]|\alpha\rangle = |\alpha e^{-i\theta}\rangle$. The microwave rotation operator in the z-basis is written as

$$\hat{R}_\mu[\phi_\mu] = \frac{1}{\sqrt{2}}\hat{\mathbb{1}} \otimes \begin{bmatrix} 1 & e^{i\phi_\mu} \\ -e^{-i\phi_\mu} & 1 \end{bmatrix}, \quad (5.7)$$

where all rotations have pulse area $\pi/2$. A full Ramsey experiment to create three and four-component cat states, including microwave rotations, SDKs, free evolution, and a final analysis microwave pulse produces the final state

$$\begin{aligned} |\Psi_f^\beta\rangle &= \hat{R}_\mu[\phi_\mu'''] \cdot \hat{O}_{SDK} \cdot \hat{U}_T[\pi] \cdot \hat{O}_{SDK} \cdot \hat{U}_T[\theta] \cdot \\ &\hat{R}_\mu[\phi_\mu''] \cdot \hat{O}_{SDK} \cdot \hat{U}_T[\pi] \cdot \hat{O}_{SDK} \cdot \hat{R}_\mu[\phi_\mu'] \cdot |\downarrow\rangle |\beta\rangle. \end{aligned} \quad (5.8)$$

The spin-up portion of the final state is given as

$$\begin{aligned}
& \exp(-2i\eta\beta_R + 2i\eta\text{Re}[e^{-i\theta}(2i\eta - \beta)] + i\phi''_\mu - i\phi'_\mu - i\phi'''_\mu) |-2i\eta - e^{-i\theta}(2i\eta - \beta)\rangle \\
& - \exp(-2i\eta\beta_R - 2i\eta\text{Re}[e^{-i\theta}(2i\eta - \beta)] - i\phi'_\mu) |2i\eta - e^{-i\theta}(2i\eta - \beta)\rangle \\
& - \exp(2i\eta\beta_R - 2i\eta\text{Re}[e^{-i\theta}(-2i\eta - \beta)] - i\phi''_\mu) |2i\eta - e^{-i\theta}(-2i\eta - \beta)\rangle \\
& - \exp(2i\eta\beta_R + 2i\eta\text{Re}[e^{-i\theta}(-2i\eta - \beta)] - i\phi'''_\mu) |-2i\eta - e^{-i\theta}(-2i\eta - \beta)\rangle,
\end{aligned} \tag{5.9}$$

where the normalization factor and spin-up ket is left out for simplicity. The brightness for any thermal state with average phonon occupation \bar{n} is given as

$$B = \frac{1}{\pi\bar{n}} \int_{-\infty}^{\infty} e^{-|\beta|^2/\bar{n}} \langle \uparrow | \Psi_f^\beta \rangle \langle \psi_f^\beta | \uparrow \rangle d^2\beta. \tag{5.10}$$

For an ion initially in a thermal motional state the brightness is

$$\begin{aligned}
& \frac{1}{4} \left[1 + e^{16(1+2\bar{n})\eta^2(\cos\theta-1)} \cos(\phi'_\mu - \phi'''_\mu) \right] \\
& + \frac{1}{4} \left[1 - e^{-32(1+2\bar{n})\eta^2 \cos^2(\frac{\theta}{2})} \cos(2\phi''_\mu - \phi'_\mu - \phi'''_\mu) \right] \\
& + \frac{1}{\sqrt{8}} e^{-8(1+2\bar{n})\eta^2} \sin(16\eta^2 \sin\theta) \sin(\phi''_\mu - \phi'''_\mu).
\end{aligned} \tag{5.11}$$

5.3 Six and Eight-Component Cat Contrast

This calculation is carried out in the same fashion, using the full set of operations

$$\begin{aligned}
|\Psi_f^\beta\rangle = & \hat{R}_\mu[\phi_\mu'''''] \cdot \hat{O}_{SDK} \cdot \hat{U}_T[\pi] \cdot \hat{O}_{SDK} \cdot \hat{U}_T[\theta] \\
& \cdot \hat{R}_\mu[\phi_\mu'''''] \cdot \hat{O}_{SDK} \cdot \hat{U}_T[\pi] \cdot \hat{O}_{SDK} \cdot \hat{U}_T[\pi] \\
& \cdot \hat{O}_{SDK} \cdot \hat{U}_T[\pi] \cdot \hat{O}_{SDK} \cdot \hat{U}_T[\frac{\pi}{2}] \cdot \hat{R}_\mu[\phi_\mu''] \\
& \cdot \hat{O}_{SDK} \cdot \hat{U}_T[\pi] \cdot \hat{O}_{SDK} \cdot \hat{R}_\mu[\phi_\mu'] \cdot |\uparrow\rangle |\beta\rangle.
\end{aligned} \tag{5.12}$$

We do not show the full brightness calculation here because of its length. The solid line in Fig. 5.3e is a fit assuming that the initial motional state is $\beta = 0$. Our initial thermal occupation number is $\bar{n} = 0.15$, or about 87% in the ground state. We do not take the thermal average because our computer could not perform the intensive calculation in less than a couple of days per run. A simpler calculation including only the lowest phonon states would be simpler, but was not done because of the good agreement without averaging.

5.3.1 Sources of Error

Several factors lead to less than perfect fidelity of the cat states we create. One restriction on the size of cat states we can generate and measure comes from Doppler cooling issues. Frequency instability leads to fluctuations in the initial thermal state, leading to slower data taking (cooling takes longer, and the noisier data requires more averaging) and sensitivity to slow noise. The ion is exposed

to off resonant light during the time that SDKs are being applied. This causes a Stark shift in the qubit splitting. SDK fidelity is discussed in other sources [1, 33]. The trap axes are rotated so that the Raman beam couples only to a single mode. Misalignment of this means some amount of motion is excited in other directions, and is not recovered. Detection fidelity is discussed in other work [62]. Finally, it is worth acknowledging that the trap is about 1 mm across in both directions (the motional wave packet for the largest state has a spread of about 200 nm), and non-harmonic contributions are negligible to the motion behavior.

Chapter 6: Highly Sensitive Atom Imaging

The optical imaging of isolated emitters, such as individual molecules [108, 109], optically active defects in solids [110], fluorescent dyes in a solution [111], or trapped atoms [48, 112], relies on efficient light collection and excellent image quality [113]. Such high resolution imaging underlies many methods in quantum control and quantum information science [48, 112], such as quantum networks [114], fundamental atom-light interactions [115], and sensing small scale forces [116]. Individual atoms in particular have been resolved and imaged for many such applications [62, 117–123], with performance that depends critically on minimizing misalignments and optical aberrations from intervening optical surfaces such as a vacuum window.

In this chapter we develop a general method for suppressing aberrations by characterizing and adapting the imaging system, and report the highest performance optical imaging of an isolated atom to date. We image a single $^{174}\text{Yb}^+$ atomic ion with a position sensitivity of $\approx 0.5 \text{ nm}/\sqrt{\text{Hz}}$ for averaging times less than 0.1 s, observe a minimum uncertainty of 1.7(3) nm, and obtain direct measurements of the nanoscale dynamics of atomic motion. Complete knowledge on the wavefront distortions is obtained through the Zernike expansion of the point spread function and we adapt this information to correct aberrations and misalignments. The gen-

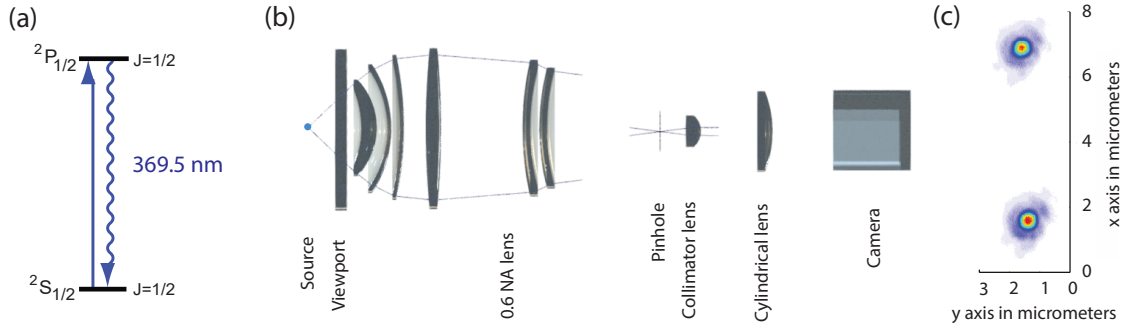


Figure 6.1: Schematic of the imaging system [43]. (a) Atomic energy diagram of $^{174}\text{Yb}^+$. The atom is excited with laser radiation at 369.5 nm driving the $^2S_{1/2} \rightarrow ^2P_{1/2}$ cycling transition and the resulting fluorescence is collected by the imaging system. (b) Transverse cut of the optical setup depicting the source, vacuum window, 0.6 NA objective lens, pinhole, short focal length lens, cylindrical lens and camera. (c) Image of two atomic ions separated by $\sim 5 \mu\text{m}$.

erality of the described work opens the door for improvement in adaptive optical imaging in many other quantum optical systems as well as other contexts, such as biological microscopy or astronomy.

6.1 Experimental Apparatus

The atomic imaging system is shown in Fig. 6.1. In this experiment, we confine a single $^{174}\text{Yb}^+$ ion (the 174 isotope has no hyperfine splitting and so can fluoresce more brightly) in the linear Paul trap with 3D harmonic oscillation frequencies $(\omega_x, \omega_y, \omega_z)/2\pi = (1, 1.2, 0.8)$ MHz. Just as in the experiments with $^{171}\text{Yb}^+$, laser light at a wavelength of $\lambda = 369.5$ nm is incident on the ion and resonantly excites the $^2S_{1/2} \rightarrow ^2P_{1/2}$ cycling transition (radiative linewidth $\gamma/2\pi = 20$ MHz) as shown in Fig. 1(a). The ion is laser-cooled and localized in each of the three dimensions

of position to $\Delta x = \sqrt{(2\bar{n} + 1)}x_0$, where $x_0 = \sqrt{\hbar/2m\omega_x} \approx 5$ nm is the zero-point spread, \bar{n} is the mean thermal vibrational occupation number along each of the dimensions of motion, and m is the atomic mass. From Eq. 2.14, the cooling laser at an oblique angle to all directions of motion produces $\bar{n} \approx \gamma/2\omega_x \sim 10$. Thus, $\Delta x \sim 20$ nm $\ll \lambda$ and the trapped ion acts as an excellent approximation to a point source.

The approximately isotropic fluorescence from the atom at $\lambda = 369.5$ nm is transmitted through the vacuum viewport and collected by an objective lens of numerical aperture NA = 0.6 with 10x magnification [62] (Fig. 6.1(b)). An intermediate image from the objective is formed at a pinhole, which spatially filters light from background sources. A second lens, after the pinhole, re-images the ion at the face of an electron-multiplying-charge-coupled-device (EMCCD) array (camera) with about 50x magnification (Fig. 6.1(c)). This makes the total magnification about (10x)(50x)=500x. The objective lens is mounted on a precision 5-axis alignment stage to compensate for comatic aberrations, and cylindrical optics are inserted after the magnifier lens to compensate for astigmatic aberrations (chosen after looking at the aberrations on the camera).

6.2 Aberration measurement and correction

The measured spatial distribution of the image is the point spread function (PSF) [124] which contains information about the ultimate resolution achievable in an imaging system and is the building block for more complex image formation

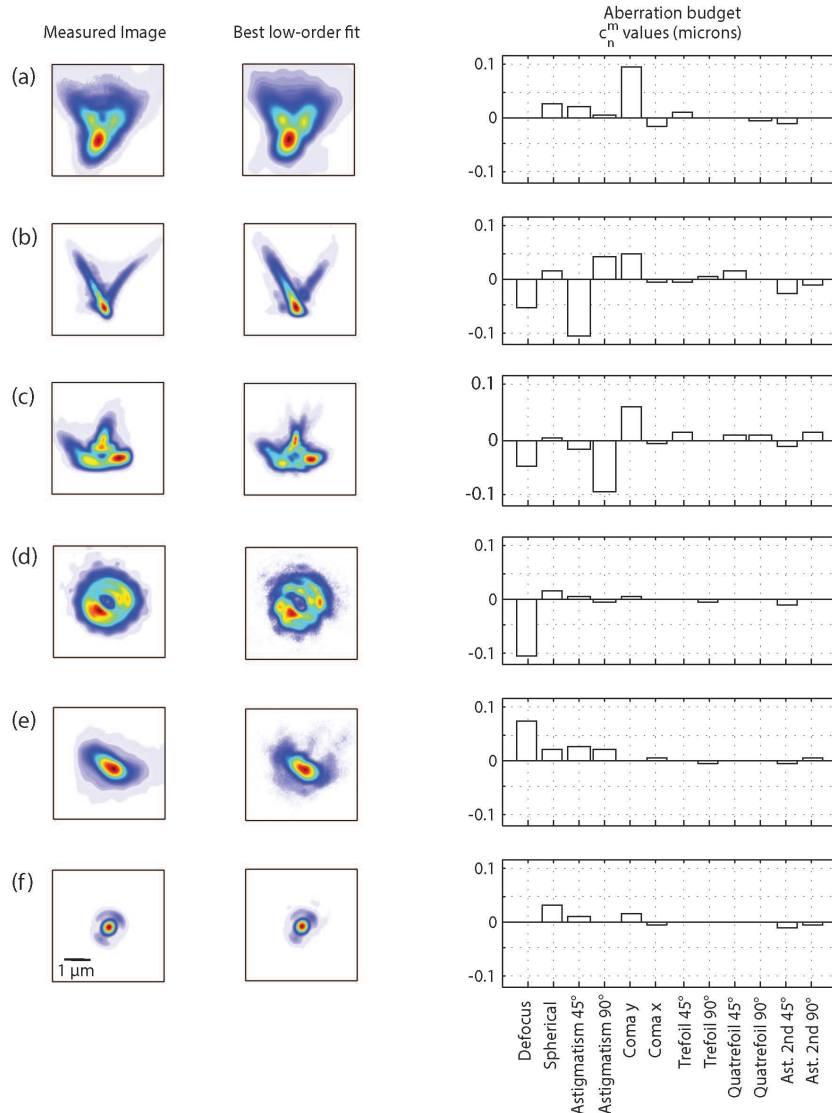


Figure 6.2: Aberration retrieval results [43]. (a), (b), (c) Single shot images of the misaligned system. (d), (e), (f) The optimally aligned system at various distances from the focal plane, with (f) at the best focus. For (d) and (e) a high contribution from the defocus term is evident with low contributions of astigmatism and coma. Large contributions of coma and astigmatism (a)-(c) are corrected with a 5-axis stage and cylindrical lens. Coefficients of determination are 0.989, 0.965, 0.958, 0.957, 0.983 and 0.994 for images (a), (b), (c), (d), (e) and (f) respectively. These images are integrated for ~ 0.5 s.

through convolution techniques. The PSF can be decomposed into Zernike polynomials $Z_n^m(\rho, \theta)$ in space

$$\text{PSF}(\rho, \theta) = \left| \mathcal{F} \left\{ \exp \left(-ik \sum_{m,n} c_n^m Z_n^m(\rho, \theta) \right) \right\} \right|^2, \quad (6.1)$$

where $\mathcal{F}\{\}$ is the Fourier transform operator, $k = 2\pi/\lambda$ is the wavenumber and the c_n^m coefficients are contributions of each Zernike component defined in the polar coordinates ρ and θ . The c_n^m coefficients correspond to particular optical aberrations, so detailed characterization of the imaging system follows from the determination of the sign and magnitude of these coefficients.

Although optical aberrations can be described in terms of a Taylor expansion of the object height and pupil coordinates [125], Zernike polynomials $Z_n^m(\rho, \theta)$ are better suited since they form an orthogonal basis set of functions. Zernike polynomials are expressed in polar coordinates ρ and θ as [126]

$$Z_n^m(\rho, \theta) = \begin{cases} N_n^m R_n^m(\rho) \cos(m\theta) & \text{for } m \geq 0 \\ N_n^m R_n^m(\rho) \sin(m\theta) & \text{for } m < 0, \end{cases} \quad (6.2)$$

$$N_n^m = \sqrt{\frac{2(n+1)}{1 + \delta_{m0}}}, \quad (6.3)$$

$$R_n^{|m|}(\rho) = \sum_{s=0}^{(n-|m|)/2} \frac{(-1)^s}{s![(n+|m|)/2-s]!} \times \frac{(n-s)!}{[(n-|m|)/2-s]!} \rho^{n-2s}, \quad (6.4)$$

where n is an integer number, m can only take values $n, n-2, n-4, \dots, -n$ for each n , and δ_{m0} is the Kronecker delta. The radial coordinate is normalized to the exit pupil radius (the radius of the image of the input aperture at the camera). Importantly, each term of this polynomial expansion has a one-to-one relation with

a specific kind of aberration. Given the Zernike expansion of a wavefront, we can calculate its deviation from a perfect wavefront using the c_n^m coefficients of eq. (6.1).

Decomposing an image into Zernike polynomials relies on numerical algorithms [127, 128] or semi-analytical calculations [129]. Here we obtain a full aberration characterization by using a least-squares fit to the measured data, using the c_n^m coefficients and the exit pupil radius as fitting parameters. Although this method omits consideration of vector (polarization) effects, it remains a generally applicable technique since these effects can be neglected at numerical apertures above 0.6 NA [130].

Fig. 6.2 shows six single-shot images of a single $^{174}\text{Yb}^+$ ion. Figures 6.2(a)-(c) were taken during alignment and Figs. 6.2(d)-(f) were taken at different distances from the focal plane of the optimally aligned system. The images were integrated for ~ 0.5 s, collecting $\approx 7 \times 10^5$ photons and fitted according to Eq. 6.1 to a linear superposition of the first twelve Zernike polynomial basis functions. The overall fitting function is then smoothed by convolving with a Gaussian function that best fits the data and accounts for spatial drifts over long exposures. The Gaussian function parameters are added to the fitting algorithm and are only important for integration times longer than 0.2 s (See next section and supplemental materials). We find that the optimal image (Fig. 6.2(f)) has a characteristic radius of $\rho_0 = 363(18)$ nm, consistent with the diffraction-limited Airy radius of $\rho_0 = 0.61\lambda/\text{NA} = 375.1$ nm given the system numerical aperture.

Based on the one-to-one mapping of the Zernike polynomials to optical aberrations, we plot an aberration budget which shows the leading order aberration

contributions to each of the images. For example, the contribution of the dominating negative (positive) defocus term of Fig. 6.2(d) (Fig. 6.2(e)) shows that we can map axial displacement on a transverse image distribution, with the position of best focus shown in Fig. 6.2(f). Moreover, a contribution of the comatic aberration indicates angular tilt errors and non-zero values of astigmatism indicate anisotropic foci in the system, seen in Figs. 6.2(a)-(c).

Fitting results show parameter uncertainties on the order of 1 nm, providing a full quantitative basis for analyzing systems that rely on aberrations to extract information on particle dynamics. Examples of these experiments involve 3d off-focus tracking [131] and imaging of atoms arranged in 3d lattices [132]. Although we describe an atomic emitter, this method can also be applied to the imaging of microbiological test samples.

6.3 Position sensitivity

The precision of measuring atomic position is dependent on the imaging system light collection and quality. As a result of the optical aberration characterization, even if it is not possible to directly correct the aberrations in the imaging system by alignment, it is feasible to post process and actively feedback the aberrated image and obtain a diffraction-limited performance through a digital filter with the information of the Zernike expansion. In this experiment we only correct the aberrations by direct alignment.

We measure the sensitivity to the position by taking N images at 1 ms exposure

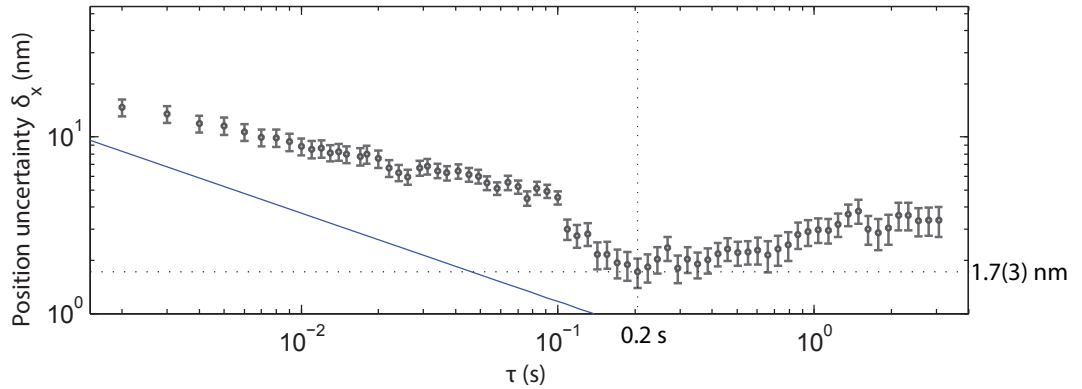


Figure 6.3: Measured position uncertainty δ_x of the trapped ion centroid position versus image integration time τ [43]. The blue line shows the expected uncertainty limited by photon counting shot noise in the imaging system. A sensitivity of $\sim 0.5\text{nm}/\sqrt{\text{Hz}}$ is measured for $\tau < 0.1$ s, which is ~ 3 times worse than shot noise, presumably because of camera noise. The ultimate position sensitivity is found to be $1.7(3)$ nm at $\tau = 0.2$ s. These measurements include small corrections for dead time bias, as described in Methods. The error bars on each point are given by the root-mean-square error.

time, binning them over total time duration intervals τ and calculating the Allan variance of the central position [133].

$$\sigma^2(\tau) = \frac{1}{2(M-1)} \sum_{n=1}^{M-1} (x_{n+1} - x_n)^2, \quad (6.5)$$

where M is the number of samples per bin and x_n is the centroid of the ion image integrated over time τ . Each image was integrated along one direction and fit to a one dimensional Gaussian linear count density function. The same procedure taken at different times τ leads to a curve of position uncertainty δ_x vs integration time as shown in Fig. 6.3. The data is corrected for a dead time of 5 ms between each 1 ms frame, allowing for state preparation and laser cooling [133, 134].

Dead times were corrected using the Allan B-functions [134]

$$\sigma^2(\tau) = \frac{\sigma^2(2, \mathcal{M}T_0, \mathcal{M}\tau_0)}{B_3(\mu)B_2(\mu)} \quad (6.6)$$

where μ is the noise model coefficient that ranges between $-1 < \mu < 1$, \mathcal{M} is the binning parameter, T_0 is the time between data acquisitions and τ_0 is the sampling time. Dead times are then defined as $t_{dead} = T_0 - \tau_0$ for single acquisition times. The integration time for the Allan variance is $\tau = \mathcal{M}\tau_0$. The noise model coefficient upon which the B-functions depend at each τ were found solving

$$\frac{B_1(\mu)}{B_3(\mu)} = \frac{\sigma^2(N, T, \tau)}{\sigma^2(2, \mathcal{M}T_0, \mathcal{M}\tau_0)} \quad (6.7)$$

for μ with $\sigma^2(N, T, \tau)$ defined as the standard variance.

The theoretical net position sensitivity for diffraction-limited imaging is a quadrature sum of three main (uncorrelated) sources of uncertainty: shot noise,

pixelation and background noise [135, 136]

$$\delta_x = \sqrt{\frac{2\rho_0^2}{R_0\tau} + \frac{l_p^2}{12R_0\tau} + \frac{16\pi\rho_0^4b}{R_0^2\tau^2}}, \quad (6.8)$$

where $b \approx 0.07$ is the mean background count rate per pixel, and $l_p \approx 33$ nm is the pixel size referred to the object (image pixel size divided by magnification). Recall $\rho_0 = 363(18)$ nm is the characteristic image radius. $R_0 = \eta_D F \gamma / 2$ is the maximum (saturated) measured fluorescence count rate from the atom, where $F \approx 10\%$ is the solid angle fraction of fluorescence collected, $\gamma / 2\pi = 20$ MHz is the radiative linewidth, and $\eta_D \approx 25\%$ is the quantum efficiency of the camera. Finite pixel size and background counts have negligible impact on the measured position sensitivity in this experiment. The observed sensitivity of ~ 0.5 nm/ $\sqrt{\text{Hz}}$ at small integration times is somewhat higher than the expected level of shot noise (shown as the blue line in Fig. 6.3), and is consistent with observed super-Poissonian noise on the camera. We measure a minimum uncertainty of $\delta_x \approx 1.7(3)$ nm at an integration time of $\tau = 0.2$ s. For longer integration times, drifts in the relative position between the optical objective and the trapped ion degrade the position uncertainty as shown in Fig. 6.3, and with simple mechanical improvements in the imaging setup the resolution can likely be pushed well below 1 nm.

Given this uncertainty in the position of the harmonically-bound ion, the sensitivity to detecting external forces is $\delta F = m\omega_x^2\delta_x$. Imagine trapping a single $^{174}\text{Yb}^+$ ion with $\omega_x / 2\pi = 10$ kHz (which is experimentally possible); this would correspond to a force sensitivity in the yoctonewton (10^{-24} N) scale, or an electric field at the $\mu\text{V}/\text{cm}$ scale. Unlike earlier work [116], this imaging force sensor applies to single

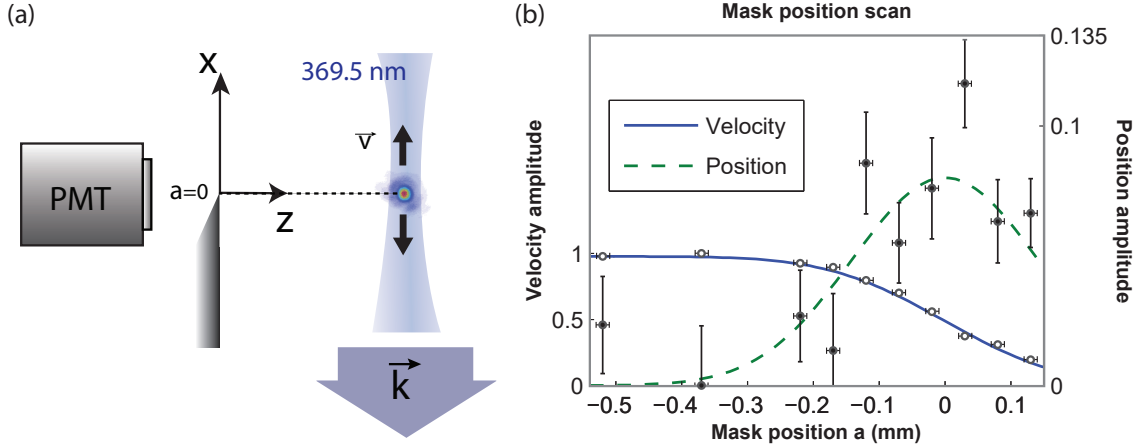


Figure 6.4: Micromotion position measurement [43]. (a) The ion's velocity \vec{v} (solid black arrows) is colinear with the direction \vec{k} of the detection light, taken to be the x -axis. The fluorescence is modulated from the micromotion of the ion along x by the first order Doppler effect as well as the obscuration by a mask with variable position a along the x -axis. (b) Contributions of the velocity (left y axis) and position (right y axis) of a single atom when a mask is scanned along one transversal direction x . The solid (dashed) line depict a fit to the data of the velocity (position) component of eq. 6.10 given by the cosine (sine) term alone. All the values are normalized with the signal amplitude at $a = -\infty$. The horizontal error bars are given by the uncertainty of the scanning stage (0.01 mm) and the vertical errors are computed by the uncertainty propagation using Eq 6.10.

ions and does not require resolution of optical sidebands. This could be used to measure tiny forces between trapped ionic molecules or atoms in a chain or gravitational effects.

6.4 Sensing of Rf Induced Micromotion Position

Confinement of atomic ions in a Paul trap is achieved through oscillating rf electric field gradients that create a harmonic ponderomotive potential [47]. In the

presence of a static uniform electric field E , which pushes the ion off of the rf null of the trap and into the oscillating field, the ion acquires a “micromotion” modulation in position $x(t) = X_\mu \sin \Omega t$ to first order in the pseudopotential approximation [15, 47], where Ω is the drive frequency of the rf trapping field (≈ 17 MHz in this experiment) and $X_\mu = \sqrt{2}eE/(m\Omega\omega)$ is the micromotion amplitude.

The conventional approach for sensing micromotion is based on the first order Doppler modulation in the scattering of light from a laser beam of wavenumber k propagating along the micromotion velocity [137] (See Fig. 6.4(a)). This is based on a principle where a moving atom sees a velocity-dependent laser frequency from the Doppler effect, and when the laser frequency is tuned to be on the slope of the resonance lineshape of the atom’s cooling transition, the scattering rate depends on the ion velocity. The correlation between the photon arrival times (measured with a photomultiplier tube) and the micromotion velocity is obtained with a time-to-digital converter. With the excitation laser red-detuned from resonance of order γ and for small levels of micromotion $kX_\mu \ll 1$, the measured fluorescence signal takes the form [138],

$$R(t) = \alpha R_0 + \beta R_0 \left(\frac{kX_\mu \Omega}{\gamma} \right) \cos \Omega t, \quad (6.9)$$

where $\alpha, \beta \leq 1$ are dimensionless constants that depend on the precise detuning and intensity of the excitation laser [138], and R_0 is the same as in Eq. 6.8.

In order to also sense a direct position sensitivity to motion, we spatially mask the ion image with a sharp edge aperture, normal to the (x) direction of motion. The mask position can be adjusted from, effectively, $a = -\infty$ (completely exposed)

to $a = +\infty$ (completely masked) with $a = 0$ covering exactly half of the image. The total fluorescence behind the mask is then the integrated fluorescence behind the exposed area,

$$R(a, t) = \alpha F(a) R_0 + \beta F(a) R_0 \left(\frac{k X_\mu \Omega}{\gamma} \right) \cos \Omega t + \alpha R_0 \frac{X_\mu}{\sigma \sqrt{\pi}} e^{-a^2/2\sigma^2} \sin \Omega t, \quad (6.10)$$

where we assume a Gaussian image distribution (approximating an Airy function) in space with root-mean-square radius $\sigma = 0.36\rho_0$ (conversion between Gaussian width and Airy width) and the scale of the mask position a is referred to the object. The first term in Eq. 6.10 is the average scattering rate spread over a Gaussian distribution and integrated over space where the mask is not present. This integration yields the error function $F(x) = [1 - \text{erf}(\frac{x}{\sigma\sqrt{2}})]/2$. The second term is found in the same way. The third term comes from a linear approximation of the scattering rate modulation due to small micromotion position fluctuations of the image at the mask.

We extract the two quadratures of the modulated fluorescence from Eq. 6.10 by performing sine and cosine transforms of the data. The phases of the modulated signal are calibrated by opening the aperture ($a = -\infty$) and taking the modulation as proportional to $\cos \Omega t$.

Figure 6.4(b) shows the position ($\sin \Omega t$) and velocity ($\cos \Omega t$) quadrature amplitudes (normalized to the amplitude at $a = -\infty$) as the mask position is scanned. Based on the observed velocity-induced modulation in the count rate with full exposure ($a = -\infty$), we infer a micromotion amplitude of $X_\mu \sim 20$ nm. As the mask is scanned along x , a position-dependent modulation in the fluorescence rate arises,

reaching a maximum level at $a = 0$. The absolute level of this position-dependent modulation is observed to be 15 times smaller than expected from Eq. 6.10. This may be due to fluctuations and drifts in the relative position of the ion with respect to the mask: fluctuations or drift of just 30 nm during the 300 s integration time required to obtain sufficient signal/noise ratio in the measurement would explain the observed reduction in the modulation. This could either be vibrations of the optical table, or the trapping system relaxing after loading (it takes up to one hour for the ion position to stop drifting after loading—an effect where it starts about 1 μm out of place after loading and returns to a repeatable spot over time). This type of measurement could allow us to minimize micromotion, although we did not because of the smaller than expected modulation.

6.5 Outlook

In the single atom emitter presented here, ultimate average position determination to the level of angstroms (10^{-10} m) should be possible for longer integration times, when drifts slower than 0.2 s are eliminated or actively corrected. Drifts may be reduced by further isolating the vacuum chamber from the environment and stabilizing the relative position between the sample and the objective. Since we obtain information of the centroid position, the zero-point ion motion does not affect these measurements.

More generally, the isolation and correction of wavefront distortions by fitting intensity images can be extended to the adaptive imaging of a variety of source

objects. If the fluorescence from the emitter is incoherent (not the case for multiple trapped ions illuminated with the same detection laser beam and within the coherence length of each other [139]), then imaging errors should not accumulate, and images from multiple emitters localized in distinct regions of space could be corrected. This technique can also be used for the optimization of laser output cavity spatial modes [140]. Most misalignments provide an unambiguous signature in the image decomposition, but for certain symmetric misalignments such as axial displacements about the focus for single-atoms, introducing additional aberrations like astigmatism [132] or coma will yield a unique fit. Given sufficient emitter brightness, active shot-to-shot adjustments and feedback to appropriate optical elements should allow the continuous optimization of image quality. The bandwidth of this type of adaptive imaging would be limited by the speed of the correction elements and the computing time for numerically extracting the error signal (this is ~ 1 s in our experiment).

Chapter 7: Realizing an Ultrafast Two Ion Gate

Trapped ions have proven to offer excellent quantum memory [141], in addition to serving as useful tools for quantum gates [2, 27, 29] and modular entanglement (quantum processing modules arbitrarily connected by photons in fibers and fiber switches) for scalable quantum computation [142–144]. Although they have a small gate-to-coherence time ratio, gate speeds have been limited by the trap evolution time. In this chapter, we demonstrate an entangling gate which is not fundamentally limited by trap evolution but instead by the Coulomb interaction between ions.

Entanglement between two ion qubits is generated using a series of SDKs with arbitrary kick direction, and periods of free evolution. As in the experiments with cat states, we restrict this entangling gate to a single axis of motion—a radial mode in this case. The radial mode is necessary because of the tunable ratio of the CoM (Center of Mass) and Relative modes of motion. Tuning the ratio of CoM and Relative mode of motion allows both paths to close in phase space, which disentangles the spin and motion and completes an entangling gate sequence.

7.1 Single Mode Phase Accumulation

First consider a single oscillator (frequency ω) in an initial coherent state $|\alpha_0\rangle$, which is kicked with magnitudes z_k at times t_k a total of n times yielding a final state $e^{i\xi_n} |\alpha(t_n)\rangle$ with [44]

$$\alpha(t_n) = e^{-i\omega t_n} \left(\alpha_0 + i \sum_{k=1}^n z_k e^{i\omega t_k} \right) \quad (7.1)$$

$$\xi_n = \text{Re} \left[\alpha_0 \sum_{k=1}^n z_k e^{-i\omega t_k} \right] - \sum_{k=2}^n \sum_{j=1}^{k-1} z_k z_j \sin[\omega(t_j - t_k)]. \quad (7.2)$$

When applying a sequence of kicks that is designed to open and close the motional phase space trajectory, satisfying the condition

$$\sum_{k=1}^n z_k e^{i\omega t_k} = 0 \quad (7.3)$$

(imagine a set of vectors in the complex plane placed tip to tail; then closing phase space means this chain ends up back where it started), the accumulated phase is independent of the initial motion, and the final state is given by

$$\alpha(t_n) = e^{-i\omega t_n} \alpha_0 \quad (7.4)$$

$$\xi_n = \sum_{k=2}^n \sum_{j=1}^{k-1} z_k z_j \sin[\omega(t_k - t_j)]. \quad (7.5)$$

7.2 Two Ion Relative Phase Accumulation

Now consider again two trapped $^{171}\text{Yb}^+$ ions which are being kicked simultaneously by the same laser (Fig. 7.1) along one principle radial direction of the trap.

In [34, 44], the SDK operator is recast in terms of the CoM and relative mode to

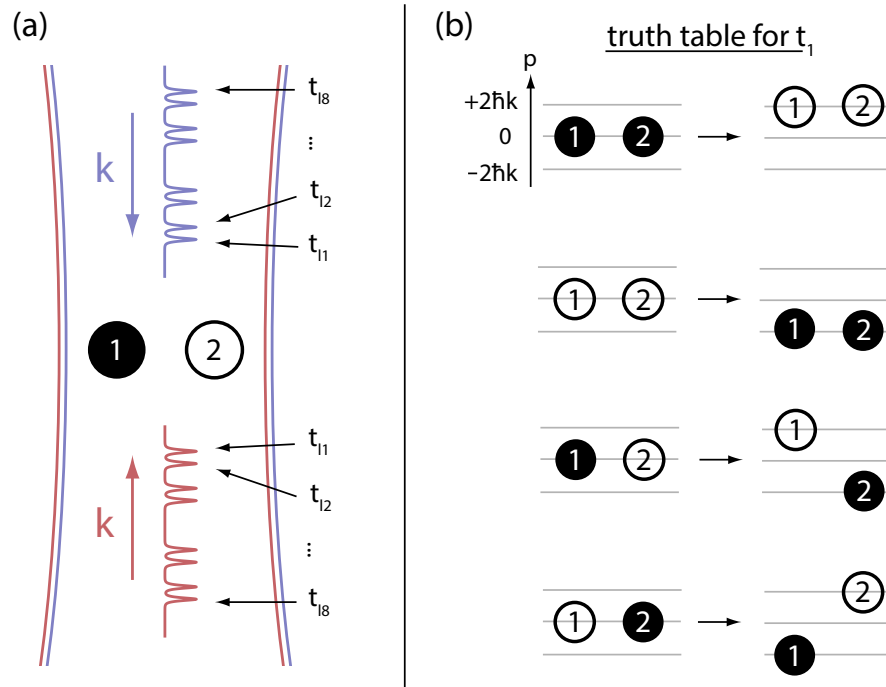


Figure 7.1: A two ion SDK. (a) An SDK on two ions is made using the same eight-pulse sequence discussed in previous chapters. The beam is applied to both ions simultaneously. The color of the ion specifies the spin state (black is $|\downarrow\rangle$ and white is $|\uparrow\rangle$), and the number is the physical position of ions. (b) Truth table for the two ion SDK. Depending on the initial qubit state of the ion, the SDK kicks the ion in the positive or negative direction.

be

$$\begin{aligned}\hat{O}_{SDK}(t) &= e^{2i\phi(t)}\hat{\sigma}_{+,1}\hat{\sigma}_{+,2}\hat{\mathcal{D}}_C[i\eta_C] + \hat{\sigma}_{+,1}\hat{\sigma}_{-,2}\hat{\mathcal{D}}_R[i\eta_R] \\ &\quad + e^{-2i\phi(t)}\hat{\sigma}_{-,1}\hat{\sigma}_{-,2}\hat{\mathcal{D}}_C[-i\eta_C] + \hat{\sigma}_{-,1}\hat{\sigma}_{+,2}\hat{\mathcal{D}}_R[i\eta_R],\end{aligned}\quad (7.6)$$

where $\hat{\mathcal{D}}_C[]$ and $\hat{\mathcal{D}}_R[]$ are the displacement operators for the normal modes, and η_C and η_R are the modified Lambe-Dicke parameters

$$\eta_C = \sqrt{2}\eta \quad (7.7)$$

$$\eta_R = \sqrt{2}\sqrt{\frac{\omega}{\omega_R}}\eta. \quad (7.8)$$

With kick size $z_k = b_k\eta_{C,R}$, where $b_k = \pm 1$ signifies the kick direction, and Eq. 7.3 being satisfied for both mode frequencies (which we guarantee by proper tuning of the trap voltages), the accumulated phase difference between the modes of motion is

$$\Phi = \sum_{k=2}^n \sum_{j=1}^{k-1} b_k b_j (\eta_R^2 \sin[\omega_R(t_j - t_k)] - \eta_C^2 \sin[\omega_C(t_j - t_k)]). \quad (7.9)$$

In terms of a truth table (where the two qubit state is represented in a single ket for simplicity), the gate has the effect

$$|\downarrow\downarrow\rangle \Rightarrow e^{i(\Phi+\gamma)}i|\downarrow\downarrow\rangle \quad (7.10)$$

$$|\downarrow\uparrow\rangle \Rightarrow |\downarrow\uparrow\rangle \quad (7.11)$$

$$|\uparrow\downarrow\rangle \Rightarrow |\uparrow\downarrow\rangle \quad (7.12)$$

$$|\uparrow\uparrow\rangle \Rightarrow e^{i(\Phi-\gamma)}i|\uparrow\uparrow\rangle, \quad (7.13)$$

where the additional phase

$$\begin{aligned} \gamma &= \phi(t_1) - \phi(t_2) + \phi(t_3) - \dots \\ &= \omega_A(t_1 - t_2 + t_3 - \dots) + \begin{cases} 0, & \text{if } n \text{ even} \\ -\phi_0, & \text{if } n \text{ odd} \end{cases} \end{aligned} \quad (7.14)$$

is imparted on the CoM mode and pertains to the phase of the light at the occurrence of each kick [44] (as previously mentioned, the relative frequency ω_A between the two, counter-propagating laser beams is introduced with AOMs). It is crucial to notice that the optical phase ϕ_0 only cancels for an even number of total kicks during a gate sequence. The phase that remains does not affect the amount of entanglement but does affect how the entanglement is witnessed through parity oscillations. This is discussed further in the next section.

7.3 A Particular Solution

We realize a gate by following a technique which has previously been outlined [32, 34]. The gate utilizes a particular symmetry to reduce the number of available paths in phase space, which also allows us to calibrate the gate without adjusting the motional mode frequencies. We build this gate using a sequence outlined as: N_1 kicks, followed by an absence of kicks with duration equal to the time it would take for N_2 kicks, then applying another N_1 kicks which can be in the same, or opposite direction, then waiting in the absence of N_3 kicks before repeating the first three stages, possibly inverting the kick directions. The pulses and waits are separated in time by $1/f_{rep}$ and occur at times t_i . This is outlined in Fig. 7.2. The values of N_1 ,

N_2 , and N_3 are given by solutions to Eq. 7.3, which is satisfied when either

$$1 - e^{iN_1\omega_{C,R}/f_{rep}} = 0, \text{ or} \quad (7.15)$$

$$1 \pm e^{i(N_1+N_2)\omega_{C,R}/f_{rep}} = 0, \text{ or} \quad (7.16)$$

$$1 \pm e^{i(2N_1+N_2+N_3)\omega_{C,R}/f_{rep}} = 0 \quad (7.17)$$

for both ω_C and ω_R (mixing and matching is alright, as long as at least one equation is satisfied for each). It is not immediately clear that Eq. 7.15 is too restrictive, but we will see that because $\omega_{C,R}/f_{rep}$ have an additional constraint, we cannot use Eq. 7.15 to provide a solution. We may, however, use Eq. 7.16 (\rightarrow Eq. 7.18) and 7.17 (\rightarrow Eq. 7.19) to provide solutions of the form

$$(N_1 + N_2) = n \frac{\omega_{rep}}{2\omega_{C,R}}; n \in \mathbb{N} \quad (7.18)$$

$$(2N_1 + N_2 + N_3) = m \frac{\omega_{rep}}{2\omega_{R,C}}; m \in \mathbb{N}. \quad (7.19)$$

The integers n and m are free parameters which are proportional to the number of trap evolutions that occur during the wait times N_2 and N_3 , meaning lower values yield faster gate times (but still tied to the trap period), while larger values often give more relative phase accumulation. The values n and m also set the kick directions (see Fig. 7.2). Also note that if $\omega_{rep}/2\omega_{C,R}$ is an even integer, these equations are satisfied for all values of n and m .

We now have all the tools to pick parameters for an entangling gate. One solution that works for our particular setup is $f_C = f_{rep}/66 = 1.234$ MHz and $f_R = f_{rep}/72 = 1.1308$ MHz. We set N_1 to be 1, 2, 3, 4, 5, and 6, and solve N_2 and N_3 for each. In practice, this allows us to observe phase accumulation while

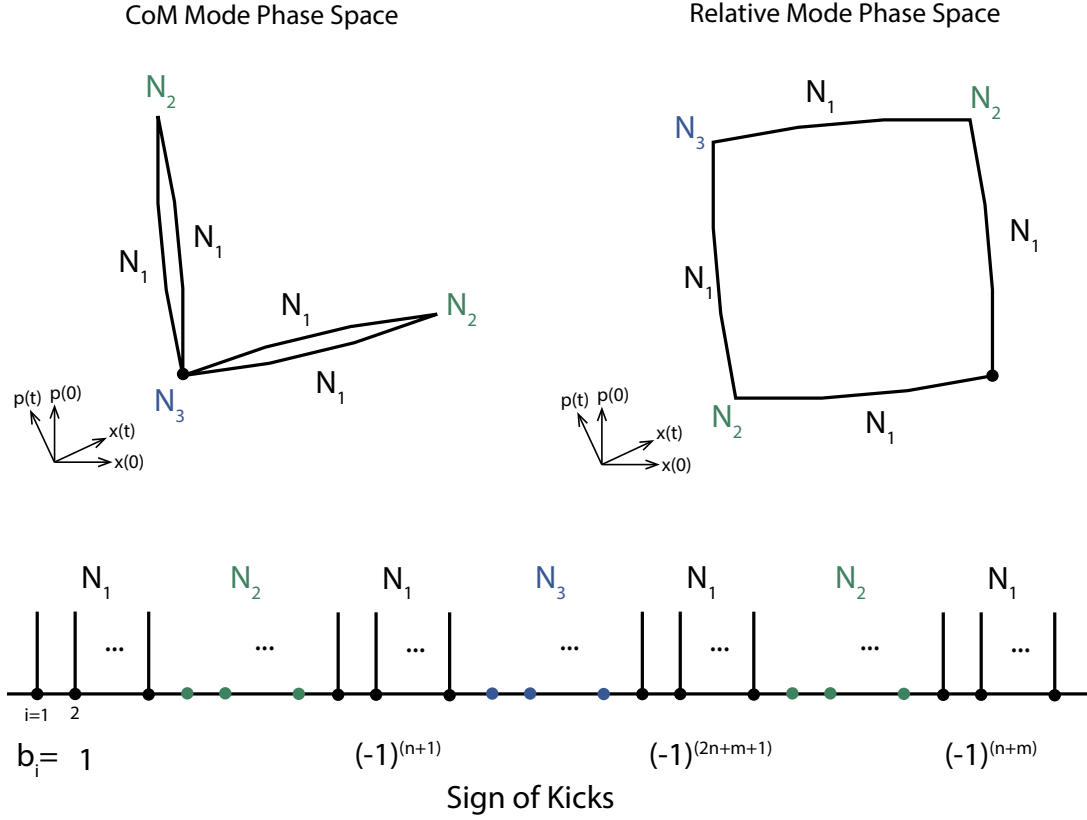


Figure 7.2: Phase space and SDK timing for a gate. This is displayed in frames that rotate at the respective mode frequencies, and the area enclosed is the accumulated phase of each mode. N_1 kicks are separated by N_2 and N_3 periods of waiting. The period between each kick (kicks are shown as vertical lines connected by a node to the horizontal time axis) is given by the repetition rate of the mode locked laser—a fixed number. The direction (sign) of each kick is given by b_i and is the same for each group of N_1 , but can be different between groups depending on the chosen solution. Definitions for n and m are given in Eqs. 7.18 and 7.19.

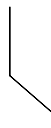
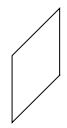
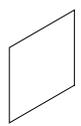
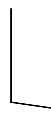
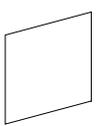
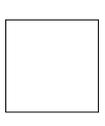
| $N_1 = 1$ CoM mode closes first Rel. mode closes second | $\{n, m\}$ | f_C | f_R | $\{N_2, N_3, \Phi\}$ |
|---------------------------------------------------------------|------------|-------------------------------------------------------------------------------------|--------------------------------------------------------------------------------------|----------------------|
| | $\{1, 1\}$ |  |  | $\{32, 2, 0.045\}$ |
| | $\{2, 2\}$ |  |  | $\{65, 5, 0.087\}$ |
| | $\{3, 3\}$ |  |  | $\{98, 8, 0.123\}$ |
| | $\{4, 4\}$ |  |  | $\{131, 11, 0.151\}$ |
| | $\{5, 5\}$ |  |  | $\{164, 14, 0.169\}$ |
| | $\{6, 6\}$ |  |  | $\{197, 17, 0.175\}$ |

Figure 7.3: Phase space trajectory for $N_1 = 1$ following the scheme of Fig. 7.1. The trajectories for the CoM mode follow paths that perfectly backtrack (zero phase accumulation) because there is only one kick in each direction and so there is no trap evolution between kicks. Images are scaled to fit the table.

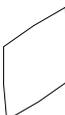
| $N_1 = 2$ CoM mode closes first Rel. mode closes second | $\{n, m\}$ | f_c | f_R | $\{N_2, N_3, \Phi\}$ |
|---------------------------------------------------------------|------------|-------------------------------------------------------------------------------------|--------------------------------------------------------------------------------------|----------------------|
| | $\{1, 1\}$ |  |  | $\{31, 1, 0.18\}$ |
| | $\{2, 2\}$ |  |  | $\{64, 4, 0.348\}$ |
| | $\{3, 3\}$ |  |  | $\{97, 7, 0.493\}$ |
| | $\{4, 4\}$ |  |  | $\{130, 10, 0.603\}$ |
| | $\{5, 5\}$ |  |  | $\{163, 13, 0.673\}$ |
| | $\{6, 6\}$ |  |  | $\{196, 16, 0.697\}$ |

Figure 7.4: Phase space trajectory for $N_1 = 2$ following the scheme of Fig. 7.1. Images are scaled to fit the table.

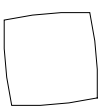
| | $\{n, m\}$ | f_C | f_R | $\{N_2, N_3, \Phi\}$ |
|-----------|------------|-------------------------------------------------------------------------------------|---------------------------------------------------------------------------------------|----------------------|
| $N_1 = 3$ | $\{1, 1\}$ |  |  | $\{30, 0, 0.405\}$ |
| | $\{6, 6\}$ |  |  | $\{195, 15, 1.563\}$ |
| $N_1 = 4$ | $\{6, 6\}$ |  |  | $\{194, 14, 2.767\}$ |
| $N_1 = 5$ | $\{3, 3\}$ |  |  | $\{94, 4, 3.034\}$ |
| $N_1 = 6$ | $\{1, 1\}$ |  |  | $\{60, 0, 3.075\}$ |

Figure 7.5: Phase space trajectory for $N_1 = 3, 4, 5, 6$ following the scheme of Fig. 7.1. Images are scaled to fit the table.

keeping the main source of infidelity—the kick number N_1 —down before scaling up the phase accumulation to generate more entanglement between the ions. Tables of some solutions, along with a phase space trajectory for several values of n and m , are shown in Figs. 7.3-7.5. It is clear that only $m \geq n$ works for our trap frequencies. Furthermore, having $m > n$ only increases time and not phase accumulation, so those cases are not considered. Thus, for these solutions $m = n$, but other solutions exist and would be useful in certain situations. The phase Φ is calculated using Eq. 7.9, with the values of b_i chosen to close phase space, and shown in Fig. 7.2.

7.4 Measuring Entanglement

Knowing the phase accumulation for each kick sequence, it is possible to describe how an entanglement witness, in this case parity, should look. We describe a global microwave qubit rotation as

$$\hat{R}_\mu(\theta_\mu, \phi_\mu) = [\cos \frac{\theta_\mu}{2} \hat{1}_1 + i \sin \frac{\theta_\mu}{2} \hat{\sigma}_1 \cdot \vec{u}(\phi_\mu)] \otimes [\cos \frac{\theta_\mu}{2} \hat{1}_2 + i \sin \frac{\theta_\mu}{2} \hat{\sigma}_2 \cdot \vec{u}(\phi_\mu)], \quad (7.20)$$

where the qubit is rotated about the Bloch sphere vector

$$\vec{u}(\phi_\mu) = \cos \phi_\mu \vec{e}_x + \sin \phi_\mu \vec{e}_y \quad (7.21)$$

using the Pauli matrices

$$\hat{\sigma}_{1,2} = \hat{\sigma}_{1,2x} \vec{e}_x + \hat{\sigma}_{1,2y} \vec{e}_y + \hat{\sigma}_{1,2z} \vec{e}_z, \quad (7.22)$$

and the quantities θ_μ and ϕ_μ are the microwave pulse area and phase. The ultrafast entangling gate operation may be written as

$$\hat{G} = e^{i(\Phi+\gamma)} |00\rangle \langle 00| + |01\rangle \langle 01| + |10\rangle \langle 10| + e^{i(\Phi-\gamma)} |11\rangle \langle 11|, \quad (7.23)$$

where Φ and γ are from Eqs. 7.9 and 7.14. A full entangling experiment is described with a set of operations taking an initial state $|00\rangle$ to the final state $|\psi_f\rangle$:

$$|\psi_f\rangle = \hat{R}_\mu(\theta_{\mu,a}, \phi_{\mu,a}) \hat{R}_\mu(\theta_{\mu,2}, \phi_{\mu,2}) \hat{G} \hat{R}_\mu(\theta_{\mu,1}, \phi_{\mu,1}) |00\rangle. \quad (7.24)$$

Fluorescence collected during detection over many experiments yields the probability of 0, 1, and 2 bright ions (see Fig. 2.6(b)) and is used to find the parity [30]

$$P = |\langle 11|\psi_f\rangle|^2 + |\langle 00|\psi_f\rangle|^2 - (|\langle 10|\psi_f\rangle|^2 + |\langle 01|\psi_f\rangle|^2). \quad (7.25)$$

In practice, because we are using a single-channel PMT there is no discrimination between the quantities $|\langle 10|\psi_f\rangle|^2$ and $|\langle 01|\psi_f\rangle|^2$; both register as one bright ion (again, recall Fig. 2.6(b)). This is not a problem because the quantity is summed in Eq. 7.25, and so we use the total quantity in that bin. A critical feature of Eq. 7.24 is the second microwave rotation $\hat{R}_\mu(\theta_{\mu,2}, \phi_{\mu,2})$, which occurs before the final analysis pulse. This rotation allows us to compensate for the effect that the phase γ has on the parity oscillation curve which is important because γ can be $\gg 1$.

This experiment is currently underway, and only one set of preliminary data has been taken. We have set $N_1 = 1$, while $n = 3$ and $m = 3$, giving a modest phase of $\Phi = \pi/25$ and a gate time of about $4 \mu\text{s}$. Taking a parity curve for 3 different values of N_3 , with the phase $\phi_{\mu,2}$ set at the theoretical optimum to cancel γ (ideally the optimum would be measured experimentally), we see the curves in Fig. 7.6(a). When $N_3 = 8$ (red data in Fig. 7.6(a)), which satisfies the condition to completely close phase space in this case, parity oscillations are consistent in amplitude with the model in Fig. 7.6(b). When $N_3 = 23$, in which the spin and motion do not disentangle, we see the parity signature disappear (black data in Fig.

7.6). Additionally, the effects of the phase γ are only present when N_3 is even. When $N_3 = 13$ (blue data in Fig. 7.6(a)), the parity oscillation is decreased in amplitude but still present indicating it is a result of entanglement. The decrease in parity amplitude from $N_3 = 8$ to $N_3 = 13$ to $N_3 = 23$ is consistent with the motional linewidth (see Chapter 4 on atom interferometry) at the measured thermal phonon occupation of $\bar{n} = 13$. The reason for the offset of the parity curve is likely calibration error of the histogram fitting, as described in Chapter 2.3.2. These measurements need to be improved, and there are a number of things that should increase fidelity such as pointing stability and reducing aberrations in the Raman laser beam, Pockels cell upgrades, higher experimental duty cycle to experimentally find γ , and more experience with histogram calibration for multiple ions. With this, there should be a clear path to increase this to $\Phi = \pi/2$ (a fully entangled state).

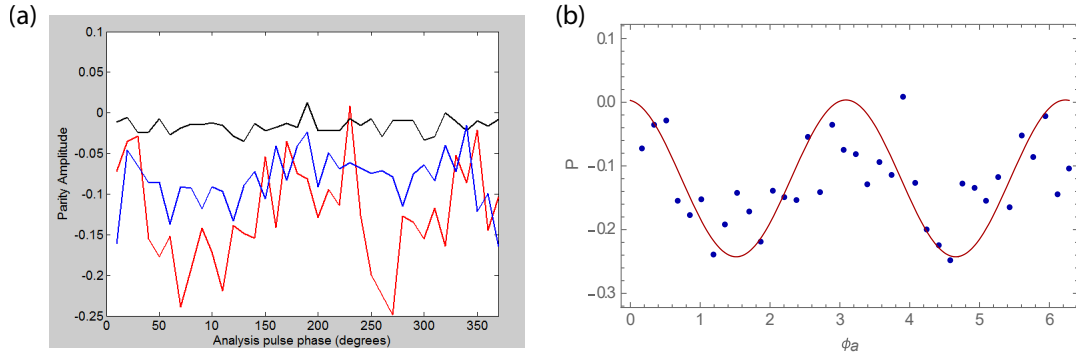


Figure 7.6: Ultrafast Entanglement Parity Oscillations. (a) Parity data for $N_1 = 1$ with $N_3 = 8$ (red, proper solution for entangling gate), $N_3 = 13$ (blue) and $N_3 = 23$ (black). When, $N_3 = 8$, the gate phase $\Phi = \pi/25$. Decreased amplitude in the blue and zero amplitude in the black plots is due to reduced and zero overlap of final motional states, showing that there is a motional dependence in the parity curves and entanglement for $N_3 = 8$ and $N_3 = 13$. The offset is likely due to histogram calibration error. (b) Theoretical parity oscillation overlying the $N_3 = 8$ entangling gate data. The theory curve is shifted down to match the offset of the data, but the amplitude, phase, and frequency are not used as fitting parameters.

Chapter 8: Outlook and Future Directions

The experiments presented here provide a sense of what ultrafast laser-atom interactions can be used for. In addition to improving the ultrafast entangling gate to its theoretical limit, there are still a number of experiments that only this apparatus (as of now) is capable of doing. Here is a short list of ones we find particularly interesting.

8.1 Imaging a Large Cat State and Other Motion

Based on the research that is presented in Chapters 5 and 6, it should be possible to directly image the separation between two parts of a large cat state. With the current trap frequency of $\omega/2\pi = 1$ MHz, 100 SDKs produces separation of

$$\Delta x = 2 \frac{p}{m\omega} \sim 400 \text{ nm}, \quad (8.1)$$

where $p = 200\hbar k$ is the momentum absorbed by each component of the cat state, and $m = 171$ amu. The zero-point spread of the wave function is given by

$$x_0 = \sqrt{\frac{\hbar}{2m\omega}} \sim 1 \text{ nm}, \quad (8.2)$$

which is also the size of the components of a cat state made from displaced vacuum states. This zero point spread, however, is much smaller than the wavelength of the detection light, which governs the diffraction limited spot size, even when the trap frequency is decreased by an order of magnitude. At a trap frequency of $\omega/2\pi = 100$ kHz, only 10 SDKs are required to create the same 400 nm of separation. On the other hand, 100 SDKs would make a cat state with a 4 μm separation between the states. By averaging a large number of experiments where we stroboscopically image the ion at points when the cat state is largest, we should be able to collect enough light to see separation between the components. This same technique may be useful for other states of motion.

8.2 Delta-Kicked Harmonic Oscillator

A proposal in 1997 for studying quantum chaos in an ion trap delta-kicked harmonic oscillator remains to be implemented [41]. This is because there is no system capable of providing a delta kick to a quantum harmonic oscillator. The relationship to a delta kicked rotor is discussed in theory [145]. With our system ideally suited for this, we should be able to study some of the properties of such a system.

8.3 Hamiltonian Engineering

By creating SDK laser-atom interactions, which occurs on a time scale shorter than other relevant time scales in the system, it should be possible to engineer

Hamiltonians that would otherwise not be possible using the process of Trotterization [38–40]. This method provides a way of building a time evolution operator that is approximately equal to the evolution operator of the desired Hamiltonian by using a series of different shorter interactions.

8.4 Superfast Cooling

A proposal in 2010 showed another method to perform sub-Doppler cooling using ultrafast pulses [39]. Since then, we have worked with the authors of the proposal to implement this in our system. It is a work in progress.

8.5 Two-dimensional Cat States

By providing a set of SDKs that is not along either axis of a non-degenerate trap (recall Fig. 2.8), it would be possible to create a cat state in two dimensions. We have not worked this out, but it may be useful for studying decoherence or for metrology [107].

8.6 Working in the Infrared

Because of the difficulties involved in working with high power Ultraviolet laser light, we have considered using a visible or infrared laser, which might be doubled or tripled just as it passes into the trap. This could drastically increase our pulse picking extinction ratio, and ability to pulse shape by possibly using a spatial light modulator (SLM)—both of which would increase the fidelity of the SDK. This is also

a very recent proposal, and the best solutions are still being worked out.

Bibliography

- [1] J. Mizrahi, C. Senko, W. C. Campbell, K. G. Johnson, C. W. S. Conover, and C. Monroe. Ultrafast spin-motion entanglement and interferometry with a single atom. *Phys. Rev. Lett.*, 110:203011, 2013.
- [2] W. C. Campbell, J. Mizrahi, Q. Quraishi, C. Senko, D. Hayes, D. Hucul, D. N. Matsukevich, P. Maunz, and C. Monroe. Ultrafast gates for single atomic qubits. *Phys. Rev. Lett.*, 105:090502, 2010.
- [3] L.-M. Duan. Scaling ion trap quantum computation through fast quantum gates. *Phys. Rev. Lett.*, 93:100502, 2004.
- [4] P. W. Shor. Algorithms for quantum computation: Discrete logarithms and factoring. In *Proc. 35nd Annual Symposium on Foundations of Computer Science*, volume 35, pages 124–134, 1994.
- [5] Y. Makhlin, G. Schön, and A. Shnirman. Quantum-state engineering with josephson-junction devices. *Rev. Mod. Phys.*, 73:357–400, May 2001.
- [6] E. Hagley, X. Maître, G. Nogues, C. Wunderlich, M. Brune, J. M. Raimond, and S. Haroche. Generation of Einstein-Podolsky-Rosen pairs of atoms. *Phys. Rev. Lett.*, 79:1–5, Jul 1997.
- [7] F. Jelezko, T. Gaebel, I. Popa, M. Domhan, A. Gruber, and J. Wrachtrup. Observation of coherent oscillation of a single nuclear spin and realization of a two-qubit conditional quantum gate. *Phys. Rev. Lett.*, 93:130501, Sep 2004.
- [8] J. L. O’Brien, G. J. Pryde, A. G. White, T. C. Ralph, and D. Branning. Demonstration of an all-optical quantum controlled-not gate. *Nature*, 426(6964):264–267, 2003.
- [9] A. D. O’Connell, M. Hofheinz, M. Ansmann, R. C. Bialczak, M. Lenander, E. Lucero, M. Neeley, D. Sank, H. Wang, M. Weides, J. Wenner, J. M. Martinis, and A. N. Cleland. Quantum ground state and single-phonon control of a mechanical resonator. *Nature*, 464:697–703, April 2010.

- [10] J. Chan, T. P. M. Alegre, A. H. Safavi-Naeini, J. T. Hill, A. Krause, S. Gröblacher, M. Aspelmeyer, and O. Painter. Laser cooling of a nanomechanical oscillator into its quantum ground state. *Nature*, 478:89–92, October 2011.
- [11] J. D. Teufel, T. Donner, D. Li, J. W. Harlow, M. S. Allman, K. Cicak, A. J. Sirois, J. D. Whittaker, K. W. Lehnert, and R. W. Simmonds. Sideband cooling of micromechanical motion to the quantum ground state. *Nature*, 475:359–363, July 2011.
- [12] R. C. Ashoori. Electrons in artificial atoms. *Nature*, 379:413–419, 1996.
- [13] L. M. K. Vandersypen, M. Steffen, G. Breyta, C. S. Yannoni, M. H. Sherwood, and I. L. Chuang. Experimental realization of Shor’s quantum factoring algorithm using nuclear magnetic resonance. *Nature*, 414(6866):883–887, 2001.
- [14] D. Jaksch, C. Bruder, J. I. Cirac, C. W. Gardiner, and P. Zoller. Cold bosonic atoms in optical lattices. *Physical Review Letters*, 81(15):3108, 1998.
- [15] D. Leibfried, R. Blatt, C. Monroe, and D. Wineland. Quantum dynamics of single trapped ions. *Rev. Mod. Phys.*, 75:281–324, Mar 2003.
- [16] A. J. Leggett. Bose-Einstein condensation in the alkali gases: Some fundamental concepts. *Reviews of Modern Physics*, 73(2):307, 2001.
- [17] K.-K. Ni, S. Ospelkaus, M. H. G. De Miranda, A. Pe’er, B. Neyenhuis, J. J. Zirbel, S. Kotochigova, P. S. Julienne, D. S. Jin, and J. Ye. A high phase-space-density gas of polar molecules. *Science*, 322(5899):231–235, 2008.
- [18] D. J. Wineland. Nobel lecture. superposition, entanglement, and raising Schrödinger’s cat. *Rev. Mod. Phys.*, 85:1103–1114, 2013.
- [19] W. Neuhauser, M. Hohenstatt, P. Toschek, and H. Dehmelt. Optical-sideband cooling of visible atom cloud confined in parabolic well. *Phys. Rev. Lett.*, 41:233–236, Jul 1978.
- [20] D. J. Wineland, R. E. Drullinger, and F. L. Walls. Radiation-pressure cooling of bound resonant absorbers. *Phys. Rev. Lett.*, 40:1639–1642, Jun 1978.
- [21] T. W. Hänsch and A. L. Schawlow. Cooling of gases by laser radiation. *Opt. Commun.*, 13:68, 1975.
- [22] D. J. Wineland and H. Dehmelt. Proposed $10^{14}\Delta\nu < \nu$ laser fluorescence spectroscopy on Tl^+ mono-ion oscillator. *Bull. Am. Phys. Soc.*, 20:637, 1975.
- [23] F. Diedrich, J. C. Bergquist, Wayne M. Itano, and D. J. Wineland. Laser cooling to the zero-point energy of motion. *Phys. Rev. Lett.*, 62:403–406, Jan 1989.

- [24] C. Monroe, D. Meekhof, B. King, S. Jefferts, W. Itano, D. Wineland, and P. Gould. Resolved-sideband raman cooling of a bound atom to the 3d zero-point energy. *Phys. Rev. Lett.*, 75:4011, 1995.
- [25] E. T. Jaynes and F. W. Cummings. Comparison of quantum and semiclassical radiation theories with application to the beam maser. In *Proc. IEEE*, volume 51, pages 89–109, 1963.
- [26] J. I. Cirac and P. Zoller. Quantum computations with cold trapped ions. *Phys. Rev. Lett.*, 74:4091–4094, May 1995.
- [27] C. Monroe, D. M. Meekhof, B. E. King, W. M. Itano, and D. J. Wineland. Demonstration of a fundamental quantum logic gate. *Phys. Rev. Lett.*, 75:4714–4717, Dec 1995.
- [28] C. Monroe, D. M. Meekhof, B. E. King, and D. J. Wineland. A “Schrödinger cat” superposition state of an atom. *Science*, 272:1131, 1996.
- [29] D. Leibfried, B. DeMarco, V. Meyer, D. Lucas, M. Barrett, J. Britton, W. M. Itano, B. Jelenkovic, C. Langer, T. Rosenband, and D. J. Wineland. Experimental demonstration of a robust, high-fidelity geometric two ion-qubit phase gate. *Nature*, 422:412–415, March 2003.
- [30] C. A. Sackett, D. Kielpinski, B. E. King, C. Langer, V. Meyer, C. J. Myatt, M. Rowe, Q. A. Turchette, W. M. Itano, D. J. Wineland, and Monroe C. Experimental entanglement of four particles. *Nature*, 404:256–259, March 2000.
- [31] A. Sørensen and K. Mølmer. Quantum computation with ions in thermal motion. *Phys. Rev. Lett.*, 82:1971–1974, 1999.
- [32] J. Mizrahi, B. Neyenhuis, K. G. Johnson, W. C. Campbell, C. Senko, D. Hayes, and C. Monroe. Quantum control of qubits and atomic motion using ultrafast laser pulses. *Appl. Phys. B*, 114:45, 2013.
- [33] K. G. Johnson, B. Neyenhuis, J. Mizrahi, J. D. Wong-Campos, and C. Monroe. Sensing atomic motion from the zero point to room temperature with ultrafast atom interferometry. *Phys. Rev. Lett.*, 115:213001, 2015.
- [34] J. J. Garcia-Ripoll, P. Zoller, and J. I. Cirac. Speed optimized two-qubit gates with laser coherent control techniques for ion trap quantum computing. *Phys. Rev. Lett.*, 91:157901, 2003.
- [35] D. Kielpinski, C. Monroe, and D. J. Wineland. Architecture for a large-scale ion-trap quantum computer. *Nature*, 417(6890):709–711, 2002.
- [36] C. Monroe and J. Kim. Scaling the ion trap quantum processor. *Science*, 339:1164, 2013.

- [37] G. C. Knee and W. J. Munro. Optimal Trotterization in universal quantum simulators under faulty control. *Physical Review A*, 91(5):052327, 2015.
- [38] R. L. Taylor, C. D. B. Bentley, J. S. Pedernales, L. Lamata, E. Solano, A. R. R. Carvalho, and J. J. Hope. Fast gates allow large-scale quantum simulation with trapped ions. *arXiv preprint arXiv:1601.00359*, 2016.
- [39] S. Machnes, M. B. Plenio, B. Reznik, A. M. Steane, and A. Retzker. Superfast laser cooling. *Phys. Rev. Lett.*, 104:183001, 2010.
- [40] L. Ortiz-Gutiérrez, B. Gabrielly, L. F. Muñoz, K. T. Pereira, J. G. Filgueiras, and A. S. Villar. Continuous variables quantum computation over the vibrational modes of a single trapped ion. *arXiv preprint arXiv:1603.00065*, 2016.
- [41] S. A. Gardiner, J. I. Cirac, and P. Zoller. Quantum chaos in an ion trap: the delta-kicked harmonic oscillator. *Physical review letters*, 79(24):4790, 1997.
- [42] K. G. Johnson, J. D. Wong-Campos, A. Restelli, K. A. Landsman, B. Neyenhuis, J. Mizrahi, and C. Monroe. Active stabilization of ion trap radiofrequency potentials. *Review of Scientific Instruments*, 87(5):053110, 2016.
- [43] J. D. Wong-Campos, K. G. Johnson, B. Neyenhuis, J. Mizrahi, and C. Monroe. High-resolution adaptive imaging of a single atom. *Nature Photonics*, 2016.
- [44] J. Mizrahi. *Ultrafast Control of Spin and Motion in Trapped Ions*. PhD thesis, University of Maryland, 2013.
- [45] S. Haroche. Controlling photons in a box and exploring the quantum to classical boundary. *Rev. Mod. Phys.*, 85:1083–1102, 2013.
- [46] M. G. Raizen, J. M. Gilligan, J. C. Bergquist, W. M. Itano, and D. J. Wineland. Ionic crystals in a linear paul trap. *Phys. Rev. A*, 45:6493, 1992.
- [47] H. Dehmelt. Experiments with an isolated subatomic particle at rest. *Rev. Mod. Phys.*, 62:525–530, 1990.
- [48] R. Blatt and D. Wineland. Entangled states of trapped atomic ions. *Nature*, 453:1008–1015, 2008.
- [49] S.-L. Zhu, C. Monroe, and L.-M. Duan. Trapped ion quantum computation with transverse phonon modes. *Phys. Rev. Lett.*, 97:050505, 2006.
- [50] J. Chiaverini, R. B. Blakestad, J. Britton, J. D. Jost, C. Langer, D. Leibfried, R. Ozeri, and D. J. Wineland. Surface-electrode architecture for ion-trap quantum information processing. *Quantum Inf. Comput.*, 5:419, 2005.
- [51] W. Paul. Electromagnetic traps for charged and neutral particles. *Rev. Mod. Phys.*, 62:531–540, 1990.

- [52] M. Cetina. *Hybrid approaches to quantum information using ions, atoms and photons*. PhD thesis, Massachusetts Institute of Technology, 2011.
- [53] J. H. Moore, C. C. Davis, and M. A. Coplan. *Building Scientific Apparatus*. Cambridge University Press, 4 edition, 2009.
- [54] J. R. Young. Outgassing characteristics of stainless steel and aluminum with different surface treatments. *J. Vac. Sci. Technol.*, 6:398, 1969.
- [55] D. J. Wineland, C. Monroe, W. M. Itano, D. Leibfried, B. E. King, and D. M. Meekhof. Experimental issues in coherent quantum-state manipulation of trapped atomic ions. *J. Res. Nat. Inst. Stand. Tech.*, 103:259–328, 1998.
- [56] S. Olmschenk, K. C. Younge, D. L. Moehring, D. N. Matsukevich, P. Maunz, and C. Monroe. Manipulation and detection of a trapped $+Yb$ hyperfine qubit. *Phys. Rev. A*, 76:052314, 2007.
- [57] H. Lehmitz, J. Hattendorf-Ledwoch, R. Blatt, and H. Harde. Population trapping in excited Yb ions. *Physical review letters*, 62(18):2108, 1989.
- [58] A. Bauch, D. Schnier, and C. Tamm. Collisional population trapping and optical deexcitation of ytterbium ions in a radiofrequency trap. *Journal of Modern Optics*, 39(2):389–401, 1992.
- [59] B. C. Fawcett and M. Wilson. Computed oscillator strengths, landé g values, and lifetimes in Yb ii. *Atomic Data and Nuclear Data Tables*, 47(2):241–317, 1991.
- [60] C. Balzer, A. Braun, T. Hannemann, C. Paape, M. Ettler, W. Neuhauser, and C. Wunderlich. Electrostatically trapped Yb $+$ ions for quantum information processing. *Physical Review A*, 73(4):041407, 2006.
- [61] H. J. Metcalf and P. van der Straten. *Laser Cooling and Trapping*. Springer-Verlag New York, 1 edition, 1999.
- [62] R. Noek, G. Vrijsen, D. Gaultney, E. Mount, T. Kim, P. Maunz, , and J. Kim. High speed, high fidelity detection of an atomic hyperfine qubit. *Opt. Lett.*, 38(22):4735–4738, 2013.
- [63] W. M. Itano and D. J. Wineland. Laser cooling of ions stored in harmonic and Penning traps. *Physical Review A*, 25(1):35, 1982.
- [64] M. S. Safronova, V. A. Dzuba, V. V. Flambaum, U. I. Safronova, S. G. Porsev, and M. G. Kozlov. Highly charged ions for atomic clocks, quantum information, and search for α variation. *Physical review letters*, 113(3):030801, 2014.
- [65] D. Hayes, D. N. Matsukevich, P. Maunz, D. Hucul, Q. Quraishi, S. Olmschenk, W. Campbell, J. Mizrahi, C. Senko, and C. Monroe. Entanglement of atomic qubits using an optical frequency comb. *Phys. Rev. Lett.*, 104:140501, 2010.

- [66] A. E. Siegman. *Lasers*. University Science Books, 1986.
- [67] R. Kitamura, L. Pilon, and M. Jonasz. Optical constants of silica glass from extreme ultraviolet to far infrared at near room temperature. *Applied optics*, 46(33):8118–8133, 2007.
- [68] P. J. Wrzesinski, D. Pestov, V. V. Lozovoy, J. R. Gord, M. Dantus, and S. Roy. Group-velocity-dispersion measurements of atmospheric and combustion-related gases using an ultrabroadband-laser source. *Optics express*, 19(6):5163–5170, 2011.
- [69] J. D. Siverns, L. R. Simkins, S. Weidt, and W. K. Hensinger. On the application of radio frequency voltages to ion traps via helical resonators. *Appl. Phys. B*, 107:921, 2012.
- [70] P. Richerme, Z.-X. Gong, A. Lee, C. Senko, J. Smith, M. Foss-Feig, S. Michalakis, A. V. Gorshkov, and C. Monroe. Non-local propagation of correlations in quantum systems with long-range interactions. *Nature*, 511:198, 2014.
- [71] P. Jurcevic, B. P. Lanyon, P. Hauke, C. Hempel, P. Zoller, R. Blatt, and C. F. Roos. Quasiparticle engineering and entanglement propagation in a quantum many-body system. *Nature*, 511:202, 2014.
- [72] C. W. Chou, D. B. Hume, J. C. J. Koelemeij, D. J. Wineland, and T. Rosenband. Frequency comparison of two high-accuracy Al^+ optical clocks. *Phys. Rev. Lett.*, 104:070802, 2010.
- [73] H. Eriksson and R. W. Waugh. *A Temperature Compensated Linear Diode Detector, Design Tip*. Agilent Technologies, 2000.
- [74] N. F. Ramsey. Experiments with separated oscillatory fields and hydrogen masers. *Rev. Mod. Phys.*, 62:541, 1990.
- [75] Q. A. Turchette, C. J. Myatt, B. E. King, C. A. Sackett, D. Kielpinski, W. M. Itano, C. Monroe, and D. J. Wineland. Decoherence and decay of motional quantum states of a trapped atom coupled to engineered reservoirs. *Phys. Rev. A*, 62:053807, 2000.
- [76] D. W. Allan. Statistics of atomic frequency standards. In *Proc. IEEE*, volume 54, page 221, 1966.
- [77] J. Rossnagel, K. N. Tolazzi, F. Schmidt-Kaler, and K. Singer. Fast thermometry for trapped ions using dark resonances. *New J. Phys.*, 17:045004, 2015.
- [78] Q. Turchette, D. Kielpinski, B. King, C. Myatt, C. Sackett, W. Itano, C. Monroe, and D. J. Wineland. Heating of trapped ions from the quantum ground state. *Phys. Rev. A*, 61:063418, 2000.

- [79] C. Roos. *Controlling the Quantum State of Trapped Ions*. PhD thesis, University of Innsbruck, 2000.
- [80] G. Shu, G. Vittorini, A. Buikema, C. S. Nichols, C. Volin, D. Stick, and K. R. Brown. Heating rates and ion-motion control in a y-junction surface-electrode trap. *Phys. Rev. A*, 89:062308, 2014.
- [81] B. C. Sawyer, J. W. Britton, and J. J. Bollinger. Spin dephasing as a probe of mod temperature, motional state distributions, and heating rates in a two-dimensional ion crystal. *Phys. Rev. A*, 89:033408, 2014.
- [82] R. J. Glauber. Coherent and incoherent states of the radiation field. *Phys. Rev.*, 131:2766, 1963.
- [83] E. C. G. Sudarshan. Equivalence of semiclassical and quantum mechanical descriptions of statistical light beams. *Phys. Rev. Lett.*, 10:277, 1963.
- [84] C. J. Myatt, B. E. King, Q. A. Turchette, C. A. Sackett, D. Kielpinski, W. M. Itano, C. Monroe, and D. J. Wineland. Decoherence of quantum superpositions through coupling to engineered reservoirs. *Nature*, 403:269, 2000.
- [85] U. Poschinger, A. Walther, K. Singer, and F. Schmidt-Kaler. Observing the phase space trajectory of an entangled matter wave packet. *Phys. Rev. Lett.*, 105:263602, 2010.
- [86] L. Deslauriers, S. Olmschenk, D. Stick, W. K. Hensinger, J. Sterk, and C. Monroe. Scaling and suppression of anomalous heating in ion traps. *Physical Review Letters*, 97(10):103007, 2006.
- [87] D. J. Wineland and W. M. Itano. Laser cooling of atoms. *Phys. Rev. A*, 20(4):1521, 1979.
- [88] S. Olmschenk. *Quantum Teleportation Between Distant Matter Qubits*. PhD thesis, University of Maryland, College Park, 2009.
- [89] C. Gehrke. *Quantitative Characterization of Nonclassicality*. PhD thesis, University of Rostock, 2008.
- [90] E. Wigner. On the quantum correction for thermodynamic equilibrium. *Phys. Rev.*, 40:749, 1932.
- [91] J. A. Wheeler and W. Zurek. *Quantum Theory and Measurement*. Princeton University Press, 1983.
- [92] V. Giovannetti, S. Lloyd, and L. Maccone. Quantum-enhanced measurements: Beating the standard quantum limit. *Science*, 306:1330–1336, 2004.
- [93] M. A. Nielsen and I. L. Chuang. *Quantum Computation and Quantum Information*. Cambridge University Press, 2000.

- [94] A. Einstein, B. Podolsky, and N. Rosen. Can quantum-mechanical description of physical reality be considered complete? *Phys. Rev.*, 47:777–780, May 1935.
- [95] E. Schrödinger. Die gegenwärtige situation in der quantenmechanik. *Naturwissenschaften*, 23:807–812; 823–828; 844–849, 1935.
- [96] M. Kasevich and S. Chu. Atomic interferometry using stimulated raman transitions. *Physical review letters*, 67(2):181, 1991.
- [97] T. Kovachy, P. Asenbaum, C. Overstreet, C. A. Donnelly, S. M. Dickerson, A. Sugarbaker, J. M. Hogan, and M. A. Kasevich. Quantum superposition at the half-metre scale. *Nature*, 528(7583):530–533, 2015.
- [98] M. Brune, E. Hagley, J. Dreyer, X. Matre, A. Maali, C. Wunderlich, J. M. Raimond, and S. Haroche. Observing the progressive decoherence of the meter in a quantum measurement. *Phys. Rev. Lett.*, 77:4887, 1996.
- [99] J. E. Mooij, T. P. Orlando, L. Levitov, L. Tian, C. H. Van der Wal, and S. Lloyd. Josephson persistent-current qubit. *Science*, 285(5430):1036–1039, 1999.
- [100] J. R. Friedman, V. Patel, W. Chen, S. K. Tolpygo, and J. E. Lukens. Quantum superposition of distinct macroscopic states. *Nature*, 406(6791):43–46, 2000.
- [101] B. Vlastakis, G. Kirchmair, Z. Leghtas, S. E. Nigg, L. Frunzio, S. M. Girvin, M. Mirrahimi, M. H. Devoret, and R. J. Schoelkopf. Deterministically encoding quantum information using 100-photon Schrödinger cat states. *Science*, 342:607, 2013.
- [102] N. Dörre, J. Rodewald, P. Geyer, B. von Issendorff, P. Haslinger, and M. Arndt. Photofragmentation beam splitters for matter-wave interferometry. *Physical review letters*, 113(23):233001, 2014.
- [103] P. Geyer, U. Sezer, J. Rodewald, L. Mairhofer, N. Dörre, P. Haslinger, S. Eibenberger, C. Brand, and M. Arndt. Perspectives for quantum interference with biomolecules and biomolecular clusters. *Physica Scripta*, 91(6):063007, 2016.
- [104] D. Kienzler, C. Fluhmann, V. Negnevitsky, H.-Y. Lo, M. Marinelli, D. Nadlinger, and J. P. Home. Observation of quantum interference between separated mechanical oscillator wave packets. *Phys. Rev. Lett.*, 116:140402, 2016.
- [105] M. Hofheinz, H. Wang, M. Ansmann, R. C. Bialczak, E. Lucero, M. Neeley, A. D. OConnell, D. Sank, J. Wenner, J. M. Martinis, and A. N. Cleland. Synthesizing arbitrary quantum states in a superconducting resonator. *Nature*, 459:546, 2009.

- [106] D. Leibfried, D. M. Meekhof, B. E. King, C. Monroe, W. M. Itano, and D. J. Wineland. Experimental determination of the motional quantum state of a trapped atom. *Phys. Rev. Lett.*, 77:4281, 1996.
- [107] W. C. Campbell and P. Hamilton. Rotation sensing with trapped ions. *arXiv preprint arXiv:1609.00659*, 2016.
- [108] W. Moerner. Nobel lecture: Single-molecule spectroscopy, imaging, and photocontrol: Foundations for super-resolution microscopy. *Rev. Mod. Phys.*, 87:1183–1212, 2015.
- [109] E. Betzig. Nobel lecture: Single molecules, cells, and super-resolution optics. *Rev. Mod. Phys.*, 87:1153–1168, 2015.
- [110] E. Rittweger, K. Y. Han, S. E. Irvine, C. Eggeling, and S. W. Hell. Sted microscopy reveals crystal colour centres. *Nature Photon.*, 3:144–147, 2009.
- [111] E. Betzig, G. H. Patterson, R. Sougrat, O. W. Lindwasser, S. Olenych, J. S. Bonifacino, M. W. Davidson, J. Lippincott-Schwartz, and H. F. Hess. Imaging intracellular fluorescent proteins at nanometer resolution. *Science*, 313:1642–1645, 2006.
- [112] W. Bakr, J. Gillen, A. Peng, Fölling S., and M. Greiner. A quantum gas microscope for detecting single atoms in a hubbard–regime optical lattice. *Nature*, 462:74–77, 2009.
- [113] S. Hell. Nobel lecture: Nanoscopy with freely propagating light. *Rev. Mod. Phys.*, 87:1169–1182, 2015.
- [114] C. Monroe, R. Raussendorf, A. Ruthven, K. R. Brown, P. Maunz, L.-M. Duan, and J. Kim. Large-scale modular quantum-computer architecture with atomic memory and photonic interconnects. *Phys. Rev. A*, 89:022317, 2014.
- [115] J. Eschner, C. Raab, F. Schmidt-Kaler, and R. Blatt. Light interference from single atoms and their mirror images. *Nature*, 413:495–498, 2001.
- [116] M. Biercuk, H. Uys, J. Britton, A. VanDevender, and J. Bollinger. Ultrasensitive detection of force and displacement using trapped ions. *Nature Nanotech.*, 5:646–650, 2010.
- [117] N. Schlosser, G. Reymond, I. Protsenko, and P. Grangier. Sub-poissonian loading of single atoms in a microscopic dipole trap. *Nature*, 411:1024–1027, 2001.
- [118] L. Karpa, A. Bylinskii, D. Gangloff, M. Cetina, and Vuletić. Suppression of ion transport due to long-lived subwavelength localization by an optical lattice. *Phys. Rev. Lett.*, 111:163002, 2013.

- [119] C.T. Schmiegelow, H. Kaufmann, T. Ruster, J. Schulz, V. Kaushal, M. Hettrich, F. Schmidt-Kaler, and U.G. Poschinger. Phase-stable free-space optical lattices for trapped ions. *Phys. Rev. Lett.*, 116:033002, 2016.
- [120] A. Alberti, C. Robens, W. Alt, S. Brakhane, M. Karski, R. Reimann, A. Widera, and D. Meschede. Super-resolution microscopy of single atoms in optical lattices. *New J. Phys.*, 18:053010, 2015.
- [121] A. Burrell, D. Szwer, S. Webster, and D. Lucas. Scalable simultaneous multiqubit readout with 99.99% single-shot fidelity. *Phys. Rev. A*, 81:040302, 2010.
- [122] E. Streed, Norton B., A. Jechow, Weinhold T., and D. Kielpinski. Imaging of trapped ions with a microfabricated optic for quantum information processing. *Phys. Rev. Lett.*, 106:010502, 2011.
- [123] G. Shu, C. Chou, N. Kurz, M. Dietrich, and B. Blinov. Efficient fluorescence collection and ion imaging with the tack ion trap. *J. Opt. Soc. Am. B*, 28:2865–2870, 2011.
- [124] J. Goodman. *Introduction to Fourier Optics*. McGraw-Hill, 1996.
- [125] V. N. Mahajan. *Optical Imaging and Aberrations: Part I: Ray Geometrical Optics*. Bellingham: SPIE-The International Society for Optical Engineering, 1998.
- [126] J. Wyant and K. Creath. *Applied Optics and Optical Engineering*, volume XI. Academic Press, 1992.
- [127] I. Iglesias. Parametric wave-aberration retrieval from point-spread function data by use of a pyramidal recursive algorithm. *Appl. Opt.*, 37:5427–5430, 1998.
- [128] R. Barakat and B. Sandler. Determination of the wave-front aberration function from measured values of the point-spread function: a two-dimensional phase retrieval problem. *J. Opt. Soc. Am. A*, 9:1715–1723, 1992.
- [129] C. Avoort, J. Braat, P. Dirksen, and A. Janssen. Aberration retrieval from the intensity point-spread function in the focal region using the extended nijboer-zernike approach. *J. Mod. Opt.*, 52:1695–1728, 2005.
- [130] I. Novotny and B. Hecht. *Principles of Nano-Optics*. Cambridge University Press, 2006.
- [131] M. Speidel, A. Jonáš, and E. Florin. Three-dimensional tracking of fluorescent nanoparticles with subnanometer precision by use of off-focus imaging. *Opt. Lett.*, 28:69–71, 2003.

- [132] K. Nelson, X. Li, and D. Weiss. Imaging single atoms in a three-dimensional array. *Nature Phys.*, 3:556–560, 2007.
- [133] W. Riley. *Handbook of frequency stability analysis*. Special Publication 1065. NIST, 2008.
- [134] J. Barnes and D. Allan. Variances based on data with dead time between the measurements. Technical report, NIST, 1990. 1318.
- [135] R. Thompson, D. Larson, and W. Webb. Precise nanometer localization analysis for individual fluorescent probes. *Biophys. J.*, 82:2775–2783, 2002.
- [136] T. Quan, S. Zeng, and Z. Huang. Localization capability and limitation of electron-multiplying charge-coupled, scientific complementary metal-oxide semiconductor, and charge-coupled devices for superresolution imaging. *J. Biomed. Opt.*, 15:066005, 2010.
- [137] D. Berkeland, J. Miller, J. Bergquist, W. Itano, and D. Wineland. Minimization of ion micromotion in a paul trap. *J. Appl. Phys.*, 83:5025–5033, 1998.
- [138] J. Keller, H. Partner, T. Burgermeister, and T. Mehlstäubler. Precise determination of micromotion for trapped-ion optical clocks. *J. Appl. Phys.*, 118:104501, 2015.
- [139] U. Eichmann, J. C. Bergquist, J. J. Bollinger, J. M. Gilligan, W. M. Itano, D. J. Wineland, and M. G. Raizen. Youngs interference experiment with light scattered from two atoms. *Physical review letters*, 70(16):2359, 1993.
- [140] D. Anderson. Alignment of resonant optical cavities. *Appl. Opt.*, 23:2944–2949, 1984.
- [141] P. T. H. Fisk, M. J. Sellars, M. A. Lawn, and G. Coles. Accurate measurement of the 12.6 GHz “clock” transition in trapped $^{171}\text{Yb}^+$ ions. *IEEE transactions on ultrasonics, ferroelectrics, and frequency control*, 44(2):344–354, 1997.
- [142] D. L. Moehring, P. Maunz, S. Olmschenk, K. C. Younge, D. N. Matsukevich, L.-M. Duan, and C. Monroe. Entanglement of single-atom quantum bits at a distance. *Nature*, 449(7158):68–71, 2007.
- [143] D. Hucul, I. V. Inlek, G. Vittorini, C. Crocker, S. Debnath, S. M. Clark, and C. Monroe. Modular entanglement of atomic qubits using photons and phonons. *Nature Physics*, 11(1):37–42, 2015.
- [144] C. Monroe, R. Raussendorf, A. Ruthven, K. R. Brown, P. Maunz, L.-M. Duan, and J. Kim. Large-scale modular quantum-computer architecture with atomic memory and photonic interconnects. *Physical Review A*, 89(2):022317, 2014.
- [145] D. R. Grempel, R. E. Prange, and S. Fishman. Quantum dynamics of a nonintegrable system. *Physical Review A*, 29(4):1639, 1984.